AN ABSTRACT OF THE DISSERTATION OF

Jay R. Alder for the degree of Doctor of Philosophy in Geography presented on March 7, 2011.

Title: Simulating Past, Present, and Future Changes in ENSO: a Model Evaluation and Data-model Comparison

Abstract approved:

Steve W. Hostetler Julia A. Jones

This thesis presents the results of a formal evaluation of a new AOGCM, GENMOM, demonstrating its ability to simulate present-day climate and ENSO dynamics. The model is applied to simulate climate for the Last Glacial Maximum, deglacial, and Holocene time periods. The model output is evaluated against the best available proxy reconstructions in a detailed data-model comparison. ENSO strength is analyzed in seven paleo simulations and compared to coral and laminated lake sediment proxy records to provide an understanding of how ENSO related mechanisms varied in the past and how they vary under increased atmospheric CO_2 forced global warming.

The GENMOM simulated present-day is found to be on par with three models used in the IPCC AR4 assessment and is comparable with reanalysis products (e.g, NCEP2). Atmospheric features such as the jet stream structure and major semi-permanent sea level pressure centers are well simulated as is the mean planetary-scale wind structure that is needed to produce the correct position of stormtracks. Most ocean surface currents are reproduced except where they are not resolvable at T31 resolution. Overall, GENMOM captures the observed gradients and spatial distributions of annual surface temperature and precipitation and the simulations are on par with other

AOGCMs. Deficiencies in the GENMOM present-day simulation include a warm bias in the surface temperature over the southern oceans, a split in the ITCZ and weaker-than-observed overturning circulation. GENMOM produces a global temperature bias of 0.6 °C. GENMOM is demonstrated to capture ENSO dynamics similar to eight AOGCMs that were evaluated in the IPCC AR4. The Niño 3 - 4 indices have a standard deviation within 0.3 °C of the observations, indicating GENMOM is producing variability in the tropical Pacifc that is comparable to observations. GENMOM produces present-day ENSO events with an average period of 5.6 years, which is within the 2 – 7 range exhibited in the observed historical record. The mid-Holocene (6ka) and Last Glacial Maximum (LGM, 21ka) simulations are compared to the best available proxy reconstructions for sea surface temperature, precipitation and net moisture to ensure the simulations are plausible. This thesis finds that the model is in good agreement over broad spatial scales, with regional discrepancies between the model and proxy data.

Coral and laminated lake sediment proxy records indicate mid-Holocene ENSO strength was reduced by 15 - 60%, offering a scenario in which ENSO-related components can be tested in climates different than present-day, thereby providing context for future changes in ENSO. The mid-Holocene simulations exhibit a 20% reduction of ENSO strength, caused by a precession forced enhancement of the Indian summer monsoon, which strengthened ENSO-related Bjerknes feedbacks. ENSO strength in the LGM is weakened by ~25%, which is not found to be caused by changes in equatorial Pacific dynamics but rather mean state cooling that weakens the tropical thermocline. The 2x and 4x simulations have strongly enhanced and more frequent ENSO events caused by disproportionate warming of the eastern Pacific relative to the western Pacific, which weakens the east-west Pacific surface temperature gradient, allowing larger anomalies, and hence ENSO events, to develop.

SIMULATING PAST, PRESENT, AND FUTURE CHANGES IN ENSO:
A MODEL EVALUATION AND DATA-MODEL COMPARISON

by

Jay R. Alder

A DISSERTATION

submitted to

Oregon State University

in partial fulfillment of
the requirements for the
degree of

Doctor of Philosophy

Presented March 7, 2011
Commencement June 2011

Doctor of Philosophy dissertation of Jay R. Alder presented March 7, 2011.

APPROVED:

Co-Major Professor, representing Geography

Co-Major Professor, representing Geography

Chair of the Department of Geosciences

Dean of the Graduate School

I understand that my dissertation will become part of the permanent collection of Oregon State University libraries. My signature below authorizes release of my dissertation to any reader upon request.

Jay R. Alder, Author

ACKNOWLEDGEMENTS

I owe a great deal of thanks to my advisor, Steve Hostetler, who has essentially made my entire graduate career possible. Being an online black hole and only a name on the department faculty board, I am profoundly fortunate to have found Steve at all (thanks to Julia Jones). Steve and I immediately resonated together as we are both interested in climate but are essentially computer/tech geeks. As an advisor he helped me define my research interests while allowing a lot of leeway in which direction I took them. He has done a wonderful job in providing the computer resources I needed to perform my work, knowing full well no matter how many computers we have they will never be idle. I appreciate him recognizing early on that me constantly being in his office was not an inability to work independently, but rather that we could share in the excitement of some cool new finding or figure, or conversely, struggle through a coding problem together. He has spent many hours reviewing and helping to revise my papers, which has enabled me to become a better author. Steve has become both my mentor and my friend, and I am glad we have our inside jokes about how many thousands of years of computer simulations we've performed and how many thousands we've had to throw out; or recognizing that we may be trying to solve the climate problems of tomorrow, all while our super computers draw as much energy as a small city.

I thank my committee members for encouraging and supporting me when I've set an aggressive schedule to complete both my MS and Ph.D. To Dave Pollard for promptly and thoroughly answering all my naïve questions in addition to developing the model that I based all my work on. To Julia Jones for constantly reinforcing that climate modeling is geography. To Andreas Schmittner for being patient with me and helping me to understand the role of the ocean in the climate system. To Ed Brook for joining my committee on such short notice and Jim McManus for serving as my GCR. Though Peter Clark did not serve on my final committee, I thank him for pushing me to know more about paleoclimate.

I really enjoyed spending time with all the guys I shared an office with over the years including, Shaun Marcott, Jeremy Shakun, Lica Ersek, Jon Hornung, Josh Cuzzone, and especially Cody Beedlow for putting up with me constantly showing him what I was working on at the time. Chuck Sears and Tom Leach have done an amazing job keeping our super computers running smoothly and keeping us on the cutting edge of technology.

I am greatly indebted to my parents who have always been unwaveringly supportive of me. My success in life is largely based on what they've provided for me. To my cousin Christina for being the big-cousin-role-model I needed. I would not be where I am today without the people who educated and molded me into a scientist. Annie Buchwald as my high school science teacher is in no small part directly responsible for my interest in science, whereas Chris Amrhein and Tom Meixner fostered that interest in college and set me on the path to becoming a scientist.

Finally, I thank my wife Debbra for everything ranging to listening about the latest computers to constantly having to hear about ENSO and other funny acronyms. She has been amazingly supportive and a wonderful proofreader and editor of almost everything I've written. I couldn't have accomplished what I have or be who I am without her.

CONTRIBUTION OF AUTHORS

Steve Hostetler oversaw and provided guidance for each chapter as well as playing a pivotal role in helping revise each paper. David Pollard provided detailed text used in the model description of Chapter 2 and helped answer questions about the nuts and bolts of the model. Both Chapter 2 and Chapter 3 evaluate aspects of the model, GENMOM, which David Pollard developed. Andreas Schmittner helped guide the analysis of the ocean model evaluation in Chapter 2.

TABLE OF CONTENTS

TABLE OF CONTENTS (Continued)

Page

TABLE OF CONTENTS (Continued)

Page

LIST OF FIGURES

LIST OF FIGURES (Continued)

LIST OF FIGURES (Continued)

LIST OF TABLES

For Debbra

Simulating Past, Present, and Future Changes in ENSO: a Model Evaluation and Data-model Comparison

Chapter 1: Introduction

1.1 Motivation

This thesis was largely motivated by an interest of how the El Niño/Southern Oscillation (ENSO) could possibly change in a warming world. The 1982-83 and 1997-98 El Niño events were the strongest in the historical record, leaving scientists asking if ENSO is strengthening because of anthropogenic global warming (Fedorov and Philander, 2000). Numerous modeling studies have used climate models to provide insight into potential changes in ENSO, yet the state-of-the-art models do not reveal a consensus for the response of ENSO to increasing atmospheric CO_2 (Guilyardi, 2006; Merryfield, 2006). The models are divided; roughly half indicate a stronger ENSO while the other half indicate a weaker ENSO in a warmer world, where only a few are statistically significant. The introduction of a new model, GENMOM, provides an opportunity to test if this particular model simulates a stronger or weaker ENSO in response to increased atmospheric CO_2 scenarios. However, adding just one more model to either category likely isn't that useful. Following the approach of the upcoming Fifth Assessment Report of the Intergovernmental Panel on Climate Change (IPCC AR5), model simulations are performed for known past climates to judge if the model is capable of simulating a climate significantly different than the present (Taylor et al., 2011). If climate models are unable to capture known variations in past ENSO, how much can we trust them to predict future changes in ENSO?

Evidence from corals (Tudhope et al. 2001; McGregor and Gagan, 2004) and lake sediment cores (Rodbell et al., 1999; Moy et al., 2002) reveal a 15 – 60% reduction in ENSO strength occurred during the mid-Holocene (~6,000 years ago). Changes in the seasonal timing of solar radiation and trace gas concentrations are well known for the mid-Holocene and are applied to climate models to simulate the past with the 15 – 60% reduction in ENSO strength as a target. By simulating past ENSO, and understanding the mechanisms driving observed changes, models help inform the interpretation of future ENSO simulations and build confidence that the model is capable of simulating climate different from the present.

The goal of this thesis is to simulate climate from the Last Glacial Maximum to the present in order to analyze changes in ENSO strength, such that understanding the mechanisms responsible for those changes inform our simulations of future ENSO (Chapter 5). Since GENMOM is a new model, it must first be evaluated to ensure it produces a reasonable modern climate (Chapter 2) and simulates ENSO with sufficient fidelity (Chapter 3). Once the model is proven to produce an accurate modern climate, it is then used to simulate past climates. Model output is compared to reconstructed proxy data to ensure the simulated past climate is plausible (Chapter 4).

1.2 Publication status

As of writing, Chapter 2 has been published in Geoscientific Model Development, while the other chapters are in preparation to be submitted to journals yet to be determined.

1.3 References

Fedorov, A. V., and Philander, S. G.: Is El Niño Changing? Science, 288, pg 1997-2002, doi: 10.1126/science.288.5473.1997, 2000.

Guilyardi, E.: El Niño–mean state–seasonal cycle interactions in a multi-model ensemble. Climate Dynamics, 26, 329–348, 2006.

McGregor, H.V. and Gagan, M.K.: Western Pacific coral δ18O records of anomalous Holocene variability in the El Nino-Southern Oscillation. Geophysical Research Letters, 31, doi:10.1029/2004GL019972, 2004.

Merryfield, W. J.: Changes to ENSO under CO2 doubling in a multimodel ensemble. J. Climate, 19, 4009–4027, 2006.

Moy, C.M., Seltzer, G.O., Rodbell, D.T., Anderson, D.M.: Variability of El Nino/ Southern Oscillation activity at millennial timescales during the Holocene epoch. Nature, 420, 162– 165, 2002.

Rodbell, D. T., Seltzer, G.O., Anderson, D.M., Abbott, M.B., Enfield, D.B., and Newman, J.H.: An ~15,000-year record of El Nino-driven alluviation in southwestern Ecuador. Science 283, 516–520, 1999.

Tudhope, A.W., Cilcott, C.P., McCulloch, M.T., Cook, E.R., Chappell, J., Ellam, R.M., Lea, D.W., Lough, J.M., Shimmield, G.B.:Variability in the El Nino–Southern Oscillation through a glacial–interglacial cycle. Science, 291, 1511– 1517, 2001.

Chapter 2: Evaluation of a present-day climate simulation with a new coupled atmosphere-ocean model GENMOM

J. R. Alder[1], S. W. Hostetler[2], D. Pollard[3] and A. Schmittner[4]

[1]Oregon State University, Department of Geosciences, Corvallis, OR 97331, United States

[2]US Geological Survey, Oregon State University, Department of Geosciences, Corvallis, OR 97331, United States

[3]Pennsylvania State University, EMS Earth and Environmental Systems, University Park, PA 16802, United States

[4]Oregon State University, College of Ocean and Atmospheric Sciences, Corvallis, OR 97331, United States

Geoscientific Model Development, 4, 69-83, doi:10.5194/gmd-4-69-2011

2.1 Abstract

We present a new, non-flux corrected AOGCM, GENMOM, that combines the GENESIS version 3 atmospheric GCM (Global ENvironmental and Ecological Simulation of Interactive Systems) and MOM2 (Modular Ocean Model version 2) nominally at T31 resolution. We evaluate GENMOM by comparison with reanalysis products (e.g, NCEP2) and three models used in the IPCC AR4 assessment. GENMOM produces a global temperature bias of 0.6 °C. Atmospheric features such as the jet stream structure and major semi-permanent sea level pressure centers are well simulated as is the mean planetary-scale wind structure that is needed to produce the correct position of stormtracks. Most ocean surface currents are reproduced except where they are not resolvable at T31 resolution. Overall, GENMOM captures reasonably well the observed gradients and spatial distributions of annual surface temperature and precipitation and the simulations are on par with other AOGCMs. Deficiencies in the GENMOM simulations include a warm bias in the surface temperature over the southern oceans, a split in the ITCZ and weaker-than-observed overturning circulation.

2.2 Introduction

We present a new non-flux corrected coupled atmosphere-ocean general circulation model (AOGCM), GENMOM, which combines GENESIS version 3 (Global ENvironmental and Ecological Simulation of Interactive Systems) and MOM2 (Modular Ocean Model version 2) general circulation models. Both models have been used widely in climate studies that demonstrate their overall ability to produce climate simulations that are in agreement both with observations and with similar models. GENESIS version

1 was developed initially in 1989 at the National Center for Atmospheric Research (NCAR) with a focus on linking terrestrial physical and biophysical processes with the atmosphere to provide a model that could be applied to simulate paleoclimate and possible future climates under global warming.

GENESIS version 1 was released in 1991 (Thompson and Pollard, 1995) and included a land-surface transfer model (LSX) and an atmospheric general circulation model derived from NCAR CCM1. GENESIS version 2 was released in 1995 and included many improvements ranging from new prognostic cloud amounts, the use of hybrid vertical coordinates, the inclusion of gravity wave drag, and additional improvements in LSX (Thompson and Pollard, 1997; Pollard and Thompson, 1997).

GENESIS version 3 expands on version 2 by including the NCAR CCM3 radiation code. The ocean can optionally be represented by fixed sea surface temperatures, a slab or mixed layer or by the MOM2 ocean general circulation model. MOM also has a long history of use and development also spanning back to the early 1990s and is used as the ocean component in many other AOGCMs (Pacanowski, 1996). Our current version of GENMOM uses T31 (~3.75° x 3.75° latitude and longitude) horizontal resolution for both the atmosphere and ocean to balance computational requirements needed for long simulations with the ability to simulate important features of the general circulation. A higher resolution version with 2^{o} x 2^{o} ocean and LSX with T31 atmosphere is under development.

We evaluate a simulation of modern climate using observational and reanalysis data and we compare GENMOM surface temperature and precipitation with three other AOGCMs evaluated in the World Climate Research Programme (WCRP) Coupled Model

Intercomparison Project phase 3 (CMIP3, Meehl et al., 2007a), a multi-model dataset that was subsequently used in the IPCC AR4 (described in Table 2.1, Randall et al., 2007). A full description of GENESIS and MOM2 as well as their coupling is provided in Section 2, atmospheric and oceanic results from a modern climate simulation are presented in Section 3, and concluding remarks follow in Section 4.

2.3 GENMOM description

2.3.1 GENESIS description

GENESIS has been developed with emphasis on terrestrial physical and biophysical processes, and suitability for paleoclimatic experiments. Earlier versions of GENESIS are described by Thompson and Pollard (1995, 1997) and Pollard and Thompson (1994, 1995, 1997), and have been applied and tested in a wide range of modern and paleoclimate applications including the Paleoclimate Modeling Intercomparison Project (e.g., Pollard et al., 1998; Joussaume et al., 1999; Pinot et al., 1999; Beckmann et al., 2005; Miller et al., 2005; Ruddiman et al., 2005; Bice et al., 2006; DeConto et al., 2006, 2008; Hostetler et al., 2006; Poulsen et al., 2006, 2007; Horton et al., 2007).

The nominal GENESIS resolution is spectral T31 (3.75° x 3.75°) with 18 vertical sigma coordinate levels, 4 of which are above the tropopause. Spectral transform dynamics are used for mass, heat and momentum (Williamson et al., 1987). A semi-Lagrangian transport in grid space is used for water vapor (Williamson and Rasch, 1989). Convection in the free atmosphere and in the planetary boundary layer is treated using an explicit sub-grid buoyant plume model similar to, but simpler than, Kreitzberg and Perkey (1976) and Anthes (1977, section 4). Stratus, convective and anvil cirrus clouds

Table 2.1 Three AOGCMs used in the IPCC AR4. T indicates the horizontal resolution using spectral truncation. L indicates the number of levels used in the model.

Model	Modeling Center, Country	Atmosphere Resolution	Ocean Resolution
GFDL CM 2.0	U.S. Department of Commerce/National Oceanic and Atmospheric Administration (NOAA)/Geophysical Fluid Dynamics Laboratory (GFDL), USA	2.0° x 2.5° L24 GFDL GAMDT, 2004	0.3°–1.0° x 1.0° Gnanadesikan et al., 2004
MPI ECHAM5	Max Planck Institute for Meteorology, Germany	T63 (~1.9° x 1.9°) L31 Roeckner et al., 2003	1.5° x 1.5° L40 Marsland et al., 2003
NCAR CCSM 3.0	National Center for Atmospheric Research, USA	T85 (1.4° x 1.4°) L26 Collins et al., 2004	0.3°–1° x 1° L40 Smith and Gent, 2002

are predicted using prognostic 3-D water cloud amounts, (Smith, 1990; Senior and Mitchell, 1993) and clouds are advected by semi-Lagrangian transport and mixed vertically by convective plumes and background diffusion.

The land-surface transfer model, LSX, accounts for the physical effects of vegetation (Pollard and Thompson, 1995). Up to two vegetation layers (trees and grass) can be specified at each grid point, and the radiative and turbulent fluxes through these layers to the soil or snow surface are calculated. A six-layer soil model extends from the surface to 4.25 m depth, with layer thicknesses increasing from 5 cm at the top to 2.5 m at the bottom. Physical processes in the vertical soil column include heat diffusion, liquid water transport (Clapp and Hornberger, 1978; Dickinson, 1984), surface runoff and bottom drainage, uptake of liquid water by plant roots for transpiration, and the freezing and thawing of soil ice. A three-layer snow model, which includes fractional area cover when the snow is thin, is used for snow cover on soil, ice-sheet and sea-ice surfaces. A three-layer sea-ice model accounts for local melting, freezing, fractional sea-ice cover (Semtner, 1976; Harvey, 1988), and includes dynamics associated with wind and ocean current using the cavitating-fluid model of Flato and Hibler (1992). Version 3 of GENESIS (Zhou et al., 2008; Kump and Pollard, 2008) incorporates the NCAR CCM3 radiation code (Kiehl et al., 1998) and the ocean is represented by the MOM2 ocean general circulation model (Pacanowski, 1996).

2.3.2 MOM2 description

MOM2 was developed by the Geophysical Fluid Dynamics Laboratory (GFDL) in the early 1990s, but builds off previous work that began back in 1969 (Pacanowski, 1996). MOM2 is a finite difference implementation of the primitive equations of ocean circulation based on the Navier-Stokes equations with the Boussinesq, hydrostatic, and rigid lid approximations (Bryan, 1969). The Boussinesq approximation invokes constant density with depth, with the exception of terms that contain gravity, thereby reducing computational complexity. The hydrostatic approximation assumes that vertical pressure gradients are density driven. A nonlinear equation of state couples temperature and salinity to fluid velocity. An insulated lateral boundary is used such that no temperature or salinity flux is exchanged between ocean and land cells. Unlike the sigma levels used for atmospheric altitude in GENESIS, MOM uses a fixed z-axis for depth, which simplifies the equations used in the finite difference representation. Our version of MOM2 uses 20 unevenly spaced vertical levels that become progressively thicker with depth, so that the uppermost ocean layers are well resolved. The topmost level is 25 m thick, while the bottommost level is ~660 m thick. A horizontal resolution of 3.75° x 3.75° is used to match the atmospheric T31 resolution. The hybrid mixing scheme isopycmix is used with a prescribed vertical viscosity coefficient of 0.1 cm^2s^{-1} and a prescribed vertical diffusion coefficient of 0.35 cm^2s^{-1}. Although the Gent-McWilliams mixing scheme (Gent and McWilliams, 1990) is available in MOM2, it was not used in this study.

2.3.3 GENMOM coupling

To simplify the coupling between the atmosphere and ocean, both the GCMs are implemented on essentially the same T31 grid. In MOM2, the latitudinal grid spacing is not exactly T31, but is adjusted with a cosine-stretching factor (Pacanowski, 1996) to closely approximate T31. GENESIS has a 30-min timestep, and MOM2 has a 6-h timestep for scalar fields. The two models interact in an essentially synchronous manner, communicating every 6 hours: 6-h averages of the surface fluxes of heat, water and momentum are passed from GENESIS to MOM2, and MOM2 is run through one 6-h scalar timestep and the updated SSTs are passed back to GENESIS and used to run it for the next 6 hours. Sea ice is treated within the LSX module of GENESIS. Under sea ice, fluxes between the base and the uppermost ocean layer are passed to MOM2. Continental freshwater river runoff is globally averaged and spread over the world ocean. The T31 version of GENMOM simulates ~22 yr per calendar day on an 8-CPU Linux server. GENMOM coupled to MOM2 has previously been used by Zhou et al. (2008) to investigate warm Cretaceous climates; however, their study focused mainly on paleoclimates and water isotopic ratios, and not on modern climatology.

2.4 Simulation of the present-day climate

We analyze the annual and seasonal climatologies of the last 30 years of a 700-year GENMOM simulation. Analysis of ocean temperature indicates that spin up of the model was suitably achieved after 400 years. Over the last century of the simulation the deep ocean (>1,000 m) warmed by ~0.002 °C/decade, the mid layers (200 m - 1,000 m) warmed by ~0.003 °C/decade and the surface temperature was essentially free of drift. We prescribed atmospheric CO_2 concentration at 355 ppmV, near the mean value for the 1981-2005 climatology period. GENMOM was initialized with a latitudinal-dependent temperature profile and ocean salinity was uniformly prescribed at 35 ppt.

GENMOM input files for topography, bathymetry, and land-ocean mask were derived by interpolating the ICE-4G model (Peltier, 2002) reconstruction from 1° x 1° to T31 resolution. Ice-sheet cover and thickness is prescribed by interpolating the ICE-4G model reconstruction to T31. To maintain numerical stability, over the northernmost

Arctic Ocean cells in MOM2 we smooth the bathymetry field derived from ICE-4G with a 9-cell moving window. At T31 horizontal resolution the Bering Strait is closed. Modern values for the distribution of vegetation (Dorman and Sellers, 1989), soil texture (Webb et al., 1993) and freshwater lakes (Cogley, 1991) are prescribed. The use of ICE-4G orography to derive global topography, bathymetry, and ice-sheet extent is based on our goal of streamlining the configuration of GENMOM for paleoclimate applications.

2.4.1 Validation datasets and input files

To evaluate the GENMOM atmospheric fields we use the NOAA NCEP Reanalysis 2 data set (NCEP2, Kanamitsu, et al., 2002) for the standard climatology period of 1981 - 2005 unless otherwise specified. Although NCEP2 is comprised of observed and derived data it provides an internally consistent dataset with which to evaluate our model. SST data are derived from the NOAA Optimum Interpolation Sea Surface Temperature V2 (OI SST, Reynolds, et al., 2002), which is a 1° x 1° gridded dataset based on combining in situ measurements and satellite observations. We use a climatology period of 1982-2005 for OI SST, because 1982 is the first full year for which the data are available. Subsurface ocean temperatures were obtained from The World Ocean Atlas 2005 (WOA05, Locarnini et al., 2006), which is also a 1° x 1° gridded dataset of ocean temperature and salinity. We use the Hadley Ice and Sea Surface Temperature v1.1 (HadISST, UK Meteorological Office, 2006) for observed sea-ice extent data and to evaluate ocean surface currents and overturning, we use the German partner of the Estimating the Circulation and Climate of the Ocean dataset (GECCO), which is a 50-year (1950 – 2000) oceanography reanalysis (Köhl and Stammer, 2008, NCEP1, Kalnay et al., 1996).

2.4.2 Atmospheric fields

The zonally averaged profile of air temperature simulated by GENMOM is in overall agreement with the NCEP2 profile (Fig. 2.1). Seasonally, GENMOM simulates the meridional shift of peak insolation and warmest surface temperatures well although the modeled tropical warm region is slightly more compressed meridionally than that of the NCEP2 data. North of 30° N in both boreal winter and summer GENMOM produces a cold bias relative to NECP2 from the surface extending up to the mid-troposphere. An additional cold bias in the upper atmosphere is found over the polar region during boreal winter. A cold bias south of 60° S is present during austral summer and in the upper atmosphere during winter.

The summer and winter patterns and magnitudes of the annually averaged planetary jet stream structure are well captured by GENMOM (Fig. 2.2). In both winter hemispheres the core of the jetstream (at ~200 hPa) and related upper level winds (500 hPa) are slightly enhanced relative to those of the NCEP2 data. These minor mismatches notwithstanding, the overall structure of the simulated jetstream suggests that GENMOM produces a realistic mean planetary-scale wind structure that is essential to the related positioning of the stormtracks.

GENMOM simulates the positions of the seasonally persistent planetary-scale ridges and troughs and thus the resulting upper atmospheric flow and 500 hPa geopotential heights (Fig. 2.3a-d). During boreal winter, the ridge over western North America is shifted eastward in GENMOM relative to observations resulting in the eastward displacement of the associated trough over northern Canada and the North Atlantic and slightly more zonal flow than that of the NCEP2 data (Fig. 2.3b). The 500

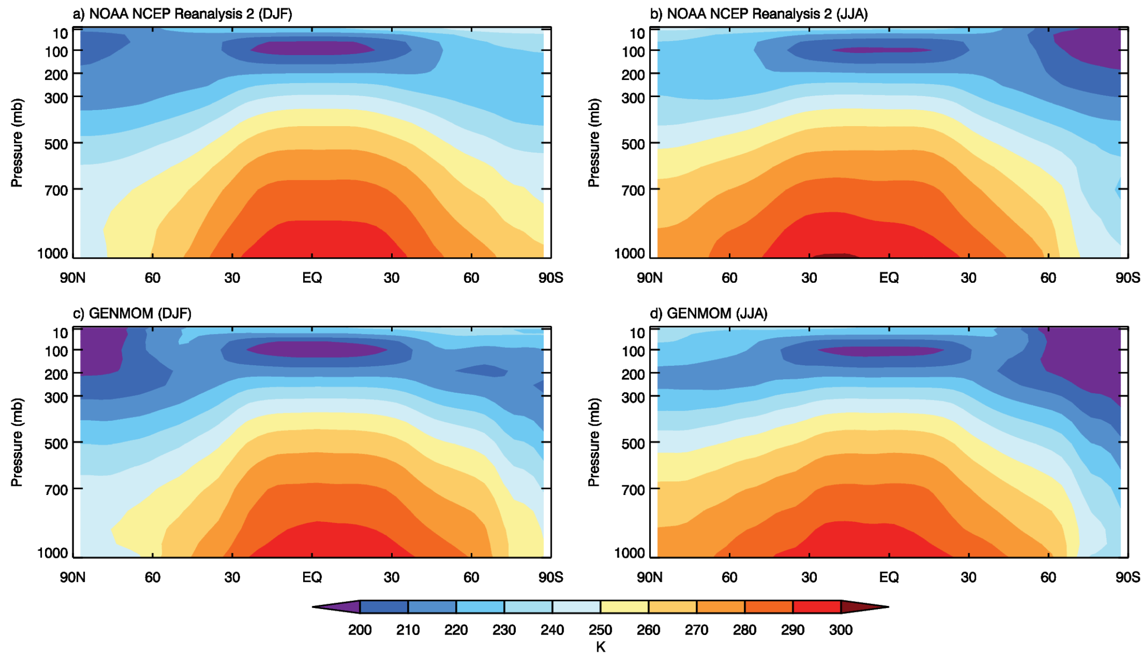

Figure 2.1 Mean-annual zonal averaged atmospheric temperature profiles. a) Observed (NCEP2, 1981 – 2005) December, January, February (DJF), b) Observed June, July, and August (JJA), c) GENMOM DJF, d) GENMOM JJA.

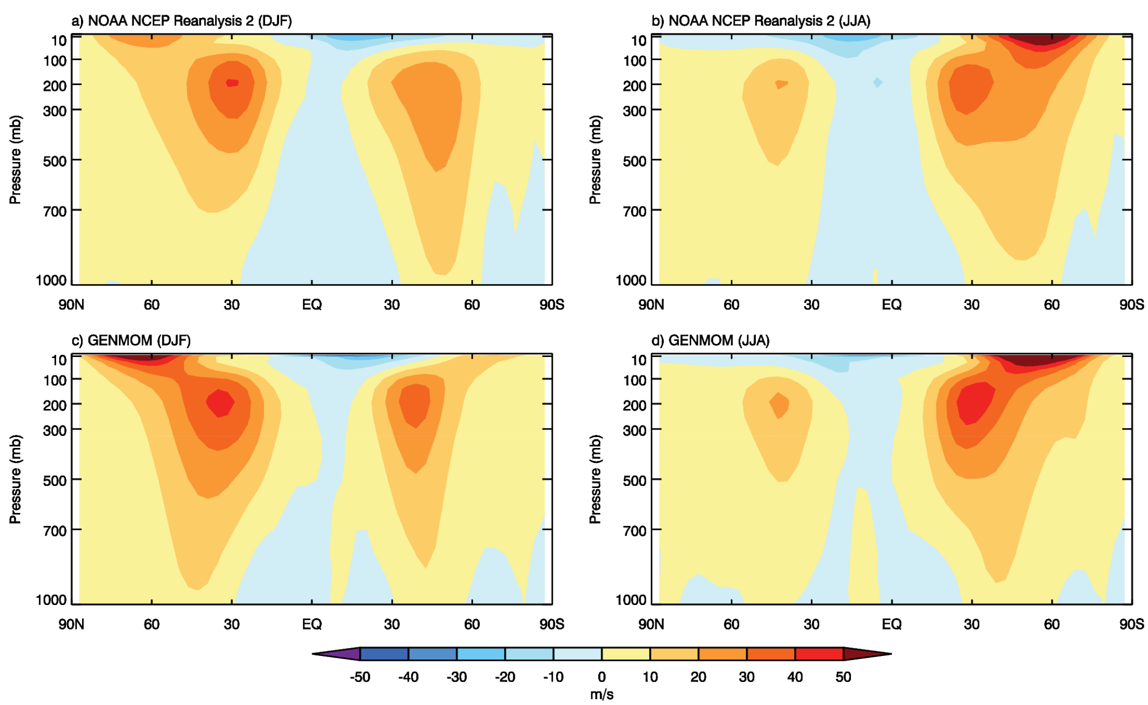

Figure 2.2 Winter (DJF) and summer (JJA) zonally averaged eastward wind velocity. a) Observed (NCEP2, 1981 – 2005) DJF, b) Observed JJA, c) GENMOM DJF, d) GENMOM JJA.

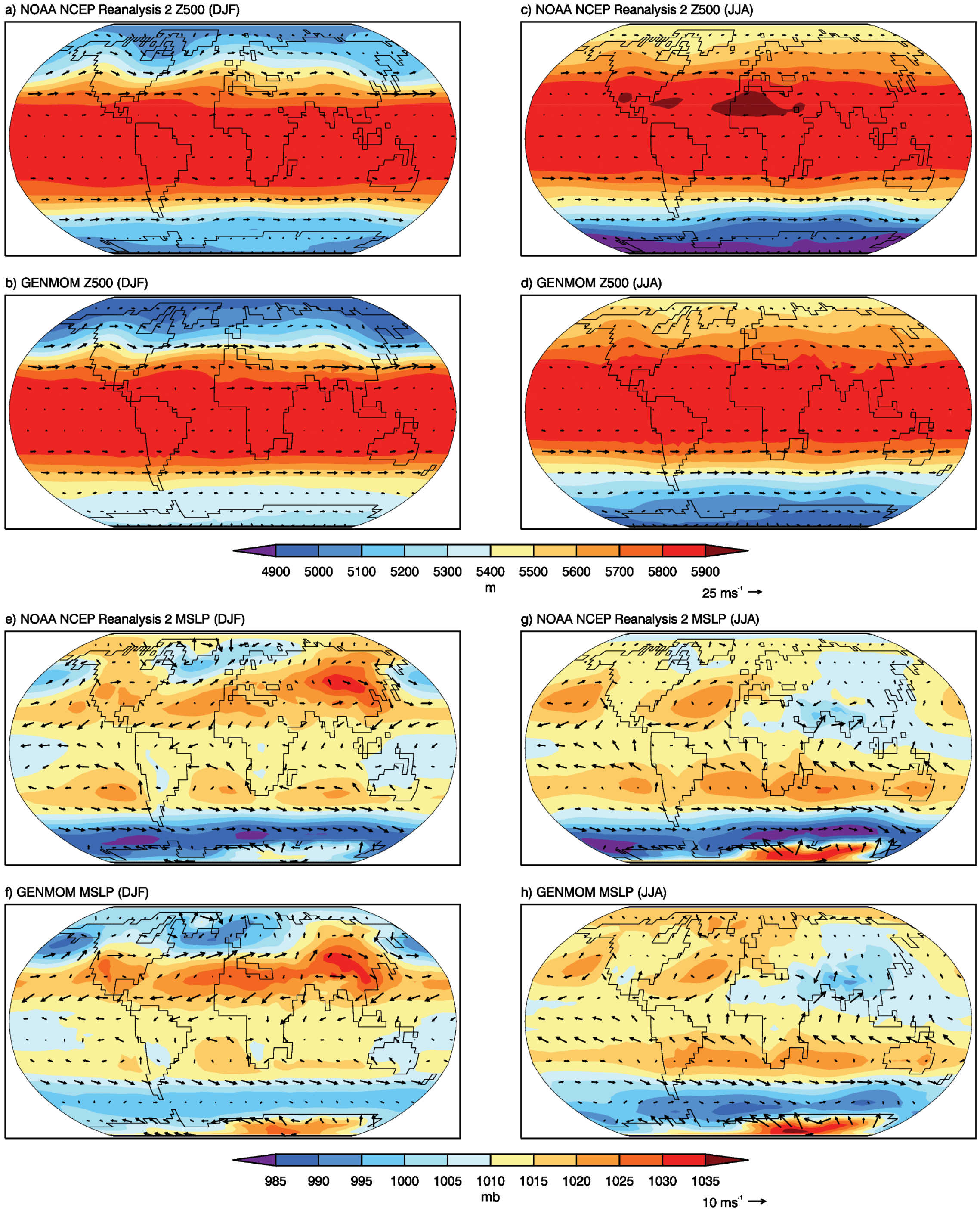

Figure 2.3 500 hPa geopotential height (Z500, a-d) and mean sea level pressure (MSLP, e-h) with wind vectors for both winter (DJF) and summer (JJA).

hPa heights over North America and Eurasia are lower than those of the NCEP2 data resulting in reduced wind velocities, particularly over eastern North America and the North Atlantic. In the southern hemisphere (SH), austral summer 500 hPa heights are well simulated but wind velocities associated with the westerlies are somewhat weaker than NCEP2 due to the lower pressure gradient over the Southern Ocean and Antarctica and the lack of actual topographic forcing due to the resolution of the model.

During boreal summer, the ridge over western North America is correctly placed in GENMOM, but the amplitude of the ridge and the related downstream trough is greater than that of the NCEP2 data (Fig. 2.3c). Heights in the region extending east of the Mediterranean and across India and China appear modestly lower than observed; however, part of the apparent discrepancy stems from values that are just above or just below the color breaks in the plotting scales.

The observed spatial pattern of the semi-permanent sea level pressure (MSLP) cells is captured by GENMOM with some regional differences (Fig. 2.3e-h). During boreal winter GENMOM simulates lower-than-observed MSLP in the Aleutian and Icelandic lows. As a result, surface wind velocities are enhanced around the pressure centers and over North America. Stronger-than-observed westerly winds across southern Europe are simulated by GENMOM as a result of the enhanced Icelandic low and the cold temperature bias in the Norwegian Sea. In the SH (austral summer), surface pressure and winds are comparable with those of the NCEP2 but GENMOM simulates a weaker-than-observed subtropical high and associated anticyclonic wind flow over the eastern Pacific off the coast of South America (Fig. 3e,f). This deficiency in turn affects the magnitude of the northward wind along the coast and the strength of convergence and westerly trade winds in the ITCZ. Over the southern ocean, the simulated gradient of MSLP is weaker and more diffuse than that of NCEP2 resulting in lower surface wind velocity, which affects the location and strength of circulation around Antarctica.

The boreal summer MSLP pressure patterns and wind velocities in both hemispheres are well captured by GENMOM (Fig. 3g,h). The northern hemisphere (NH) subtropical highs are well placed, but slightly weaker than NCEP2; the associated wind velocities are similar to those of NCEP2. MSLP and wind velocities in the tropics and the SH (austral winter) are also well simulated by GENMOM; however, as is the case with DJF, the JJA high-pressure anticyclones are somewhat weaker than observed. Again, the associated anticyclonic flow around the subtropical highs is too weak which contributes to a weakened South Pacific Gyre. The SH westerly winds are simulated to be too weak, presumably due to coarse resolution topography, which will influence ocean overturning.

2.4.3 Surface temperature

The simulated global mean-annual 2 m air temperature is 278.3 K, in good agreement with the NCEP2 value of 278.9 K. Over land, the simulated temperature is 1.3 K colder than observed and over the oceans simulated temperature is 0.6 K warmer than observed. GENMOM captures the observed meridional temperature and temperatures over topographic features resolved by the model such as the Rocky Mountains, the Andes and the Himalayas, have regional temperatures that compare well with observations (Fig. 2.4b). The temperature bias over land and much of the ocean is similar in magnitude to other AOGCMs (Fig. 2.4c-d).

The cold bias over the Norwegian Sea reflects too much simulated sea-ice resulting from insufficient meridional overturning. Warm biases are found over Southern

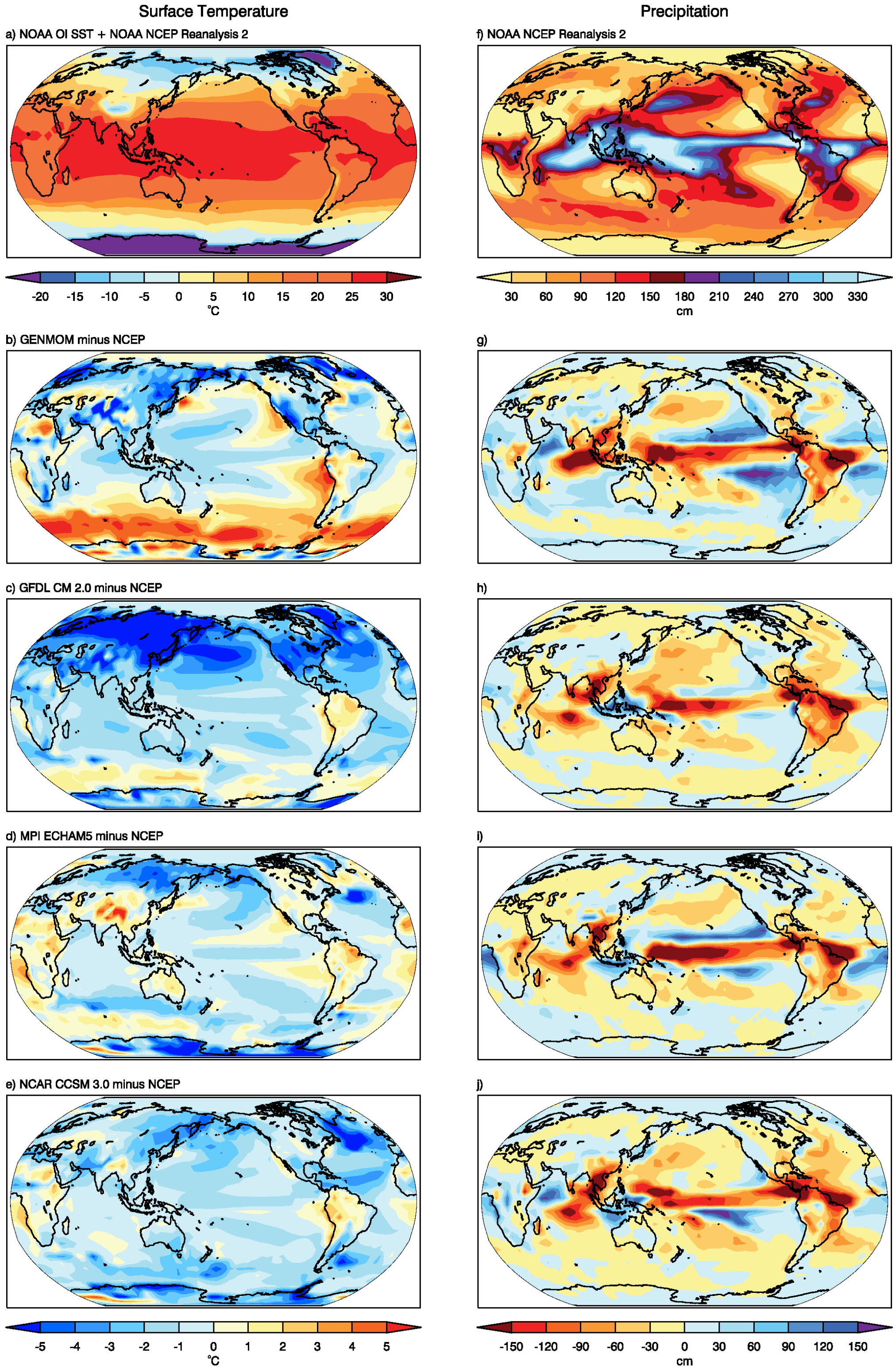

Figure 2.4 Annual surface temperature (a) with model anomalies (b-e) and annual total precipitation (f) with model anomalies (g-j) from GENMOM and three AOGCMs included in the IPCC AR4. Observed data are from NOAA NCEP Reanalysis 2 (over land) and NOAA OI SST (over sea). GENMOM 2 m air temperature and SST are for

model years 670-699 of the control equilibrium simulation. The three IPCC AR4 models are averaged over the last 30 years (1970 – 1999) of the Climate of the 20th Century experiment. All data are bi-linearly interpolated to a 5° x 5°grid. Anomalies are calculated as simulation – observation.

Ocean and in the upwelling region off the western coast of South America (Fig. 2.4a). The Southern Ocean bias is attributed primarily to weaker-than-observed sea level pressure gradient and attendant reduced westerly wind strength (Fig. 2.3) which results in weakened ocean overturning in the Ocean. The warm bias off the coast of South America is in part attributed to weaker shore-parallel winds associated with the reduced subtopical high (Fig. 2.3) and to the lack of resolution of finer scale currents in MOM. Lack of a California Current (~300 km wide) is similarly attributed to the T31 resolution of the models. Further discussion of the oceanic circulation is given in Section 3.5.

GENMOM captures the global patterns of the seasonal cycle of temperature but overestimates the amplitude over Greenland, South America, southeast United States and Australia and underestimates the amplitude over northern Africa, the western United States and much of Europe and Asia (Fig. 2.5). The model also simulates greater variability over some of the oceans, particularly in the mid latitudes.

2.4.4 Precipitation

GENMOM simulates global mean-annual precipitation reasonably well relative to the reanalysis data (Figs. 2.4g and 2.6). Notable exceptions are dry biases over Southeast Asia and South America. GENMOM also produces a double Intertropical Convergence Zone (ITCZ) in the tropical Pacific, which is characterized by displacement of precipitation maxima off the equator (Lin, 2007). The dry biases and the double ITCZ are common to other AOGCMs (Fig. 2.4h-j).

During DJF, the southern branch of the ITCZ simulated by GENMOM extends too far to the east, whereas during JJA, the northern branch of the ITCZ is compressed and extends too far to the north relative to observations. Lin (2007) attributes the double

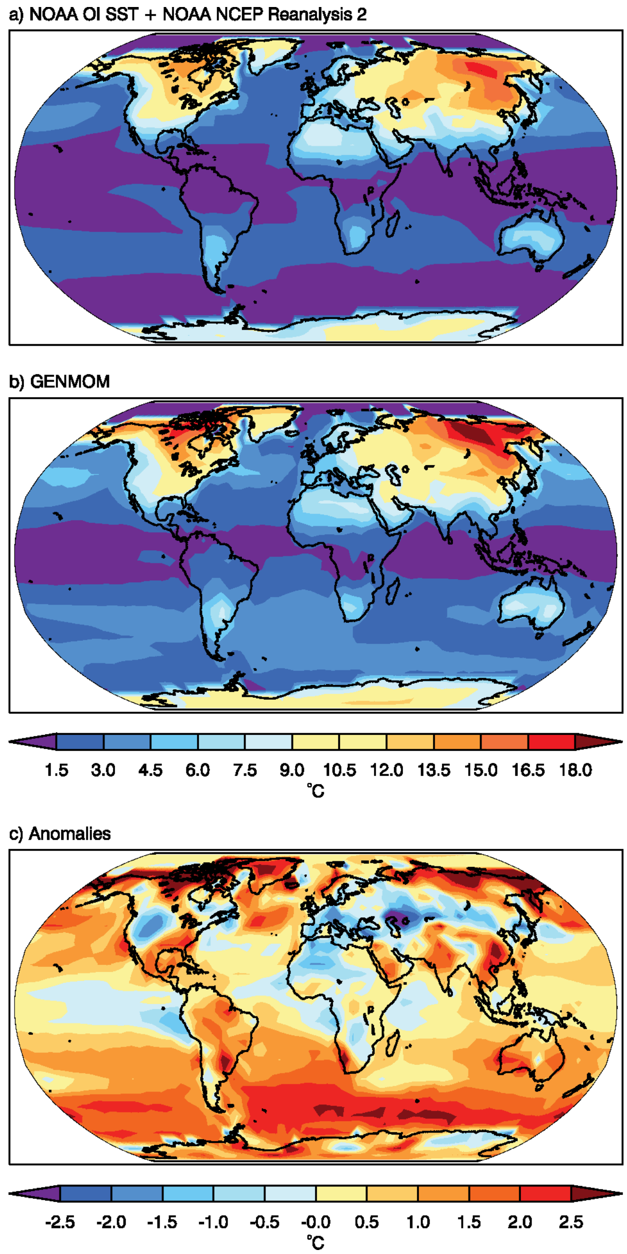

Figure 2.5 Observed and modeled seasonal cycle amplitude of surface temperature and anomalies. The amplitude of the seasonal cycle is calculated as the standard deviation of the 12 climatological months.

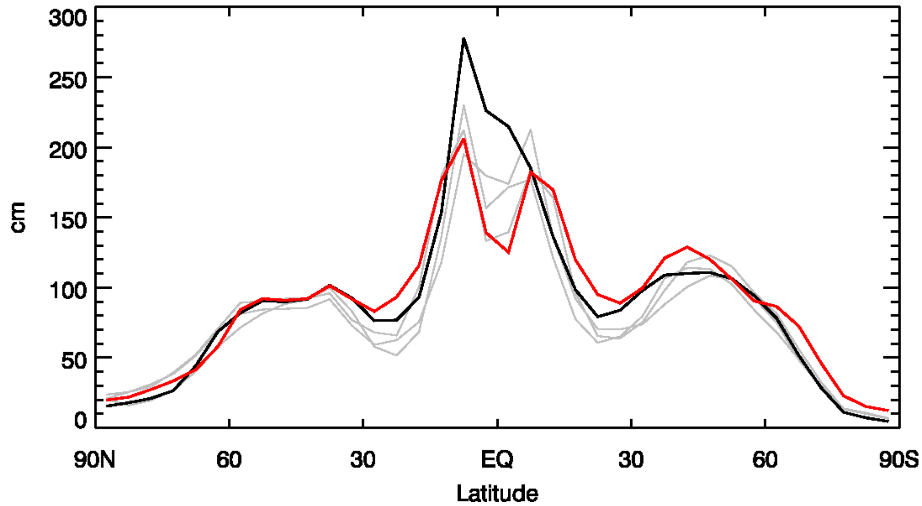

Figure 2.6 Zonal averaged annual precipitation for observations (black), GENMOM (red) and three IPCC AR4 models (gray). The IPCC AR4 models are averaged over the last 30 years (1970 – 1999) of the Climate of the 20th Century experiment.

ITCZ to: 1) excessive tropical precipitation, 2) high sensitivity of modeled precipitation and surface air humidity to SST, 3) a lack of sensitivity of cloud amount to precipitation, and 4) a lack of sensitivity of stratus cloud formation to SST. GENMOM produces a cold SST bias in the Pacific Basin along with a confined cold tongue, both of which Lin (2007) note as factors that result in a double ITCZ. Consistent with Lin (2007), GENMOM does not produce a double ITCZ when coupled to a slab ocean. The split ITCZ problem can potentially be resolved by improving resolution of tropical ocean-atmosphere feedbacks.

2.4.5 Oceanic fields

The global surface and subsurface patterns of ocean potential temperatures simulated by GENMOM are consistent with the WOA05 data (Fig. 2.7); however, anomalies reveal biases exceeding 2 °C (Fig. 2.7a), similar to other AOGCMs (Randall et al., 2007, Supplementary Materials, Pages 60-61). The warm bias in the near-surface of the Southern Ocean is consistent with the surface temperature anomalies shown in Fig. 2.4b. The Southern Ocean warm bias is attributed to weak ocean overturning and, perhaps, indicates the need for incorporating the Gent-McWilliams mixing scheme (Gent and McWilliams, 1990). The warm bias in the tropical ocean mid-depths is attributed to weakened simulated upwelling and the use of a relatively high vertical diffusion coefficient (0.35 cm^2s^{-1}) that is prescribed to maintain reasonable ocean overturning; too much heat is diffused from the surface to the mid-depths.

GENMOM captures the zonal distributions of salinity with depth both between and within the Atlantic and Indian + Pacific basins (Fig. 2.8). Salinity in the Indian + Pacific Oceans matches well to observations with much of the zonal bias being less than

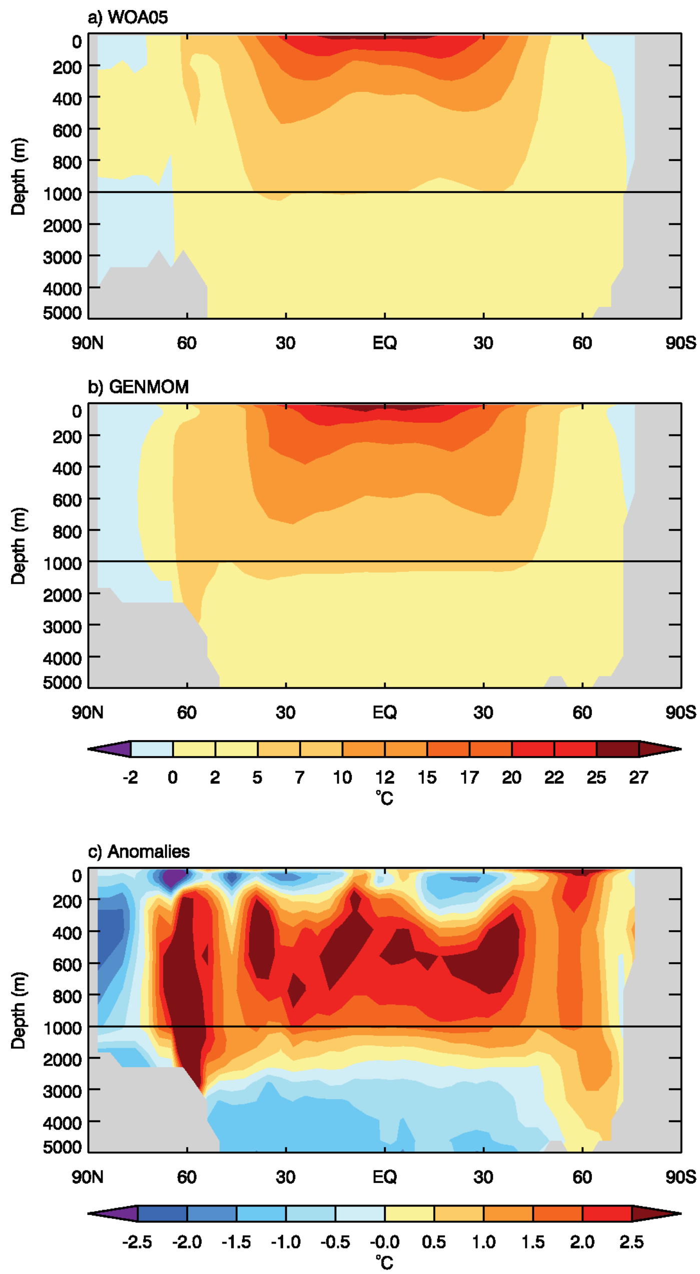

Figure 2.7 Mean-annual zonally averaged ocean potential temperature profile. a) Observed (WOA05), b) GENMOM, c) Anomalies, calculated as GENMOM - observed.

±0.2 PSS. Relative to the WOA05 data, in the Atlantic, GENMOM simulates lower salinity waters at high latitudes and higher salinity waters in the northern mid latitudes; the maximum centered on 30° N exceeds observations and the maximum at 30° S underestimates observations. A 1+ PSS salinity bias in the northern mid latitudes between 400 – 1,000 m is attributed to a build up of salinity in the Gulf of Mexico caused by weaker-than-observed circulation associated with the coarse resolution of ocean orography. Similarly, the low salinity bias north of 60° N is associated with reduced northward penetration of the North Atlantic Drift into the Arctic, again due to the coarse resolution of ocean orography, and weaker-than-observed Atlantic Meridional Overturning Circulation (AMOC). Similar to ocean temperature, the GENMOM salinity anomalies are comparable with those of other AOGCMs (Randall et al., 2007, Supplementary Materials, Pages 66-68).

We compare simulated global and basin ocean overturning for the full 300-year GENMOM with observations (Fig. 2.9). The last 30 years of the simulation coincidently displayed one of the weakest periods of overturning in the 300-yr simulation, so we use the full 300-year record as more representative because higher frequency (decadal) variability is smoothed out in the average. Globally, GENMOM produces overturning that is similar in pattern to that of the GECCO data. The most notable shortcoming in the GENMOM simulation is that the strength and depth of the Deacon Cell, which is characterized as deep clockwise meridional circulation in the Southern Ocean driven by windstress, are poorly captured. Wind velocities across the Southern Ocean are weaker-than-observed (Fig. 2.3) thereby failing to produce sufficient windstress to drive deep overturning (Toggweiler and Samuels, 1995; Sijp and England, 2009). The weak westerly

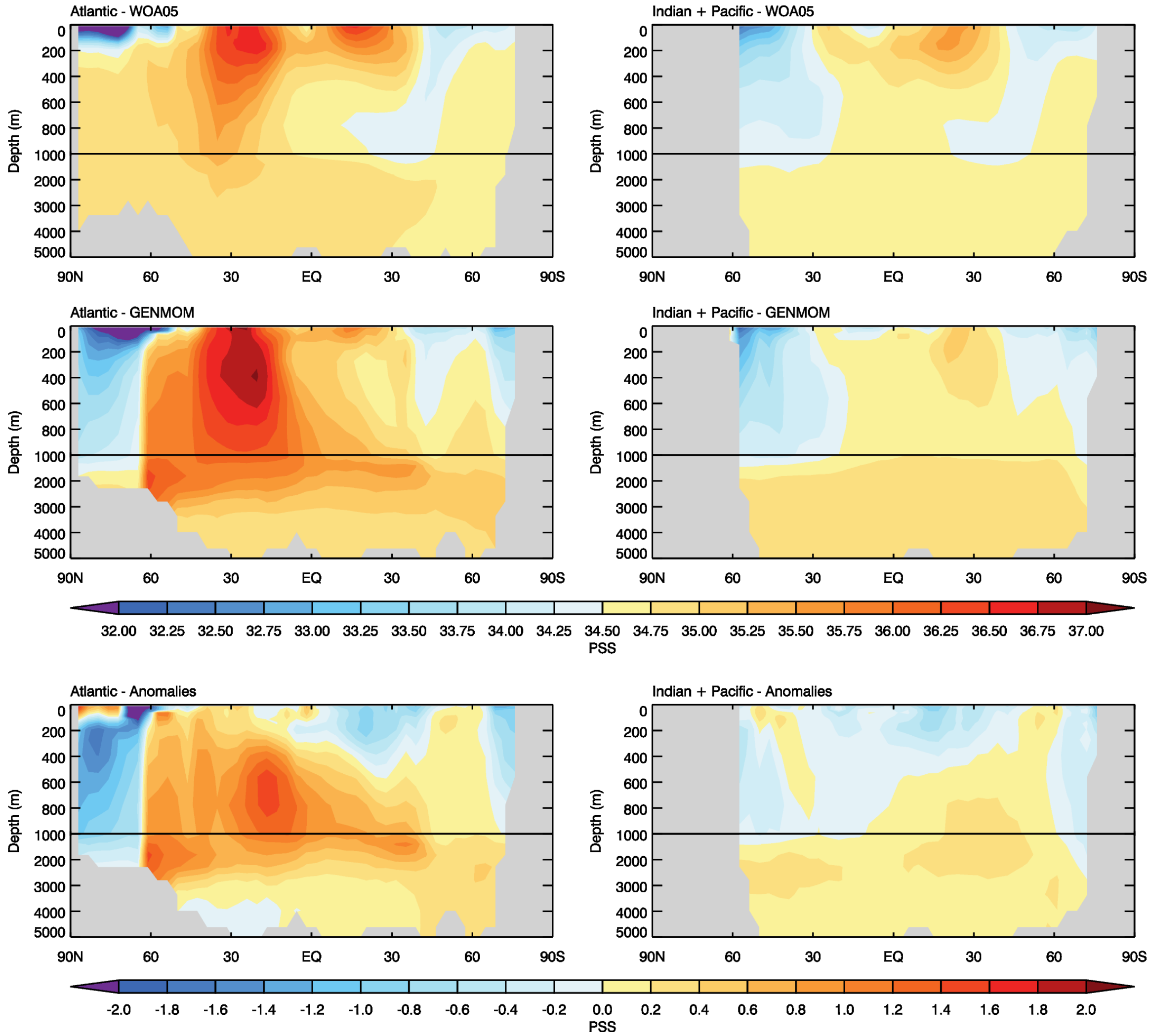

Figure 2.8 Mean-annual zonally averaged ocean salinity profile for both observed (WOA05) and simulated (GENMOM) for the Atlantic Ocean (left), Indian and Pacific Oceans (right), and anomalies between observed and simulated.

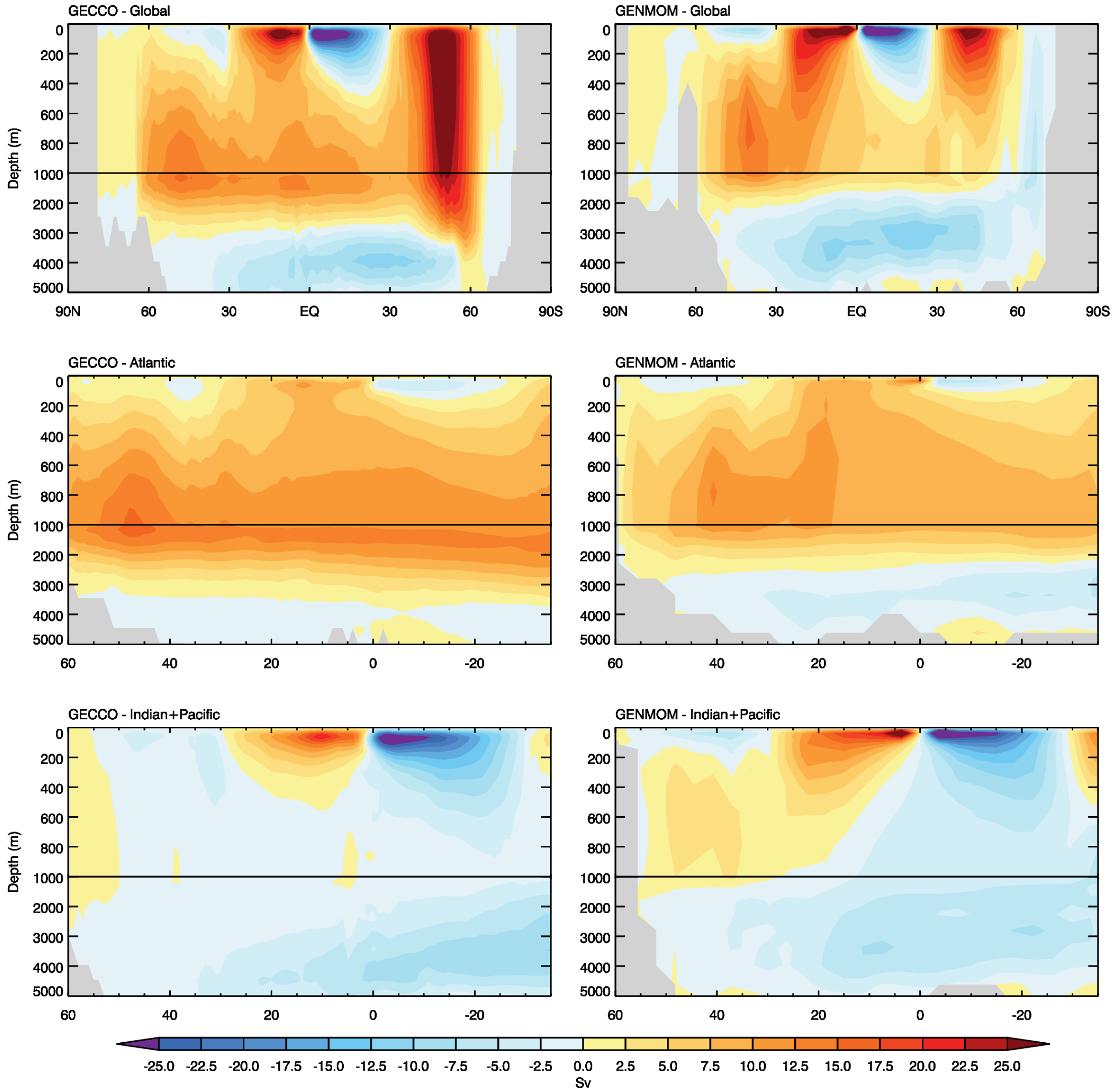

Figure 2.9 Ocean overturning for both observed (GECCO) and simulated (GENMOM, full 300-year simulation) globally (top), Atlantic Ocean (middle), Indian and Pacific Oceans (bottom).

winds are likely due to the coarse meridional resolution (Held and Phillipps, 1993; Tibaldi et al., 1990) and may also contribute to weak AMOC biases in non-flux corrected models with coarse atmospheric resolution, as found in earlier studies (Bryan et al., 2006; Schmittner et al., accepted). Failure to simulate the Deacon Cell also contributes to the warm Southern Ocean temperature bias by limiting the addition of upwelled cold waters.

The simulated AMOC is somewhat weaker in strength than that of the GECCO data. The maximum AMOC strength over the 300-year simulation is 14.5 ± 0.9 Sv, which is lower than the observed 16 - 18 Sv range. [The models used in the IPCC AR4 generally fall between 12 - 20 Sv (Meehl et al., 2007b; Schmittner et al., 2005).] The combined Indian Ocean and Pacific Ocean overturning matches well with observations with the exception that GENMOM simulates deeper-than-observed clockwise overturning in the northern tropics, which may imply the vertical diffusion coefficient is too high.

The major Atlantic surface currents are well simulated in GENMOM, with the exception of the Gulf Stream, which is too weak (Fig. 2.10). The Antarctic Circumpolar Current flowing through the Drake Passage is well resolved, as is the continuing flow to the South Atlantic Current. In the Pacific, the equatorial currents are well simulated, but the North Equatorial Counter Current is not present and the North Equatorial Current is weaker than that of the observations. The Kuroshio Current is well placed but slightly weaker than that of the observations. The California Current is absent from the GENMOM simulated surface currents. Both the Humboldt Current and Antarctic Circumpolar Current are weaker than observed. The strength of the Antarctic Circumpolar Current through the Drake Passage is ~35% weaker than the 119 Sv

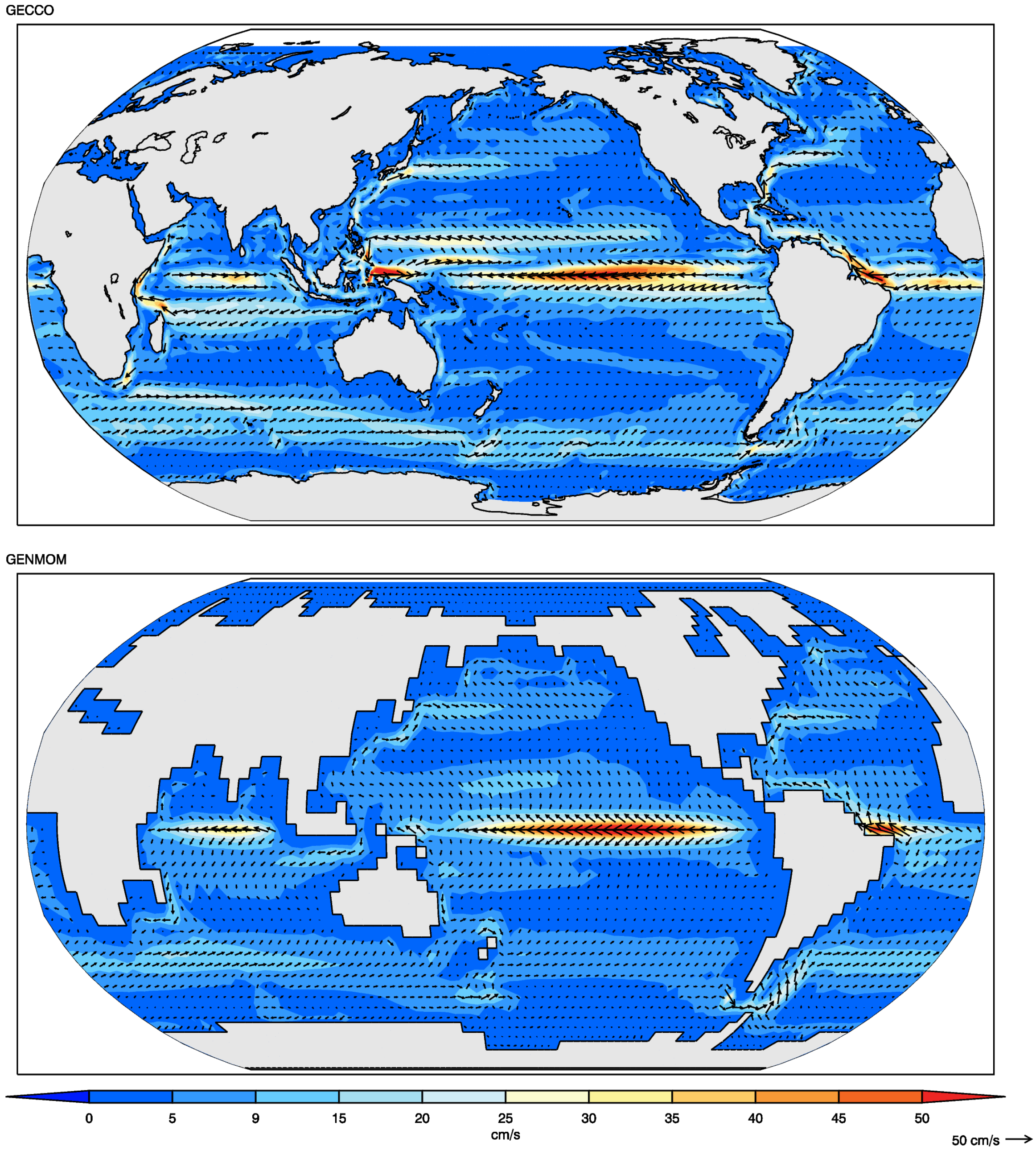

Figure 2.10 Annual global surface currents for both observations (GECCO) and GENMOM simulated.

estimated from the GECCO reanalysis. In the Indian Ocean, GENMOM simulates the Indonesian Throughflow well. The Indonesian Throughflow is 12.7 ± 0.8 Sv, compared to the observed estimates of 9.3 ± 2.5 Sv (Gordon et al., 1999) and 13.2 ± 1.8 Sv (Lumpkin and Speer, 2007).

Surface currents in the northern Indian Ocean are modulated by the monsoon, where currents flow westward during winter and eastward during summer. The annually averaged surface currents in Fig. 2.10 show westward flow dominating in GENMOM whereas eastward flow dominates in the observations. The reversal of the surface currents is most noticeable in GENMOM during winter and spring.

GENMOM reproduces the observed NH winter and summer sea-ice extent and concentration (Fig. 2.11). Sea ice extends too far into the Norwegian Sea during both winter and summer and too far into Hudson Bay during winter. The excessive sea-ice in the Norwegian Sea is likely due to the weakened AMOC, which does not transport enough warm, mid-latitude water northward. Sea ice is deficient around Antarctica during both seasons. The lack of extent and concentration is a direct result of the persistent warm temperature bias in the Southern Ocean.

2.5 Discussion

We present the first formal evaluation of the new AOGCM GENMOM, a non-flux corrected model comprised of GENESIS 3 atmospheric model, the MOM2 ocean model and LSX land-surface model. The spectral resolution of T31 for both atmosphere and ocean is used during this evaluation. The simulated global 2 m air temperature is 0.6 °C warmer over oceans and 1.3 °C colder over land. The jet stream structure and major planetary features of sea level pressure are well captured by the model. GENMOM

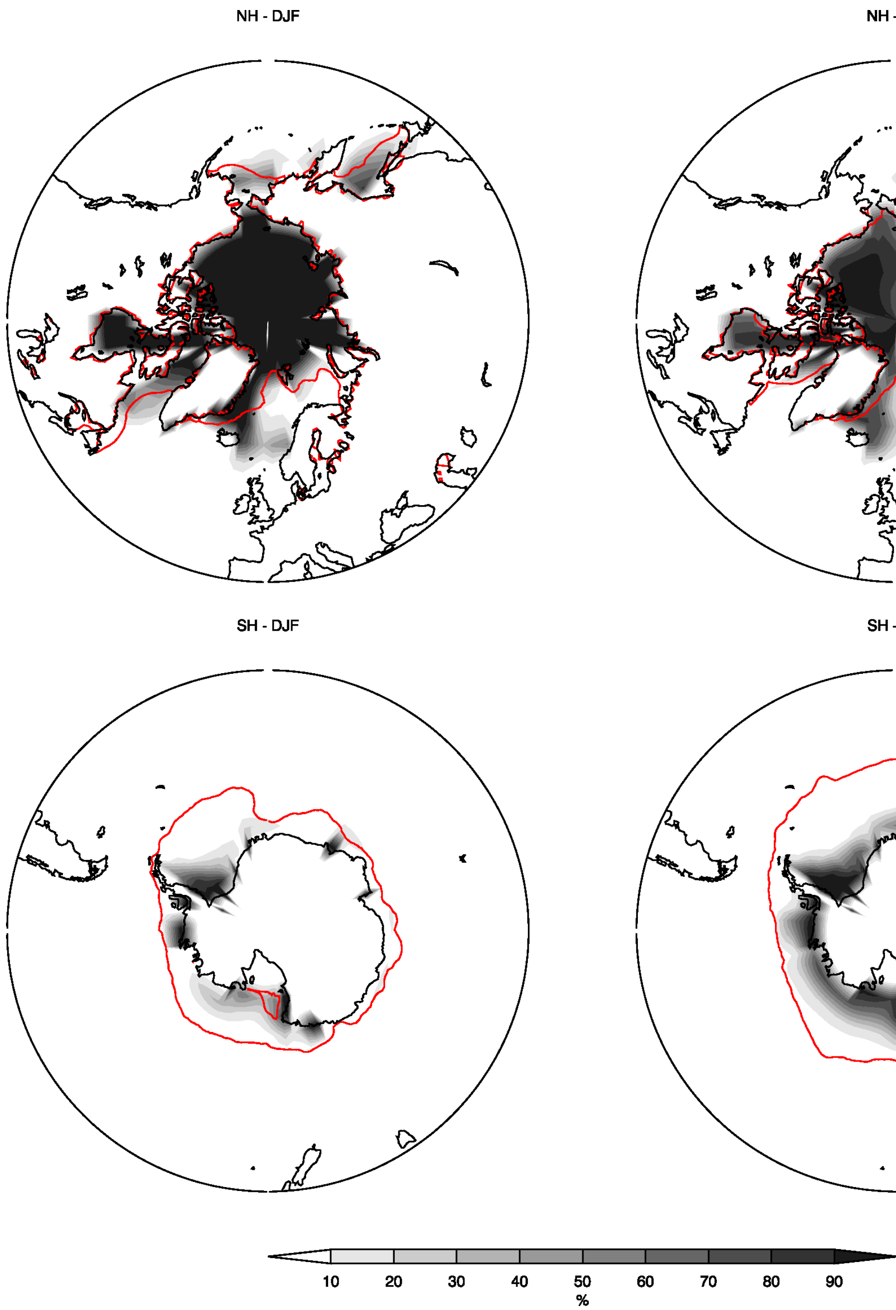

Figure 2.11 Fractional sea-ice extent. HadISST v1.1 15% observed contour plotted in red.

produces a realistic mean planetary-scale wind structure that is needed to produce the correct position of stormtracks. The 500 hPa ridges and troughs are well simulated, as are the seasonal surface pressure cyclones and anticyclones.

The annual surface temperature gradient, spatial distribution, and the annual distribution of precipitation compare well to observations and are on par with the three other AOGCMs. Cold SST anomalies in the Norwegian Sea are explained by excessive sea-ice in both winter and summer, which is in turn caused by weak Atlantic Ocean overturning. A warm bias in the Southern Ocean is attributed to a weak ocean overturning resulting in a poor simulation of the Deacon Cell, which suppresses associated cold water upwelling in the Southern Ocean. GENMOM fails to resolve adequately the South Pacific Gyre, which results in a warm SST bias in the eastern Pacific Ocean and weak anticyclonic atmospheric circulation around the gyre. GENMOM simulates a double ITCZ when coupled with the OGCM, which is not present when GENESIS is coupled to a slab ocean.

The global ocean temperature is generally well simulated, with the exception of a warm bias between 200 – 1000 m in the tropics and mid-latitudes. The warm bias is attributed to weak global overturning and the use of a high value of the vertical diffusion coefficient, which was needed to maintain realistic global ocean overturning. Salinity is generally well simulated, but with a fresh bias in the North Atlantic caused by underrepresentation of narrow channels (i.e., the Norwegian Sea) at T31 model resolution and a 1+ PSS salinity bias in the northern mid latitudes originating in the Gulf of Mexico. Ocean overturning is simulated with the correct spatial pattern, but is generally weaker-than-observed. We attribute the weak meridional ocean overturning to (i) weak and northwardly displaced westerly winds in the SH due to coarse topography and (ii) a narrow and shallow Drake Passage also due to coarse orography.

Most ocean surface currents are well simulated by GENMOM, with the exception of narrow currents such as the Gulf Stream and the Kuroshio Current that are weaker-than-observed again due to the coarse T31 resolution. Northern Hemisphere Sea-ice is well simulated with the exception of excess sea-ice in the Norwegian Sea. However, the SH sea-ice extent is too small compared to observations. Both NH and SH deficiencies are linked to weak ocean overturning. The use of the Gent-McWilliams mixing scheme should be considered in future GENMOM simulations with the expectation that this scheme should cool the Southern Ocean and increase SH sea-ice (Wiebe and Weaver, 1999).

The evaluation performed here demonstrates that the first generation of GENMOM produces a realistic climatology. Deficiencies in the oceanic component of the model discussed here provide guidance for improving GENMOM. The addition of a coupled ocean model allows GENMOM to be used to investigate past climates and to study phenomena such as ENSO that require dynamic ocean-atmosphere interaction.

2.6 Acknowledgements

We thank the UK Meteorological Office Hadley Centre, US National Weather Service and PCMDI (US Dept. of Energy), and the National Oceanographic Data Center for providing access to datasets. We acknowledge the modeling groups, the Program for Climate Model Diagnosis and Intercomparison (PCMDI) and the WCRP's Working Group on Coupled Modelling (WGCM) for their roles in making available the WCRP CMIP3 multi-model dataset. Support of this dataset is provided by the Office of Science, U.S. Department of Energy. We also thank our two anonymous GMD reviewers for their feedback.

2.7 References

Anthes, R.A.: A cumulus parameterization scheme utilizing a one-dimensional cloud model. Mon. Wea. Rev. 105, 270-286, 1977.

Beckmann, B., Floegel, S., Hoffman, P., Schulz, M., and Wagner, T.: Orbital forcing of Cretaceous river discharge in tropical Africa and ocean response. Nature, 437, 241-244, 2005.

Bice, K.L., Birgel, D., Meyers, P.A., Dahl, K.A., Hinrichs, K.U., and Norris, R.D.: A multiple proxy and model study of Cretaceous upper ocean temperatures and atmospheric CO2 concentrations. Palaeoceanography, 21, PA2002, doi:10.1029/2005PA001203, 1-17, 2006.

Bryan, F.O., Danabasoglu, G., Nakashiki, N., Yoshida, Y., Kim, D.H., Tsutsui, J., and Doney, S.C.: Response of the North Atlantic thermohaline circulation and ventilation to increasing carbon dioxide in CCSM3. J Climate, 19, 2382-2397, 2006.

Bryan, K.: A numerical method for the study of the circulation of the world oceans. J. Comput. Phys., 4, 347–376, 1969.

Clapp, R.B., and Hornberger, G.M.: Empirical equations for some soil hydraulic properties. Water Res. Res., 14, 601-604, 1978.

Cogley, J.G.: GGHYDRO--Global hydrological data release 2.0, Trent Clim. Note 91-1, 13 pp., Dep. Geogr., Trent Univ., Peterborough, Ont, 1991.

Collins, W.D., Rasch, P.J., Boville, B.A., McCaa, J.R., Williamson, D.L., Kiehl, J.T., Briegleb, B., Bitz, C., Lin, S.-J., Zhang, M., and Dai, Y.: Description of the NCAR Community Atmosphere Model (CAM3.0), Technical Note TN-464+STR, National Center for Atmospheric Research, Boulder, Colo., 214 pp., 2004.

DeConto, R.M., Pollard, D. and Harwood, D.: Sea ice feedback and Cenozoic evolution of Antarctic climate and ice sheets. Paleoceanography, 22, PA3214, doi:10.1029/2006PA001350, 2006.

DeConto, R.M., Pollard, D., Wilson, P., Palike, H., Lear, C., and Pagani, M.: Thresholds for Cenozoic bipolar glaciation. Nature, 455, 653-656, 2008.

Dickinson, R.E.: Modeling evapotranspiration for three-dimensional global climate models. In: Hansen, J.E. and Takahashi, T. (eds.), Climate Processes and Climate Sensitivity. Geophysical Monograph 29, American Geophysical Union, Washington D.C., 58-72, 1984.

Dorman, J.L., and Sellers, P.J.: A global climatology of albedo, roughness and stomatal resistance for atmospheric general circulation models as represented by the Simple Biosphere Model (SB). J. Appl. Meteor., 28, 833-855, 1989.

Flato, G.M., and Hibler, W.D.: Modeling pack ice as a cavitating fluid. J. Phys. Oceanogr., 22, 626-651, 1992.

Gent, P.R., and McWilliams, J.: Isopycnal mixing in ocean circulation models. J Phys Oceanogr 20, 150-155, 1990.

GFDL GAMDT (The GFDL Global Atmospheric Model Development Team): The new GFDL global atmosphere and land model AM2- LM2: Evaluation with prescribed SST simulations. J. Clim., 17, 4641– 4673, 2004.

Gnanadesikan, A., Dixon, K.W., Griffies, S.W., et al.: GFDL's CM2 global coupled climate models–Part 2: The baseline ocean simulation, J. Climate, 19, 675–697, 2004.

Gordon, A.L., Susanto, R.D., and Ffield, A.: Throughflow within Makassar Strait. Geophys. Res., Lett., 26, 3325–3328, 1999.

Harvey, L.D.D.: Development of a sea ice model for use in zonally averaged energy balance climate models. J. Climate, 1, 1221-1238, 1988.

Held, I.M. and Phillipps, P.J.: Sensitivity of the Eddy Momentum Flux to Meridional Resolution in Atmospheric Gcms. J Climate, 6, 499-507, 1993.

Horton, D.E., Poulsen, C.J., and Pollard, D.: Orbital and CO2 forcing of late Paleozoic continental ice sheets. Geophys. Res. Lett., 34, L19708, doi:10.1029/2007GL031188, 2007.

Hostetler, S.W., Pisias, N.J., and Mix, A.C.: Sensitivity of Last Glacial Maximum climate to uncertainties in tropical and subtropical ocean temperatures. Quat. Sci. Rev., 25, 1168-1185, 2006.

Joussaume, S., Taylor, K.E., Braconnot, P., Mitchell, J.F.B., Kutzbach, J.E., Harrison, S.P., Prentice, I.C., Broccoli, A.J., Abe-Ouchi, A., Bartlein, P.J., Bonfils, C., Dong, B., Guiot, J., Herterich, K., Hewitt, C.D., Jolly, D., Kim, J.W., Kislov, A., Kitoh, A., Loutre, M.F., Masson, V., McAvaney, B., McFarlane, N., de Noblet, N., Peltier, W.R., Peterschmitt, J.Y., Pollard, D., Rind, D., Royer, J.F., Schlesinger, M.E., Syktus, J., Thompson, S., Valdes, P., Vettoretti, G., Webb, R.S., Wyputta, U.: Monsoon changes for 6000 years ago: Results of 18 simulations from the Paleoclimate Modeling Inter- comparison Project (PMIP). Geophys. Res. Lett., 26, 859–862, 1999.

Kalnay, E., Kanamitsu, M., Kistler, R., Collins, W., Deaven, D., Gandin, L., Iredell, M., Saha, S., White, G., Woollen, J., Zhu, Y., Leetmaa, A., Reynolds, B., Chelliah, M., Ebisuzaki, W., Higgins, W., Janowiak, J., Mo, K.C., Ropelewski, C., Wang, J., Jenne, R., and Joseph, D.: The NCEP/NCAR 40-Year Reanalysis Project. Bulletin of the American Meteorological Society, 77, 437-471, 1996.

NCEP-DEO AMIP-II Reanalysis (R-2): Kanamitsu, M., Ebisuzaki, W., Woollen, J., Yang, S-K, Hnilo, J.J., Fiorino, M., and Potter, G.L.: Bul. of the Atmos. Met. Soc, 1631-1643, 2002.

Kiehl, J.T., Hack, J.J., Bonan, G.B., Boville, B.A., Williamson, D.L., and Rasch, P.J.: The National Center for Atmospheric Research Community Climate Model: CCM3. J. Climate, 11, 1131-1149, 1998.

Köhl, A. and Stammer, D.: Decadal sea level changes in the 50-year GECCO ocean synthesis. J. Climate, 21, 1876–1890, 2008.

Kreitzberg, C.W., and Perkey, D.J.: Release of potential instability: Part I. A sequential plume model within a hydrostatic primitive equation model. J. Atmos. Sci., 33, 456-475, 1976.

Kump, L.R. and Pollard, D.: Amplification of Cretaceous warmth by biological cloud feedbacks. Science, 320, 195, 2008.

Lin, J. L.: The double-ITCZ problem in IPCC AR4 coupled GCMs: Ocean–atmosphere feedback analysis. J. Climate, 20, 4497–4525, 2007.

Locarnini, R. A., Mishonov, A.V., Antonov, J.I., Boyer, T.P., and Garcia, H.E.: World Ocean Atlas 2005, Volume 1: Temperature. S. Levitus, Ed. NOAA Atlas NESDIS 61, U.S. Government Printing Office, Washington, D.C., 182 pp, 2006.

Lumpkin, R. and Speer, K.: Global ocean meridional overturning. J. Phys., Oceanogr., 37, 2550-2562, 2007.

Marsland, S.J., Haak, H., Jungclaus, J.H., Latif, M., and Röske, F.: The Max-Planck-Institute global ocean/sea ice model with orthogonal curvilinear coordinates. Ocean Modelling, 5, 91–127, 2003.

Meehl, G.A., Covey, C., Delworth, T., Latif, M., McAvaney, B., Mitchell, J.F.B., Stouffer, R.J., and Taylor, K.E.: The WCRP CMIP3 multi-model dataset: A new era in climate change research, Bulletin of the American Meteorological Society, 88, 1383-1394, 2007a.

Meehl, G.A., Stocker, T.F., Collins, W.D., Friedlingstein, P., Gaye, A.T., Gregory, J.M., Kitoh, A., Knutti, R., Murphy, J.M., Noda, A., Raper, S.C.B., Watterson, I.G., Weaver, A.J., and Zhao, Z.-C.: Global Climate Projections. In: Climate Change 2007: The Physical Science Basis. Contribution of Working Group I to the Fourth Assessment Report of the Intergovernmental Panel on Climate Change [Solomon, S., D. Qin, M. Manning, Z. Chen, M. Marquis, K.B. Averyt, M. Tignor and H.L. Miller (eds.)]. Cambridge University Press, Cambridge, United Kingdom and New York, NY, USA, 2007b.

Miller, G., Mangan, J., Pollard, D., Thompson, S., Felzer B., and Magee, J.: Sensitivity of the Australian monsoon to insolation and vegetation: implications for human impact on continental moisture balance. Geology, 33, 1, 65-68, 2005.

Pacanowski, R.C.: MOM 2 Version 2.0 (Beta) Documentation: User's Guide and Reference Manual. NOAA GFDL Ocean Technical Report 3.2, 329 pp, 1996.

Peltier, W. R.: Global glacial isostatic adjustment: palaeogeodetic and space-geodetic tests of the ICE-4G (VM2) model. J. Quaternary Sci., Vol. 17 pp. 491–510. ISSN 0267-8179, 2002.

Pinot, S., Ramstein, G., Harrison, S.P., Prentice, I.C., Guiot, J., Stute, M., and Joussaume, S.: Tropical paleoclimates at the Last Glacial Maximum: Comparison of Paleoclimate Modeling Intercomparison Project (PMIP) simulations and paleodata, Clim. Dyn., 15, 857–874, 1999.

Pollard, D., Bergengren, J.C., Stillwell-Soller, L.M., Felzer, B., and Thompson, S.L.: Climate simulations for 10 000 and 6 000 years BP using the GENESIS global climate model, Paleoclimates - Data and Modelling, 2, 183-218, 1998.

Pollard, D., and Thompson, S.L.: Sea-ice dynamics and CO2 sensitivity in a global climate model. Atmos.-Ocean, 32, 449-467, 1994.

Pollard, D. and Thompson, S.L.: Use of a land-surface-transfer scheme (LSX) in a global climate model (GENESIS): The response to doubling stomatal resistance. Global and Planetary Change, 10, 129-161, 1995.

Pollard, D. and Thompson, S.L.: Climate and ice-sheet mass balance at the last glacial maximum from the GENESIS version 2 global climate model. Quaternary Science Reviews, 16, 841–864, 1997.

Poulsen, C.J., Pollard, D., and White, T.S.: General Circulation Model simulation of the d18O content of continental precipitation in the middle Cretaceous: A model-proxy comparison. Geology, 35, 199-202, 2006.

Poulsen, C.J., Pollard, D., Montanez I.P., and Rowley, D.: Late Paleozoic tropical climate response to Gondwanan glaciation, Geology, 35, 771-774, 2007.

Randall, D.A., Wood, R.A., Bony, S., Colman, R., Fichefet, T., Fyfe, J., Kattsov, V., Pitman, A., Shukla, J., Srinivasan, J., Stouffer, R.J., Sumi, A., and Taylor, K.E.: Climate Models and Their Evaluation. In: Climate Change 2007: The Physical Science Basis. Contribution of Working Group I to the Fourth Assessment Report of the Intergovernmental Panel on Climate Change [Solomon, S., D. Qin, M. Manning, Z. Chen, M. Marquis, K.B. Averyt, M.Tignor and H.L. Miller (eds.)]. Cambridge University Press, Cambridge, United Kingdom and New York, NY, USA, 2007.

Reynolds, R.W., Rayner, N.A., Smith, T.M., Stokes, D.C., and Wang, W.: An Improved In Situ and Satellite SST Analysis for Climate. J. Climate, 15, 1609-1625, 2002.

Roeckner, E., Bäuml, G., Bonaventura, L., et al.: The Atmospheric General Circulation Model ECHAM5. Part I: Model Description, MPI Report 349, Max Planck Institute for Meteorology, Hamburg, Germany, 127 pp., 2003.

Ruddiman, W.F., Vavrus, S.J., and Kutzbach, J.E.: A test of the overdue-glaciation hypothesis. Quat. Sci. Rev., 24, 1-10, 2005.

Schmittner, A., Latif, M., and Schneider, B.: Model projections of the North Atlantic thermohaline circulation for the 21st century assessed by observations. Geophys. Res. Lett., 32, L23710, doi:10.1029/2005GL024368, 2005.

Schmittner, A., Silva, T.A.M., Fraedrich, K., Kirk, E., Lunkeit, F.: Effects of Mountains on Global Ocean Circulation. Journal of Climate, *in press*, doi:10.1175/2010JCLI3982.1.

Semtner, A.J.: A model for the thermodynamic growth of sea ice in numerical investigations of climate. J. Phys. Oceanogr., 6, 379-389, 1976.

Senior, C.A. and Mitchell, J.F.B.: Carbon dioxide and climate: the impact of cloud parameterization. J. Climate, 6, 393-418, 1993.

Sijp, W. P. and England, M.H.: Southern Hemisphere Westerly Wind Control over the Ocean's Thermohaline Circulation. J. Clim., 22, 1277-1286, 2009.

Smith, R.N.B.: A scheme for predicting layer clouds and their water content in a general circulation model. Q. J. Roy. Meteorol. Soc., 116, 435-460, 1990.

Smith, R.D., and Gent, P.R.: Reference Manual for the Parallel Ocean Program (POP), Ocean Component of the Community Climate System Model (CCSM2.0 and 3.0). Technical Report LA-UR-02-2484, Los Alamos National Laboratory, Los Alamos, NM, http://www.ccsm. ucar.edu/models/ccsm3.0/pop/, 2002.

Thompson, S.L. and Pollard, D.: A global climate model (GENESIS) with a land-surface-transfer scheme (LSX). Part 1: Present-day climate. J. Climate, 8, 732-761, 1995.

Thompson, S.L. and Pollard, D.: Greenland and Antarctic mass balances for present and doubled CO2 from the GENESIS version 2 global climate model. J. Climate, 10, 871-900, 1997.

Tibaldi, S., Palmer, T.N. Brankovic, C., and Cubasch, U.: Extended-Range Predictions with ECMWF Models: Influence of Horizontal Resolution on Systematic-Error and Forecast Skill. Q J Roy Meteor Soc, 116, 835-866, 1990.

Toggweiler, J. R. and Samuels, B.: Effect of Drake Passage on the Global Thermohaline Circulation. Deep Sea Res. I, 42, 477-500, 1995.

UK Meteorological Office, Hadley Centre: HadISST 1.1 - Global sea-Ice coverage and SST (1870-Present), [Internet]. British Atmospheric Data Centre, Downloaded 2/8/2010. Available from http://badc.nerc.ac.uk/data/hadisst/, 2006.

Webb, R.S., Rosenzweig, C.E., and Levine, E.R.: Specifying land surface characteristics in general circulation models: Soil profile data set and derived water-holding capacities. Global Bio- geochem. Cycles, 7, 97–108, 1993.

Wiebe, E.C., and A. J. Weaver, 1999: On the sensitivity of global warming experiments to the parameterization of sub-grid scale ocean mixing. Climate Dyn., 15, 875–893.

Williamson, D.L. and Rasch, P.J.: Two-dimensional semi-Lagrangian transport with shape-preserving interpolation. Mon. Wea. Rev., 117, 102-129, 1989.

Williamson, D.L., Kiehl, J.T., Ramanathan, V., Dickinson, R.E., and Hack, J.J.: Description of NCAR Community Climate Model (CCM1). NCAR Technical Note NCAR/TN-285+STR, Boulder, Colorado, 112 pp, 1987.

Zhou, J., Poulsen, C.J., Pollard, D., and White, T.S.: Simulation of modern and middle Cretaceous marine d18O with an ocean-atmosphere general circulation model. Paleoceanography, 23, PA3223, doi:10.1029/2008PA001596, 2008.

Chapter 3: The sensitivity of ENSO to increased atmospheric CO_2 as simulated by the atmosphere-ocean model GENMOM

J. R. Alder[1], S. W. Hostetler[2] and D. Pollard[3]

[1]Oregon State University, Department of Geosciences, Corvallis, OR 97331, United States

[2]US Geological Survey, Oregon State University, Department of Geosciences, Corvallis, OR 97331, United States

[3]Pennsylvania State University, EMS Earth and Environmental Systems, University Park, PA 16802, United States

3.1 Abstract

The El Niño/Southern Oscillation (ENSO) affects societies in many countries through global atmospheric teleconnections that bring drought or torrential rainfall. How ENSO might respond to global warming is unclear. Here we apply a new AOGCM, GENMOM, which combines the GENESIS atmospheric GCM (Global ENvironmental and Ecological Simulation of Interactive Systems) and MOM (Modular Ocean Model), to test the response of ENSO to global warming. GENMOM simulates a realistic present-day climate (Alder et al, 2011) and we demonstrate that GENMOM captures ENSO dynamics to a degree similar to other AOGCMs that were evaluated in the IPCC AR4. We evaluate the simulated response of ENSO to doubling (710 ppmV) and quadrupling atmospheric CO_2 (1420 ppmV) (hereafter denoted 1x, 2x and 4x respectively) using 700-year equilibrium simulations. Where possible, we compare our results to eight AOGCMs used in the IPCC AR4. Our GENMOM sensitivity tests indicate higher amplitude and more frequent ENSO events are associated with global warming. Bjerknes feedbacks weaken with increased atmospheric CO_2, where the east-west Pacific temperature gradient is reduced by ~34% in the 4x simulation, which in turn drives a 38% reduction in west Pacific windstress and ~32% reduction in east Pacific upwelling, allowing larger and more frequent anomalies to develop. The Walker Circulation weakens, while the west Pacific zone of deep tropical convection is displaced eastward, resulting in a more eastwardly confined El Niño warm tongue. Analysis of atmospheric teleconnections reveals the present day positive (negative) western North American temperature anomalies associated with El Niño (La Niña) experience a sign reversal under the 4x simulation to become negative (positive). South American temperature and precipitation

teleconnections are simulated to strengthen with increasing atmospheric CO_2, as are precipitation teleconnections to the Indian subcontinent.

3.2 Introduction

ENSO is a coupled ocean-atmosphere mode of variability that occurs in the Pacific Ocean (Neelin et al., 1998) with regional to global influence. The phases of ENSO are identified by warm (El Niño) or cold (La Niña) sea surface temperature (SST) anomalies along the equator and anomalies of the sea level pressure (SLP) difference between Tahiti and Darwin, Australia (Horel and Wallace, 1981). During non-ENSO periods, the tropical Pacific is in a quasi-stable balance between SSTs and windstress related to trade wind convergence in the Intertropical Convergence Zone (ITCZ). Warm westerly waters give rise to buoyant air masses that drive deep tropical convection over Indonesia. Once lifted to the upper atmosphere, these air masses diverge and are propagated eastward by upper atmospheric westerly winds. Cool eastern Pacific surface temperatures cause divergence at the surface, which, in turn, induces the upper atmospheric air mass to subside. At the surface, easterly winds complete the loop by forcing the surface air mass westward to the region of deep tropical convection. This convective loop is known as the Walker Circulation and the location of convection strongly influences the location and intensity of rainfall over Southeast Asia and South America. Windstress caused by strong easterly winds force an oceanic response in the form of eastern coastal upwelling. The cool upwelled water brought to the surface helps maintain an east-west SST gradient. The balance of winds, water temperature and upwelling are collectively known as Bjerknes feedbacks (Bjerknes, 1969).

ENSO events are a disruption of the Walker Circulation where the Bjerknes feedbacks are either weakened (El Niño) or strengthened (La Niña). El Niño events occur when the easterly trade winds relax, allowing the warm western waters to propagate eastward, thereby weakening the east-west temperature gradient. Because the convective branch of the Walker Circulation is centered on the region of warmest water, the eastward expansion of warm water forces an eastward shift of the convective branch. The reduced windstress associated with the relaxed easterly winds weakens upwelling, which helps to reduce further the east-west temperature gradient. La Niña events are generally the opposite of El Niño: the easterly trade winds strengthen which enhances upwelling along the coast of South America bringing more cool water to the surface thereby strengthening the east-west surface temperature gradient (Neelin et al., 1998). The increased easterly wind strength forces warm westerly surface waters west with the accompanying westward shift of rainfall.

Neither the ocean nor the atmosphere trigger an ENSO event in isolation, they are inherently linked (Trenberth, 1997; Neelin et al., 1998). Historical observations indicate the frequency of ENSO is between 3 - 7 years. Significant progress has been made over the past two decades in understanding the underlying mechanisms of ENSO and related hydrological teleconnections (Giannini et al., 2001; Ropelewski and Halpert, 1987). The long-term behavior of ENSO outside the historical record and under radiative forcing associated with varying atmospheric composition and large-scale boundary conditions (e.g., continental ice sheets) that occurred in the past (Clement et al., 1999), and that might occur in the future (Collins, 2000a; Collins, 2000b), is of interest for extending our understanding of ENSO to interpret the past and inform us about future climatic change and variability. Modeling past and future ENSO characteristics is best accomplished through the application of coupled atmospheric and oceanic general circulation models and many related model studies have been published (eg, Otto-Bliesner et al., 2003; Liu et al, 2000; Timmermann et al., 1999; Merryfield, 2006).

Here we explore the multi-century ENSO response to present (355 ppmV), doubled (710 ppmV) and quadrupled (1420 ppmV) atmospheric CO_2 levels (1x, 2x and 4x respectively) using a new non-flux corrected AOGCM, GENMOM, that combines GENESIS version 3 (Global ENvironmental and Ecological Simulation of Interactive Systems) and MOM version 2 (Modular Ocean Model) general circulation models (Alder et al, 2011). Our current version of GENMOM uses T31 (~3.75° x 3.75° latitude and longitude) horizontal resolution for both the atmosphere and ocean to balance computational requirements with the ability to simulate features of the general circulation. We first compare the GENMOM simulation of present-day climatology of the Pacific Basin with observations and with eight AOGCMs used in the Intergovernmental Panel on Climate Change Fourth Assessment Report (IPCC AR4, Randall, 2007). We then investigate the GENMOM ENSO response to atmospheric CO_2 forcing using 700-year equilibrium simulations. The first 400 years are discarded as model spin-up, leaving 300 years for our analysis. In addition to the 1x, 2x, 4x equilibrium simulations we include a shorter 140-year transient simulation using the A2 emission scenario (Nakićenović, 2000) to test the ENSO response to non-stationary atmospheric CO_2 forcing.

3.3 GENMOM description

GENMOM is a hybrid name that combines the atmospheric model GENESIS version 3 (Thompson and Pollard, 1995; Thompson and Pollard, 1997; Pollard and Thompson, 1997) with the ocean model MOM version 2 (Pacanowski, 1996). The main improvements in GENESIS version 3 are (1) solar and thermal infrared radiation are calculated using the NCAR CCM3 radiation code, and (2) the ocean is optionally represented by the MOM2 ocean general circulation model to compose GENMOM. The nominal AGCM resolution is spectral T31 (3.75° x 3.75°) with 18 vertical levels using sigma coordinates. MOM2 uses 20 unevenly spaced levels. A land-surface transfer model (Land Surface eXchange) accounts for the physical effects of vegetation (Pollard and Thompson, 1995). To simplify the coupling between the atmosphere and ocean, both the GCMs are implemented on essentially the same T31 grid. In MOM2, the latitudinal grid spacing is not exactly T31, but is adjusted with a cosine-stretching factor (Pacanowski, 1996) to closely approximate T31. GENESIS has a 30-min timestep, and MOM2 has a 6 h timestep for scalar fields. The two models interact in an essentially synchronous manner, communicating every 6 h. 6 h averages of the surface fluxes of heat, water and momentum are passed from GENESIS to MOM2, and MOM2 is run through one 6 h scalar timestep. The updated SSTs are passed back to GENESIS and used to run it for the next 6 h. A detailed description of GENMOM is presented by Alder et al (2011).

Formal evaluation of the present day climatology simulated by GENMOM (Alder et al, 2011) indicates that the model captures global circulation patterns. Atmospheric fields such as the jet stream structure and major SLP features are well simulated. The simulated global 2 m air temperature is 0.6 ºC warmer over oceans and 1.3 ºC colder over land. The model has a warm SST bias (1 – 2.5 ºC) in the Southern Ocean and a subsurface warm temperature bias (exceeding 2 ºC) between 200–1000 m in the tropics and mid-latitudes. Similar to other AOGCMs, GENMOM simulates a weaker-than-observed Atlantic Meridional Overturning Circulation (AMOC): the maximum simulated overturning is 14.5 ± 0.9 Sv, whereas the observed range is 16 - 18 Sv. Also similar to other AOGCMs, GENMOM produces a split ITCZ. Alder et al (2011) compare the GENMOM simulated climatology to three IPCC AR4 models (GFDL CM 2.0, MPI ECHAM5, and NCAR CCSM 3.0 used in this evaluation) finding that the climatologies are generally comparable despite the coarse T31 resolution.

3.4 Simulation of ENSO

Numerous intermodel comparison projects (AchutaRao and Sperber, 2002; AchutaRao and Sperber, 2006; Guilyardi, 2006) indicate that the ability of coupled AOGCMs to simulate ENSO is improving, but that there are many areas for further improvements. In most cases the models do not accurately capture the ocean-atmosphere dynamics of ENSO that are identified in the observed record, such as the tight link between ocean and atmosphere in transferring anomalies between the two or the seasonal timing of ENSO events. AchutaRao and Sperber (2002, hereafter referred to as AS02) compared simulations from the 17 models that were used in the Coupled Model Intercomparison Project (CMIP2). AchutaRao and Sperber (2006, hereafter referred to as AS06) published a follow-up study to assess whether the models used in IPCC AR4 performed better than the prior generation of CMIP2 models evaluated in AS02. We rely on the techniques used in AS02 and AS06 to evaluate the ENSO in GENMOM.

3.4.1 Validation datasets

In our evaluation we use NOAA NCEP Reanalysis 1 data (NCEP1, Kalnay et al., 1996), which spans 1948 – 2007 thereby providing a relatively long "observed" record of atmospheric fields associated with ENSO. Because NCEP1 fields are produced by a global reanalysis model, we also use the Hadley Ice and Sea Surface Temperature v1.1 (HadISST, UK Meteorological Office, 2006) dataset to provide observed SSTs for same time period as the NCEP. Observed sea surface temperature is not available from NCEP1, so 2 m air temperature is used as a proxy. Although these fields are different, they have similar values over tropical waters on a monthly basis, particularly in the equatorial Pacific. In the case of GENMOM, switching from SST to 2 m air temperature do not change our results. To evaluate upwelling, we use the German partner of the Estimating the Circulation and Climate of the Ocean dataset (GECCO, Köhl and Stammer, 2008).

The three simulations are integrated for 700 years. The first 400 years are disregarded as model spin-up, leaving 300 years to be used in our analysis. Over the last century of the simulation, the deep ocean (>1,000 m) warmed by ~0.002 °C/decade, the mid layers (200 m - 1,000 m) warmed by ~0.003 °C/decade and the surface temperature was essentially free of drift. We compare a subset period of 60 years (model years 400-459) from the 700-year GENMOM simulation to the observed records. A 60-year subset period was used so length of the simulated data is comparable to that of the observed records (1948 – 2007). The 60-year period was chosen by subdividing the 300-year record into 10, non-overlapping intervals, calculating the standard deviation of the Niño 3 index for each period and selecting the 60-year period that had a Niño 3 index standard deviation closest to that of HadISST (see section 3c. for Niño index definition). Eight IPCC AR4 models are included in our analysis for context (Table 3.1). The time period analyzed for each of these comparison models is the last 60 years of the Climate of the 20th Century experiment (1970 – 1999).

3.4.2 Simulated tropical Pacific

The background mean state of SST in the tropical Pacific plays an important role in the mechanics of ENSO; yet, although many AOGCMs simulate the large scale gradients well, they often fail to simulate the finer spatial patterns such as the east-west temperature gradient or the seasonal timing of winds. The western Pacific is characterized by the Warm Pool (WP) with surface temperatures exceeding 28 ºC, whereas the eastern Pacific has much cooler surface temperatures (20 – 25 ºC). These lower temperatures are the result of cold-water upwelling and surface advection of cool higher latitude water via the Peru Current. The difference in east-west surface temperature sets up a gradient that drives surface winds, which reinforce the warm-cold gradient by enhancing upwelling. GENMOM simulates the east-west temperature gradient, but it is weaker than observed (Figs. 3.1 and 3.2). During both December, January, February (DJF) and June, July, August (JJA), GENMOM is too warm in the eastern Pacific, specifically at 15º S. The weak Peru Current discussed by Alder et al. (2011) is expressed by insufficient northward transport of cold water in the far eastern Pacific with an attendant strong zonal SST pattern. The eastern Pacific is generally too warm, and the western Pacific is not warm enough, which is also seen in GDFL CM 2.0 and NCAR CCSM 3.0. During DJF when peak insolation is south of the equator, GENMOM simulates far too much zonal warming in the eastern Pacific, which is similar

Table 3.1 Eight AOGCMs used in the IPCC AR4. T indicates the horizontal resolution using spectral truncation. L indicates the number of levels used in the model.

Model	Modeling Center, Country	Atmosphere Resolution	Ocean Resolution
CCCMA CGCM 3.1 T63	Canadian Centre for Climate Modelling and Analysis, Canada	T47 (~2.8° x 2.8°) L31 McFarlane et al., 1992; Flato, 2005	1.9° x 1.9° L29 Pacanowski et al., 1993
CSIRO MK 3.0	Commonwealth Scientific and Industrial Research Organisation (CSIRO) Atmospheric Research, Australia	T63 (~1.9° x 1.9°) L18 Gordon et al., 2002	0.8° x 1.9° L31 Gordon et al., 2002
GFDL CM 2.0	U.S. Department of Commerce/National Oceanic and Atmospheric Administration (NOAA)/Geophysical Fluid Dynamics Laboratory (GFDL), USA	2.0° x 2.5° L24 GFDL GAMDT, 2004	0.3°–1.0° x 1.0° Gnanadesikan et al., 2004
MIROC 3.2 medres	Center for Climate System Research (University of Tokyo), National Institute for Environmental Studies, and Frontier Research Center for Global Change (JAMSTEC), Japan	T42 (~2.8° x 2.8°) L20 K-1 Developers, 2004	0.5°–1.4° x 1.4° L43 K-1 Developers, 2004
MIUB ECHO-G	Meteorological Institute of the University of Bonn, Meteorological Research Institute of the Korea Meteorological Administration (KMA), and Model and Data Group, Germany/Korea	T30 (~3.9° x 3.9°) L19 Roeckner et al., 1996	0.5°–2.8° x 2.8° L20 Wolff et al., 1997
MPI ECHAM5	Max Planck Institute for Meteorology, Germany	T63 (~1.9° x 1.9°) L31 Roeckner et al., 2003	1.5° x 1.5° L40 Marsland et al., 2003
NCAR CCSM 3.0	National Center for Atmospheric Research, USA	T85 (1.4° x 1.4°) L26 Collins et al., 2004	0.3°–1° x 1° L40 Smith and Gent, 2002
UKMO HadCM3	Hadley Centre for Climate Prediction and Research/Met Office, UK	~1.3° x 1.9° L38 Pope et al., 2000	0.3°–1.0° x 1.0° L40 Gordon et al., 2000

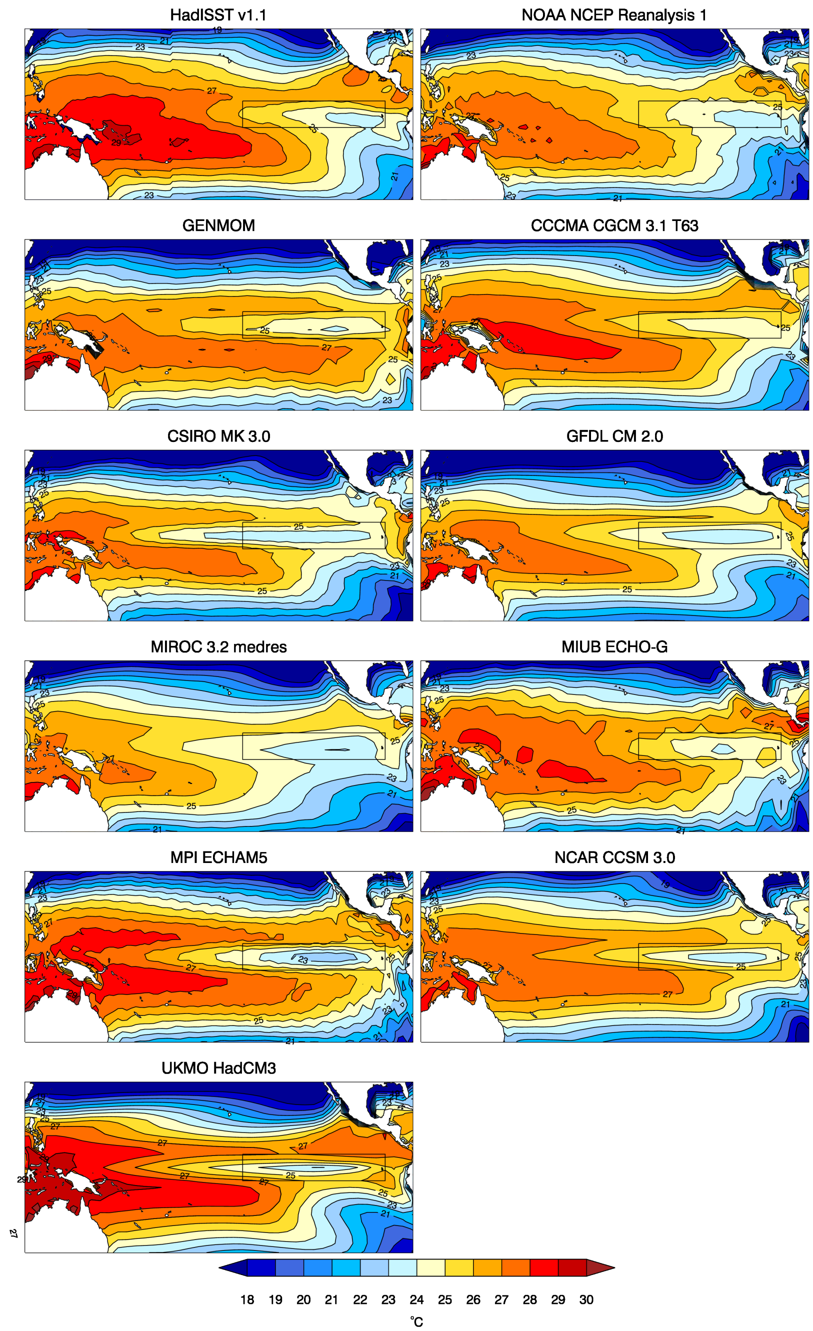

Figure 3.1 December, January, Febuary (DJF) average surface temperature over the Pacific basin for HadISST v1.1 and NCEP1, GENMOM and eight IPCC AR4 models. HadISST v1.1 is shown as SST, all others are 2 m air temperature. The Niño 3 region is overlaid in black.

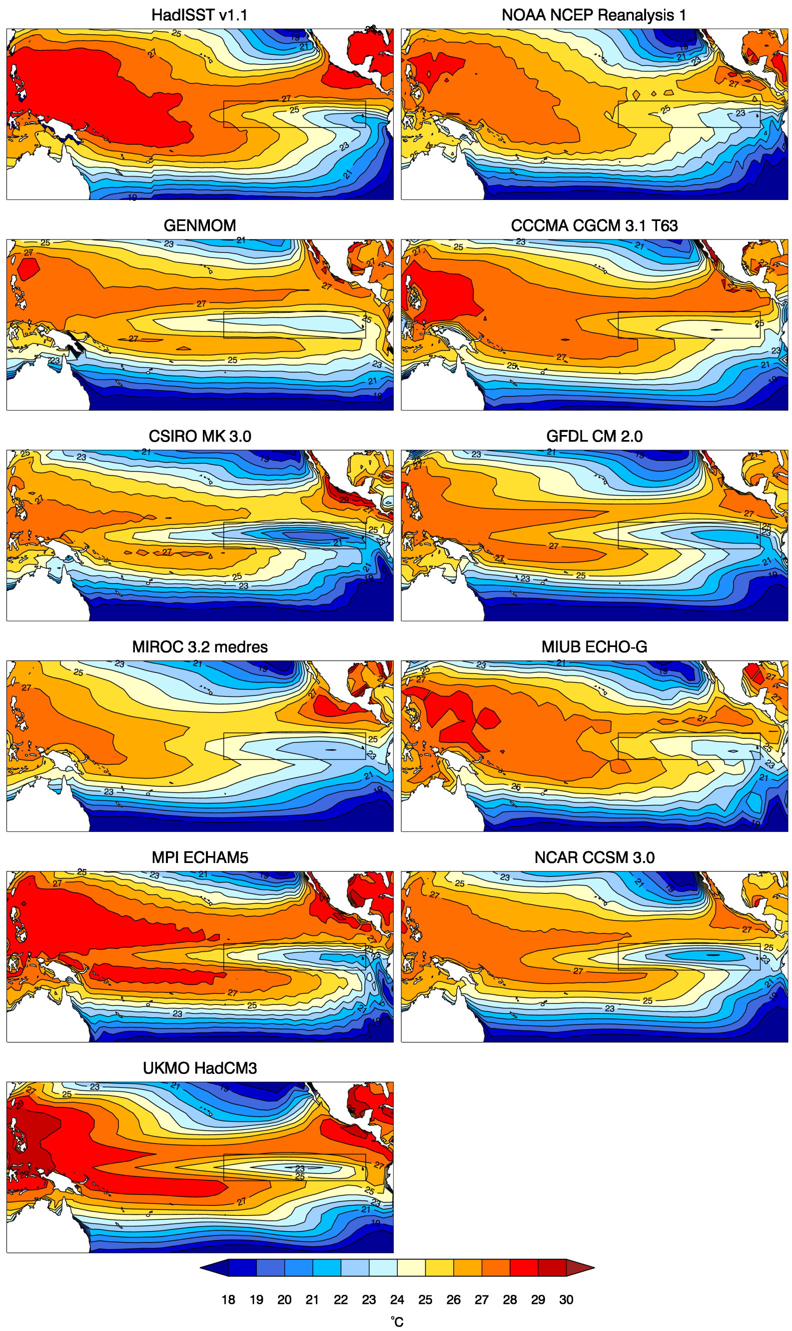

Figure 3.2 June, July, August (JJA) average surface temperature over the Pacific basin for HadISST v1.1 and NCEP1, GENMOM and eight IPCC AR4 models. HadISST v1.1 is shown as SST, all others are 2 m air temperature. The Niño 3 region is overlaid in black.

to MPI ECHAM5 and NCAR CCSM 3.0. During JJA when peak insolation is north of the equator, GENMOM simulates cool water that is confined to the equator and extends farther to the west than observed (Fig. 3.2). A few of the IPCC models shown here (CSIRO MK3, GDFL CM 2.0 and NCAR CCSM 3.0) also have a summer cold tongue that extends too far west, but only GENMOM has cool SSTs enclosed by warm SSTs. This could be caused by the weak northward Peru Current failing to bring cool water northward or weak subsurface upwelling. GENMOM simulates a distinct semi-annual cycle in the eastern equatorial Pacific where waters cool during northern hemisphere spring whereas observations indicate the region should remain warm during that part of the year (not shown). Although the simulation of a semi-annual temperature cycle is incorrect, it is not uncommon in AOGCMs (Guilyardi, 2006). AS02 found both NCAR CSM and DOE-PCM models had a semi-annual cycle, however an eastern Pacific semi-annual cycle is not seen in any of the IPCC AR4 models presented here.

Similar to the GECCO reanalysis, GENMOM produces a seasonal cycle of upwelling off the western coast of South America with fall and spring maxima (Fig. 3.3). The net annual total of upwelled waters at ~100 m water depth is 4.6 Sv and 8.3 Sv in GENMOM and the GECCO data set, respectively, indicating GENMOM is capturing the correct seasonal timing of upwelling but annually has too little net upwelling.

The ascending and decending branches of the Walker Cirulation, as quantified by omega, are generally well simulated in GENMOM (Fig. 3.4). The wintertime (DJF) convective zone is correctly positioned at 150º E, but is narrower than observed. The wintertime (DJF) subsidance zone is also well positioned in the east Pacific, but is weaker-than-observed and more confined to the east than observed. This is likely due to

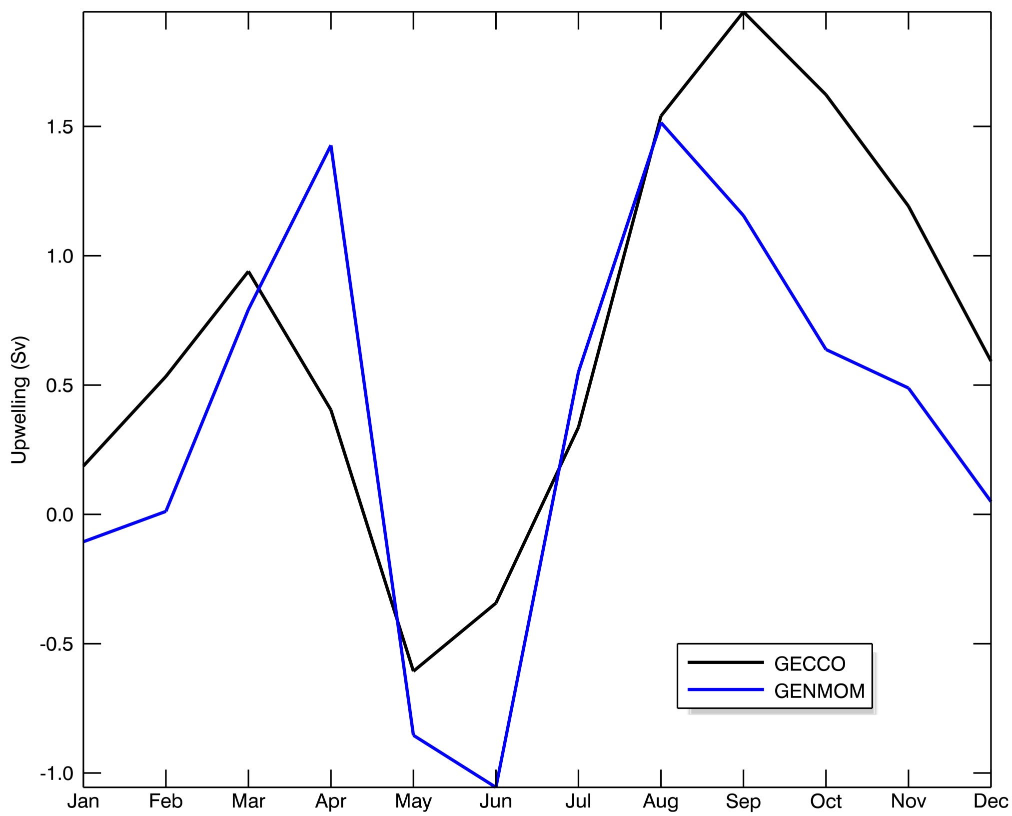

Figure 3.3 Upwelling volume off the South American western coast (110º W - 90º W, 10º S - 30º S) at ~100 m depth.

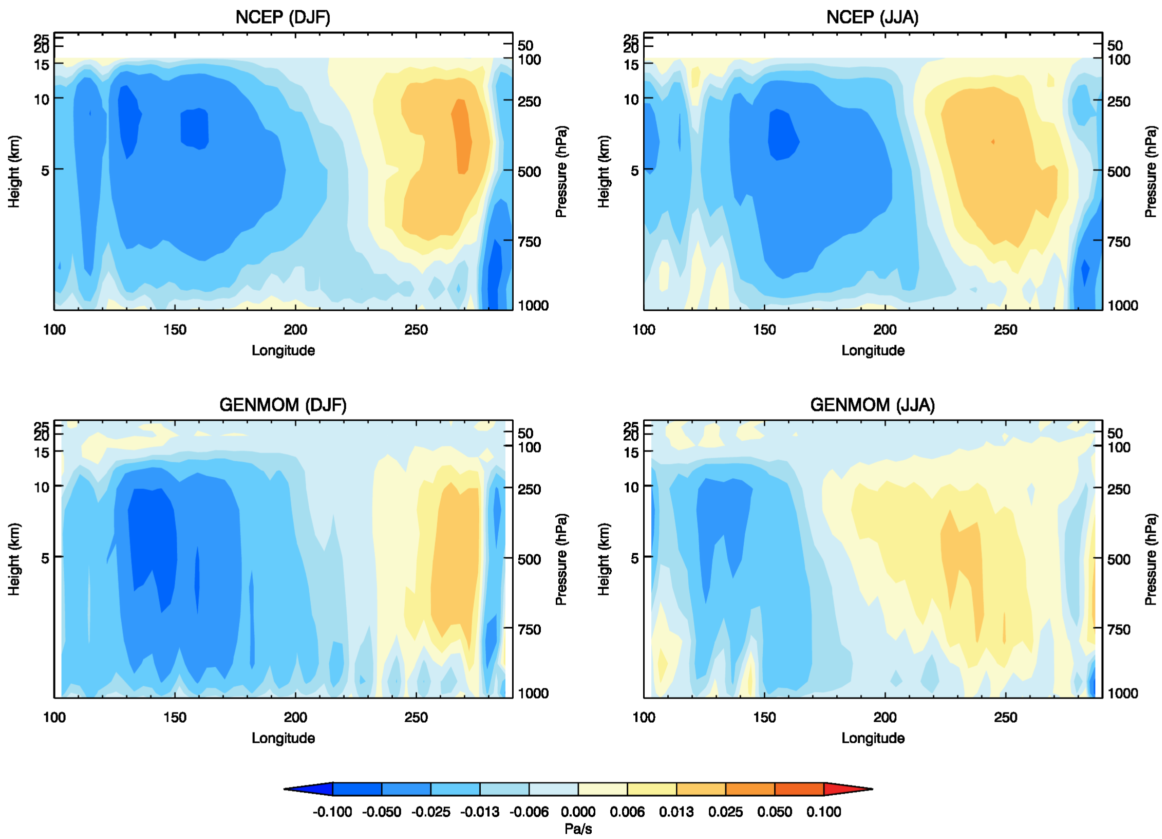

Figure 3.4 Winter and summer Walker Circulation composites of Omega comparing both NCEP1 and GENMOM. Negative values indicate vertical convection whereas positive values represent subsidence.

GENMOM east Pacific SSTs not being cool enough. The summertime (JJA) west Pacific convective region is both weaker and displaced westward relative to NCEP because GENMOM exhibits a ~2 °C bias in the Warm Pool and because the warmest SSTs don't extend far enough towards the central Pacific. The summertime subsidence zone is also weaker-than-observed and extends too far west because the GENMOM cold tongue is too warm and extends too far west. In the eastern Pacific, the coldest SSTs should be nearly meridional, whereas in GENMOM they are zonal (Fig. 3.2), which weakens the strength of eastern subsidence.

3.4.3 ENSO regions of variability

To simplify the analysis of ENSO, we subdivide the Pacific into three regions and average SSTs for each model grid point within the region into a single value. The three established regions in the tropical Pacific are Niño 3 (5°N – 5°S, 150°W – 90°W), Niño 3.4 (5°N – 5°S, 170°W – 120°W) and Niño 4 (5°N – 5°S, 160°E – 150°W), which are used to measure variability in the west Pacific (Niño 4), central Pacific (Niño 3.4), and east Pacific (Niño 3, Rasmusson and Carpenter, 1982). Warm El Niño temperature anomalies typically initiate in the eastern Niño 3 region and quickly spread across the equatorial Pacific to the Niño 4 region. Sea surface temperatures or 2 m air temperature for these regions are spatially averaged and then the mean is removed to separate the influence of the seasonal cycle, so that only temperature departures from normal remain. These anomaly indices are commonly used as a metric of ENSO variability. The use of the Niño indices allows climate models to be compared to observations in general way. The indices also provide a way to gauge the strength of a particular ENSO event to other past events.

The standard deviations of monthly 2-m air temperature anomalies in the three Niño regions for the observed data, GENMOM, and the IPCC AR4 models evaluated in AS06 are shown in Fig. 3.5 (NCEP1 is shown as 2 m air temperature, HadISST as SST). The overall magnitude of temperature variability simulated by GENMOM is within 0.3 degrees or less of observations in all regions. Similar to other non flux-corrected AOGCMs, GENMOM incorrectly produces peak variability in the Niño 4 region with decreasing eastward variability rather than the west-to-east increase in variability displayed in the observations. Failure to produce peak variability in the observed Niño 3 region may be an indicator that the simulated ENSO events are not properly interacting with the seasonal cycle, or in the case of GENMOM, the eastern Pacific seasonal cycle is not properly being simulated (AchutaRao and Sperber, 2002).

3.4.4 ENSO time series

Here we calculate Niño indices as monthly deviations of SSTs from the climatological monthly mean. Many definitions as to what constitutes an ENSO event are used in the literature (Quinn et al., 1978; SCOR, 1983; Wolter and Timlin, 1993); we follow Trenbeth (1997) who defines an El Niño (La Niña) event as a period when the temperature anomaly of the Niño 3 region remains above (below) 0.5°C (-0.5°C) for six consecutive months in a five month smoothed time series. The five-month smooth is used to minimize any possible influence from intraseasonal variations in the tropical ocean (Trenbeth, 1997). The Niño 3 time series produced by GENMOM (model years 400-459) displays greater variability and lower amplitude ENSO events than those of the two observed datasets (Fig. 3.6), indicating the model is producing more sub-ENSO (< 2 - 3 years) variability than is exhibited in the observations. The lower event amplitude is

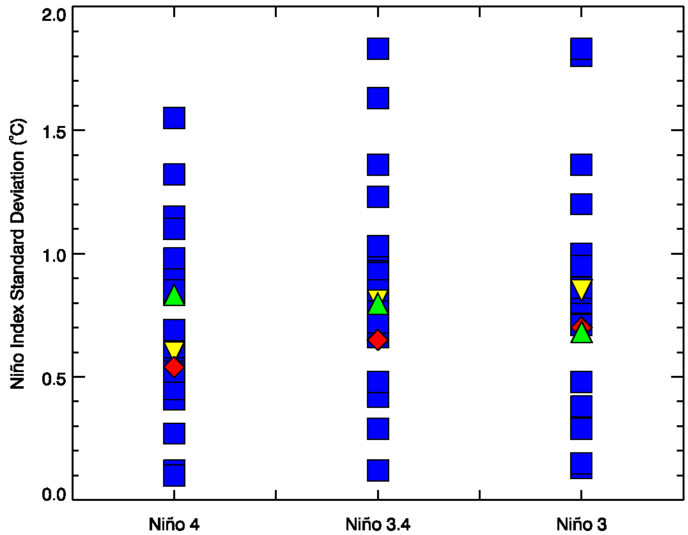

Figure 3.5 Standard deviations of monthly anomalies for observed, IPCC AR4 models evaluated in AS06 (surface air temperature) and GENMOM (SST) for the Niño regions. GENMOM (green), HadISST v1.1 (yellow), and NCEP1 (red). IPCC model results are provided in Table 2 of AchutaRao and Sperber (2006).

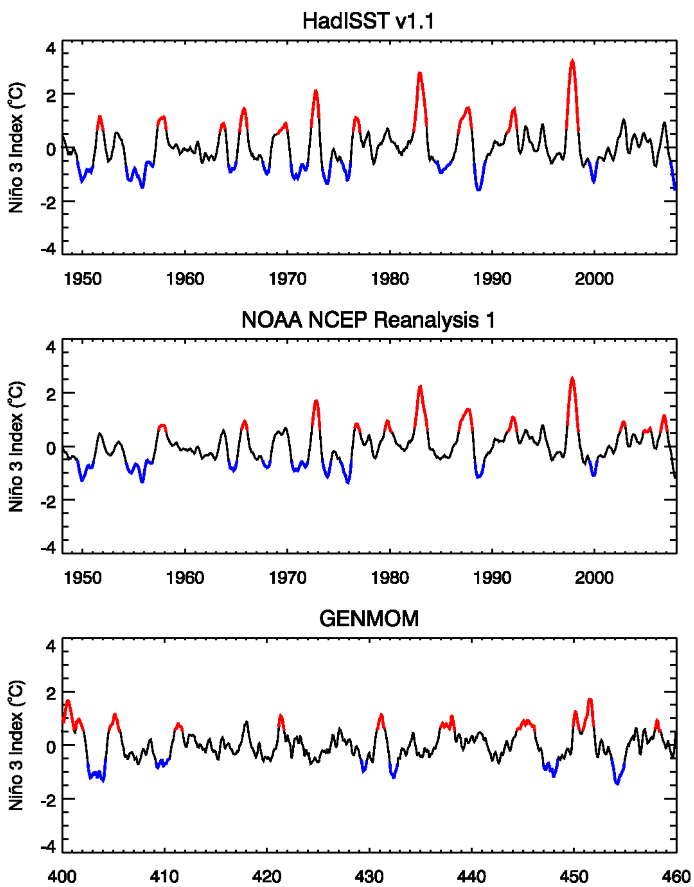

Figure 3.6 Observed and simulated Niño 3 indices.

consistent with the standard deviation values (Fig. 3.5). The observed Niño 3 index is skewed towards stronger El Niño events, while GENMOM produces a more symmetrical time series with El Niño and La Niña events essentially having the same strength.

Spectral analysis is a commonly used technique to determine the frequency of ENSO events. Here we use the Maximum Entropy Method (MEM) so that our results are comparable to AS02 and AS06. The spectra of the simulated Niño 3 index computed by MEM places a single peak at 5.3 years in contrast to the NCEP1 and HadISST v1.1 that display peak power at 3.9 and 4.3 years respectively (Fig. 3.7). Although the ENSO produced by GENMOM is less frequent than observations, the broad spectral peak is similar to that of the observations, indicating that ENSO events occur at intervals between 4 and 8 years. The narrow peaks in the power spectra presented in Fig. 2a of AS06 indicate that many of the IPCC AR4 models produce ENSO events that are both too frequent and too regular (not shown). Significant spectral power in the 2 - 7 year range is absent in many of the IPCC AR4 models. A few of the IPCC AR4 models do not produce variability in the Niño 3 region with the magnitude of the anomalies greater than ± 0.5°C for six consecutive months, thereby failing to meet our criterion for an ENSO event. Thus we find that GENMOM is producing ENSO events with a reasonable frequency, while that frequency is lower than the observation it is well within the range seen in the IPCC AR4 models (AchutaRao and Sperber, 2006).

3.4.5 Composite anomalies of surface fields during ENSO events

Composite anomalies of temperature and precipitation for modeled ENSO events illustrate global teleconnections and provide a means for comparing GENMOM with observations and other AOGCMs. ENSO composites are computed by globally

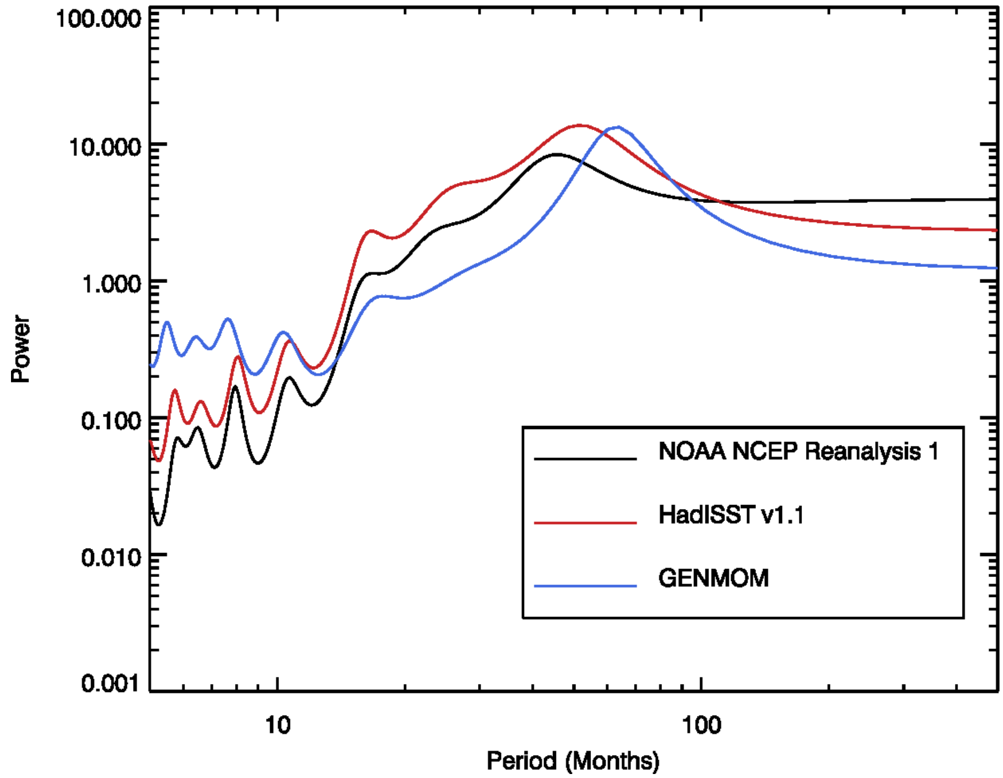

Figure 3.7 Observed and simulated Niño 3 index MEM spectra. The SSA Toolkit (Dettinger et al., 1995) was used to calculate power spectra via the Maximum Entropy Method.

averaging all periods (e.g., DJF) wherein ENSO events occur and subtracting the long-term mean from the event average. The goal of this technique is to produce snapshots of how global temperature and precipitation patterns differ during ENSO events. The GENMOM temperature teleconnections during warm El Niño events are generally well simulated (Fig. 3.8) compared to NCEP. The simulated warm tongue in the equatorial Pacific is somewhat compressed latitudinaly relative to NCEP, but has the correct east-west extent. The classic horseshoe-shaped pattern of cold anomalies surrounding the warm tongue is well simulated in GENMOM. Similar to most of the other models shown here, the strengthening of the Aleutian Low, indicated by cold SST anomalies, is weaker-than-observed in GENMOM. Although GENMOM simulates cold anomalies in northern Canada and Alaska, it does capture the warm anomaly to the United States better than most of the IPCC AR4 models shown here that predominantly incorrectly simulate a cold teleconnection. Most of the models shown here correctly have a warm temperature teleconnection to northern South America and a cold anomaly over southern South America. GENMOM also exhibits this pattern, but the southern cold anomaly is stronger than in NCEP, a common problem with the other models. El Niño teleconnections to Asia are varied in both the observations and model simulations, yet only GENMOM and CCCMA CGCM 3.1 place a strong positive anomaly over northern Asia. GENMOM, as well as all the IPCC AR4 models shown here, correctly simulates the warm teleconnection to Australia as seen in NCEP.

The temperature teleconnections of cold La Niña events simulated by GENMOM have similar but, in many cases opposite, characteristics to the warm events (Fig. 3.9). The subtropical high in the Pacific is strengthened during La Niña events, which is seen

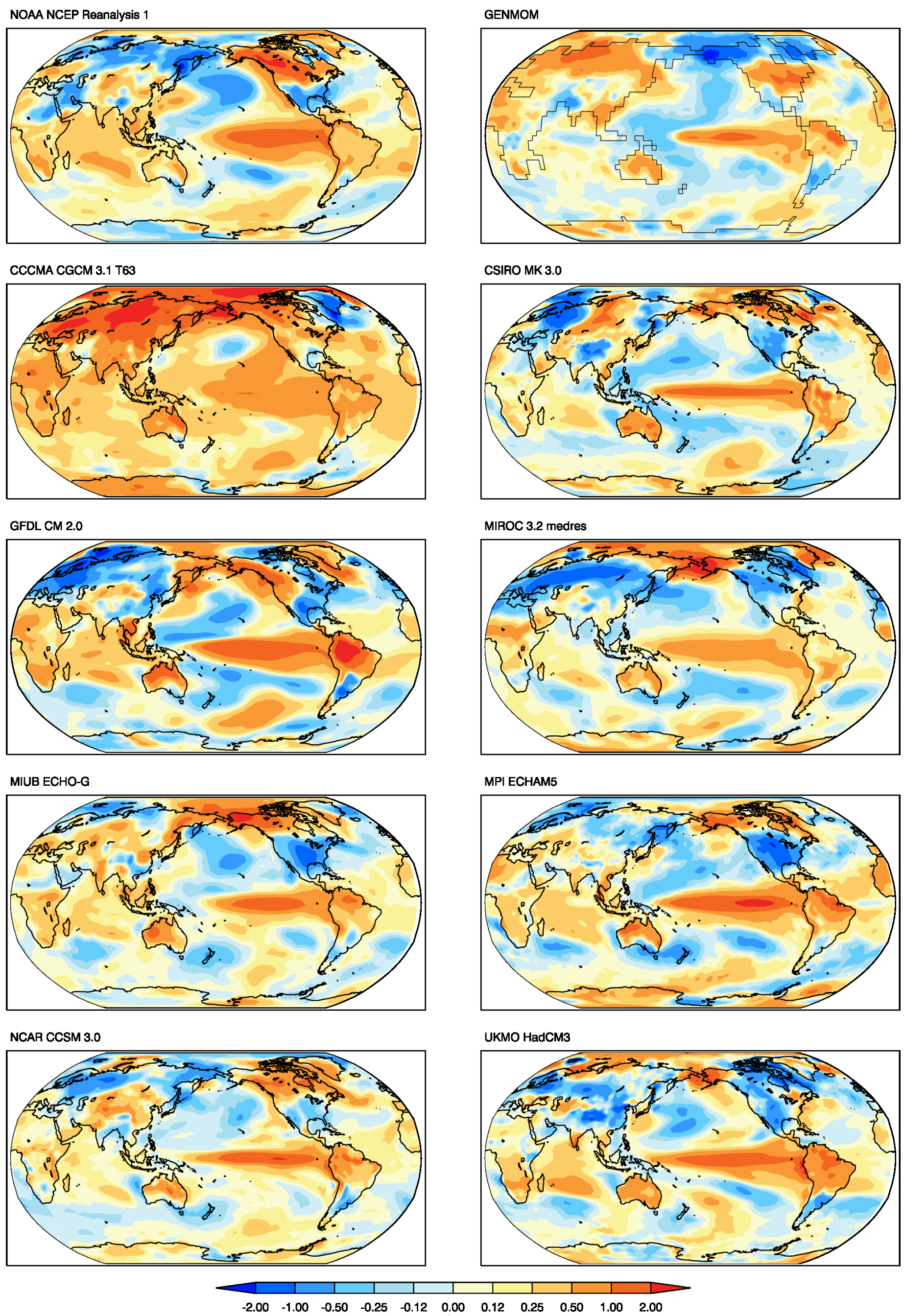

Figure 3.8 Surface air temperature (2 m) DJF El Niño composite anomalies for observed, eight IPCC AR4 models and GENMOM. Both GENMOM and IPCC AR4 models are averaged over a 60-year period.

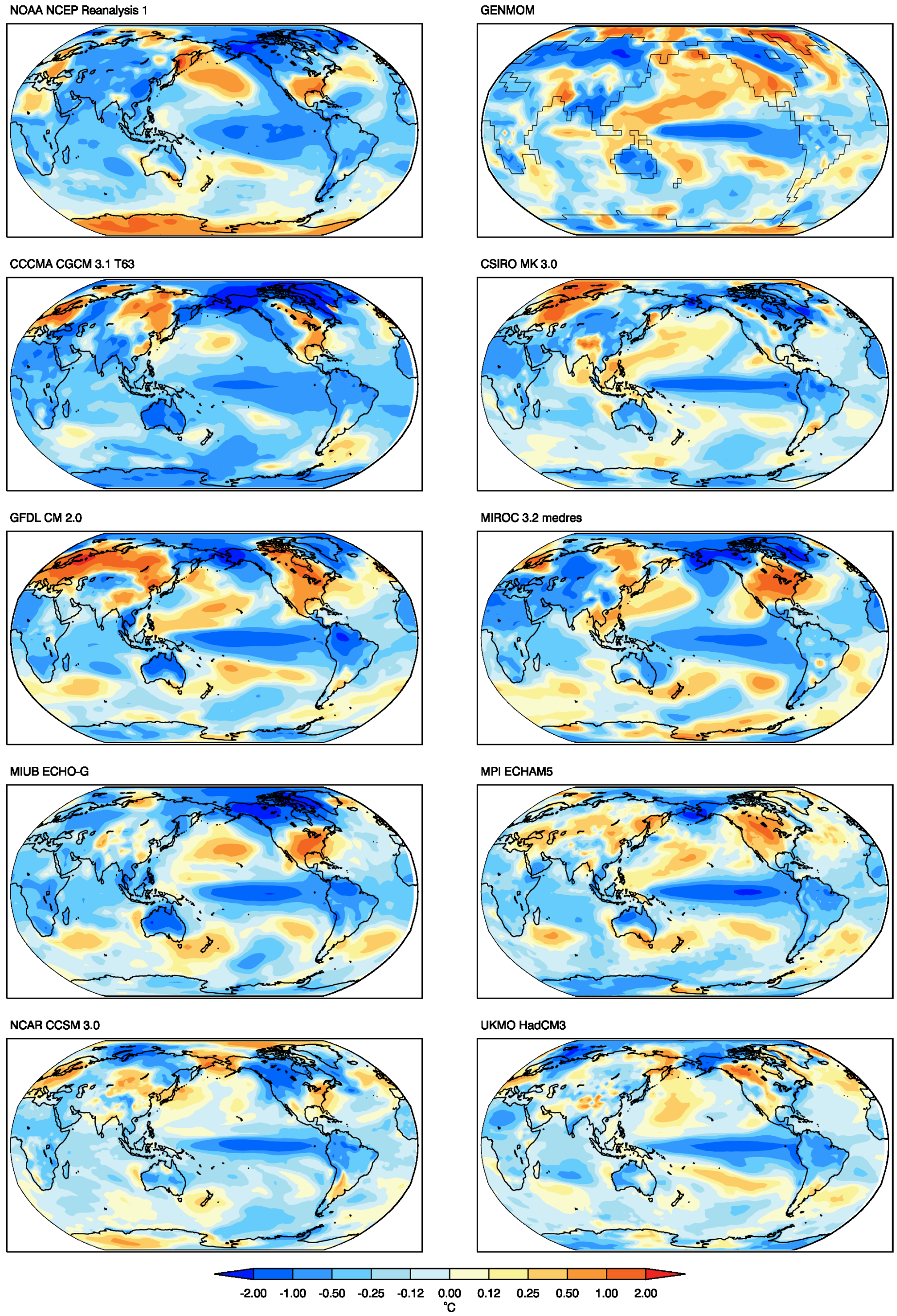

Figure 3.9 Surface air temperature (2 m) DJF La Niña composite anomalies for observed, eight IPCC AR4 models and GENMOM. Both GENMOM and IPCC AR4 models are averaged over a 60-year period.

as a strong positive anomaly in the north Pacific, but this feature is not well captured by many of the models shown here. GENMOM does simulate positive anomalies in the north Pacific, but they appear to be part of the horseshoe shape extending from the equator rather than focused in the location of the Pacific subtropical high. Similar to the El Niño composite, GENMOM simulates a temperature teleconnection to North America that generally compares well to NCEP, although the Pacific Northwest is incorrectly simulated to have a positive anomaly. Similar to many of the IPCC AR4 models shown here, GENMOM simulates a reasonable La Niña temperature teleconnection to Asia, Africa, Australia and South America, whereas Europe is simulated to have the incorrect sign of the teleconnection. Figs. 3.8 and 3.9 suggest that the models with the highest resolution do not necessarily produce the most realistic ENSO pattern. ECHO-G has the lowest resolution, which is similar to GENMOM, yet it reproduces the observed spatial pattern accurately.

During an El Niño event, warm surface waters in the western Pacific are displaced eastward along with the corresponding zone of deep tropical convection, which results in an eastward shift in precipitation and attendant drying over the far western Pacific (Fig. 3.10). GENMOM generally captures the increased precipitation in the warm tongue and the associated drying in Southeast Asia and Australia, whereas many of the IPCC AR4 models shown here have a very zonal and intense precipitation pattern. The GENMOM simulated increase in tropical Pacific precipitation is slightly too confined to the equator and does not capture enough drying in the northern tropics. GENMOM incorrectly simulates drying in the Indian Ocean during DJF El Niño events, which is not seen in the other models shown here. GENMOM simulates a drying in northern South America

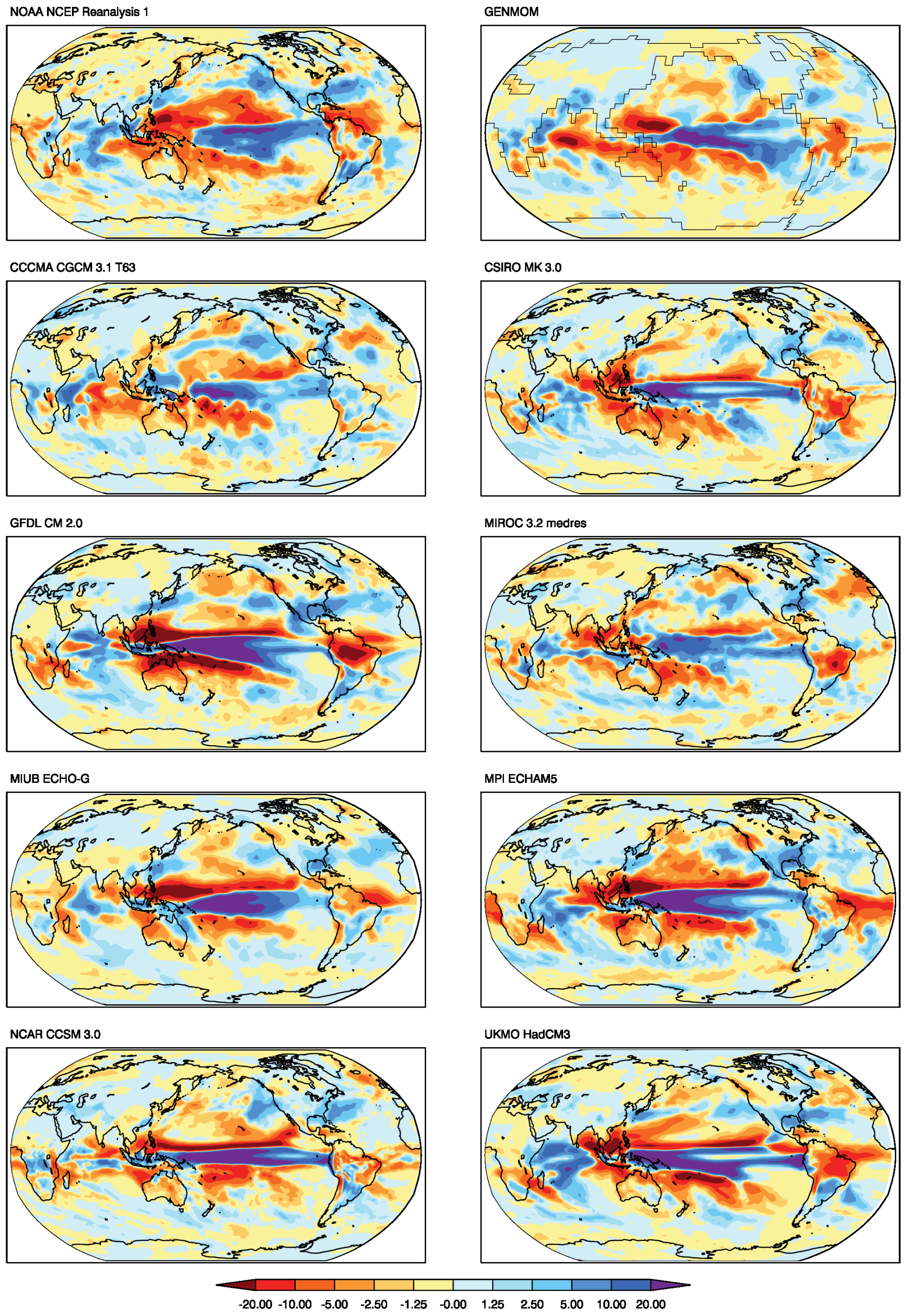

Figure 3.10 Precipitation DJF El Niño composite anomalies for observed, eight IPCC AR4 models and GENMOM. Both GENMOM and IPCC AR4 models are averaged over a 60-year period.

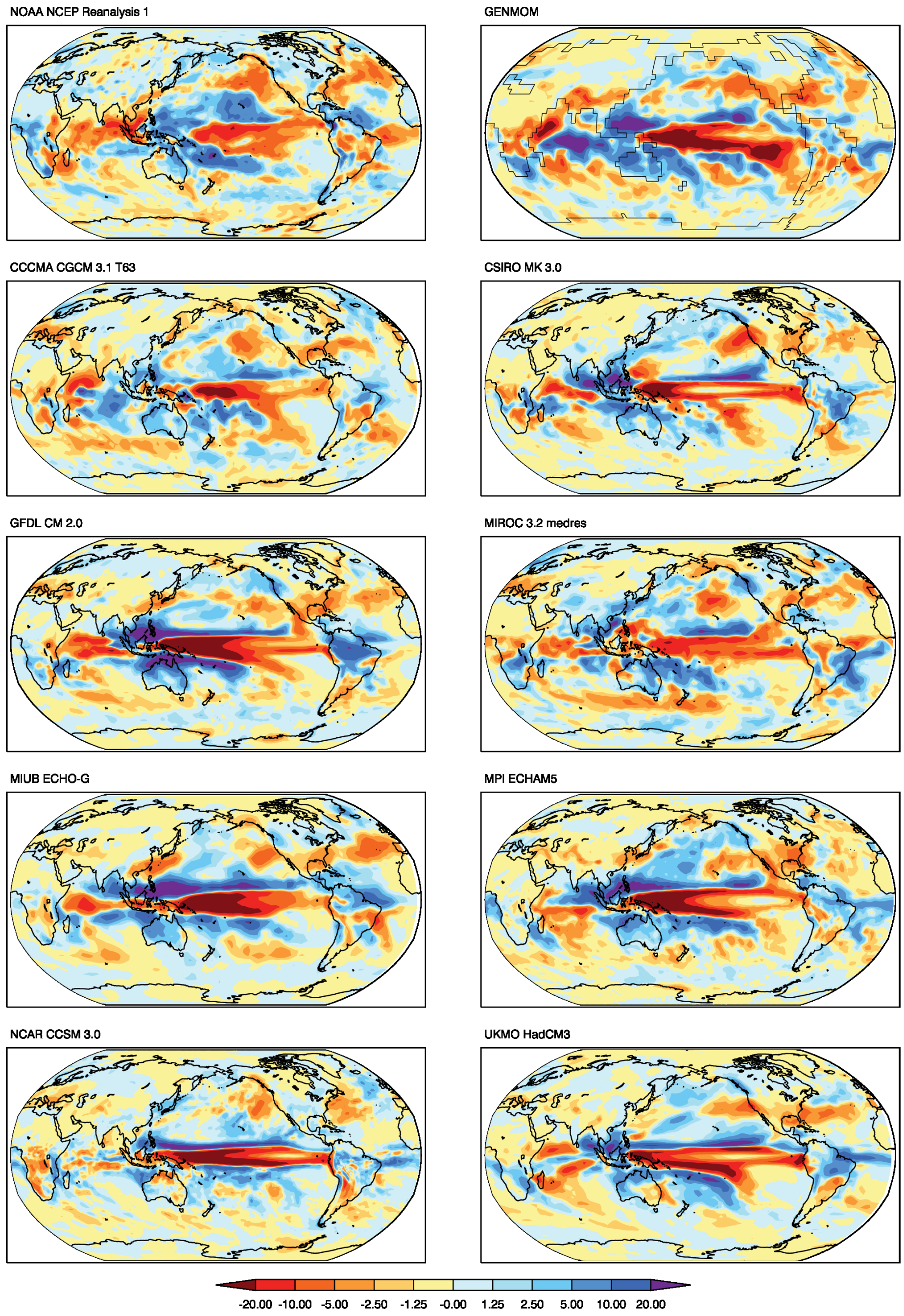

Figure 3.11 Precipitation DJF La Niña composite anomalies for observed, eight IPCC AR4 models and GENMOM. Both GENMOM and IPCC AR4 models are averaged over a 60-year period.

during El Niño events, which generally matches NCEP, whereas this drying is noticeably missing in CCCMA CGCM 3.1 and too strong in GFDL CM 2.0. During La Niña events, GENMOM simulates similar precipitation spatial patterns in the tropical Pacific compared to the observations, albeit with a stronger magnitude along the equator (Fig. 3.11).

GENMOM simulates incorrect precipitation teleconnection in the Indian Ocean, yet generally matches NCEP well in all other regions. Many of the models place a zonal reduction of precipitation in equatorial Pacific whereas GENMOM performs well compared to the observations. All of the models shown here fail to adequately capture the intensity of the observed mid-latitude teleconnections associated with cold La Niña events. GENMOM correctly simulates increased rainfall across both eastern and western coasts of North America during El Niño events, along with decreased precipitation across both coasts during La Niña events. Although the patterns of these teleconnections match NCEP, the magnitude of the North American precipitation teleconnection is weaker-than-observed on the western coast. The GENMOM simulated global precipitation teleconnections are surprisingly good when compared to observations and the IPCC models shown here despite the coarse T31 resolution and split ITCZ.

During El Niño and La Niña events the Walker circulation changes strength and the locations of vertical convection over Indonesia in the west and downward subsidence over the east Pacific. During an El Niño event the eastern Pacific subsidence weakens while western convection expands eastward relative to normal conditions. Conversely, La Niña conditions are characterized by a strengthening of both eastern subsidence and western convection, while the western convection is contracted further westward.

GENMOM reproduces both these transitions reasonably well, despite weaker-than-observed eastern subsidence and generally more confined convection and subsidence zones (not shown). In the horizontal (not shown), the zones of convection and subsidence are strongly tied to the persistent split ITCZ simulated by GENMOM (Alder et al., 2011).

3.5 Changes in ENSO with global warming

In this section we detail the response of ENSO to present day (355 ppmV), doubling (710 ppmV) and quadrupling (1420 ppmV) of atmospheric CO_2 (denoted 1x, 2x and 4x respectively). The three simulations are integrated for 700 years. The first 400 years are disregarded as model spin-up, leaving 300 years to be used in our analysis. Other trace gases such as CH_4 and N_2O were not altered from present day values. A 140-year simulation using the A2 emission scenario was performed that also include changes in CH_4 and N_2O along with CO_2.

GENMOM has a global equilibrium sensitivity of 2.5°C to a doubling of atmospheric CO_2, which is in the range of 2.1°C - 4.4°C reported in the IPCC AR4 (Meehl et al., 2007). The most dramatic warming occurs at the poles during their respective winter, which is caused by a change in the ice-albedo feedback due to reduced sea-ice distributions in the warming scenarios (not shown). All models simulate warming in the equatorial Pacific, which potentially may affect the development of ENSO events and related teleconnections (Fig. 3.12). Generally, GENMOM has a similar spatial response to a doubling of atmospheric CO_2 when compared to the IPCC AR4 models shown here. Unlike the IPCC AR4 models seen here, the GENMOM cold tongue in the eastern and central Pacific disproportionately warms more than the western Pacific. This

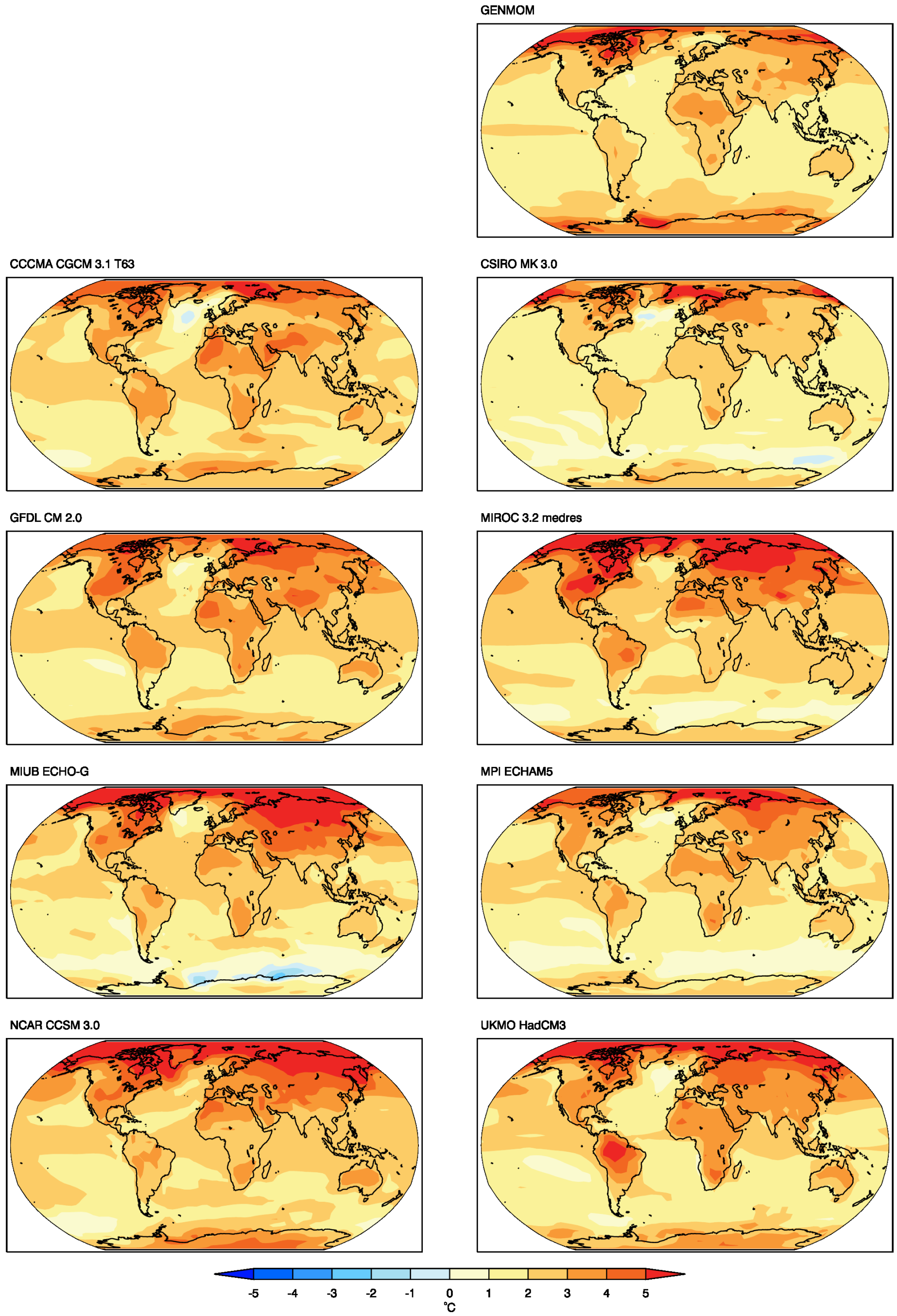

Figure 3.12 AOGCM sensitivity to a doubling of CO_2 for eight IPCC AR4 models and GENMOM. GENMOM anomalies are calculated as the last 30 years of 2x equilibrium simulation minus the last 30 years of 1x equilibrium simulation. IPCC anomalies are calculated as the 30 years surrounding double CO_2 in the SRES A2 emission scenario minus the last 30 years of the Climate of the 20th Century experiment.

asymmetric warming decreases the east-west temperature gradient in the equatorial Pacific and generally serves to allow larger anomalies (ENSO events) to develop. GENMOM has moderate warming at the North Pole and more intense warming at the South Pole compared to the other models shown here, which is likely due to differing responses of sea-ice to rising temperatures.

3.5.1 ENSO strength and frequency

The Niño 3 indices for the three equilibrium simulations are shown in Fig. 3.13; increased variability with CO_2 level is readily apparent as more temperature anomalies cross the ±0.5 °C threshold needed to meet our criteria of an ENSO event. The Niño 3 index standard deviations for the 1x, 2x and 4x simulations are 0.62, 0.70, and 0.75 respectively. Based on F-tests, the time series have statistically significant different variance at the 95% confidence level ($\sigma = 0.05$). Similar to spectral analysis, wavelet analysis not only calculates the frequency of ENSO events, but in contrast to spectral analysis, wavelet analysis also has the ability to detect the location of where frequencies change within the record. Thus, wavelet analysis reveals a more detailed evolution of ENSO spectra (Fig. 3.14) than is provided by MEM. The 1x simulation has a single 5.6 year period, while 2x and 4x simulations have 5.8 and 4.6 year periods respectively. Using normalized power spectra Guilyardi (2006) found a double peak of 3.5 and 5.3 years in the HadISST record from 1900-2000 as opposed to the single 4.3 year MEM peak in our 1948-2007 range. The double ENSO peak may be more realistic, indicating a switch from local SST-wind interaction in the central-east Pacific (S-mode) to that of remote wind-thermocline feedbacks in the west Pacific (T-mode) that are mechanisms

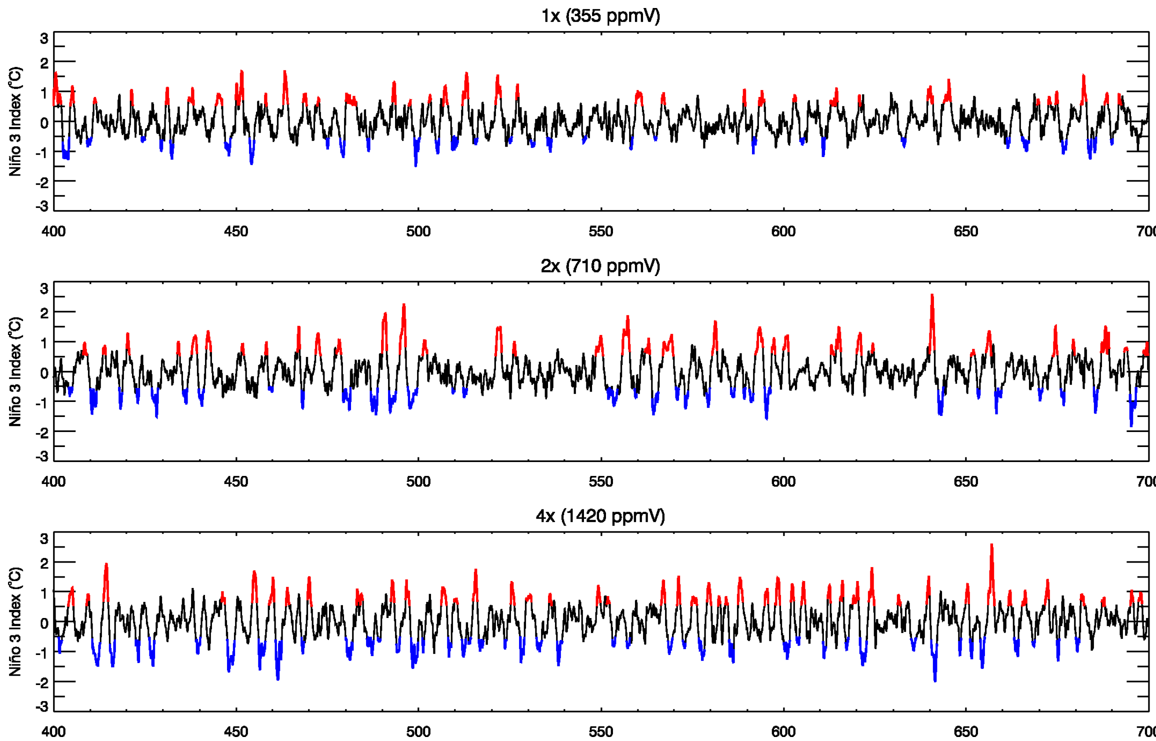

Figure 3.13 GENMOM simulated Niño 3 index for 1x, 2x and 4x with El Niño events (red) and La Niña events (blue) highlighted.

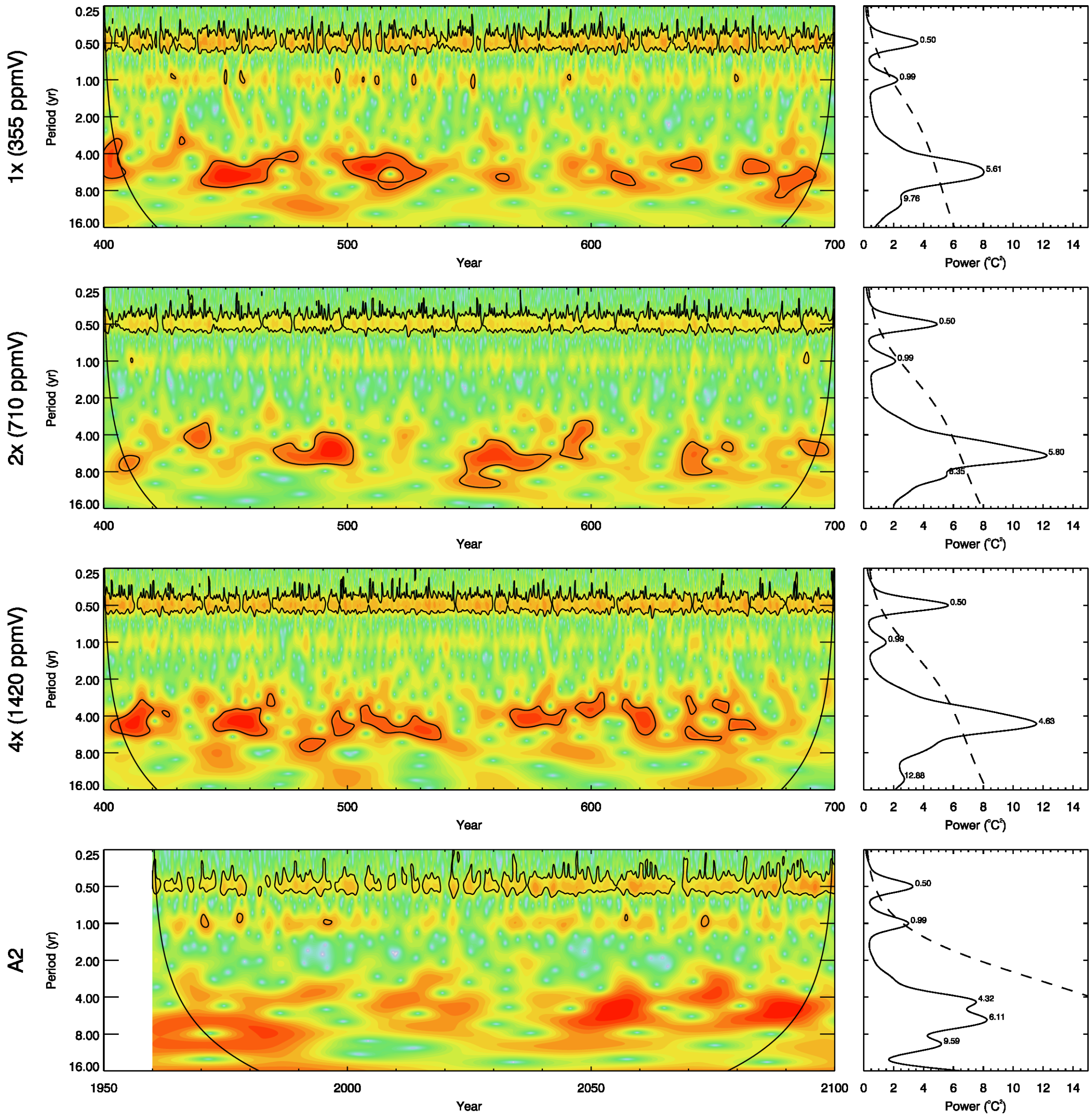

Figure 3.14 Wavelet analysis of the Niño 3 SSTs (left) with global spectra (right).

drawn on to explain the pre- and post-1976 change in observed ENSO frequency (Guilyardi, 2006).

By having one spectral peak, the 1x, 2x and 4x spectra indicate that GENMOM is simulating one mode. The 5.6 year period in the 1x simulation is similar to the longer 5.3 year observed spectral peak that Guilyardi (2006) associates with remote wind-thermocline feedbacks (T-mode). The 2x simulation has a negligible change in frequency, whereas the 4x simulation has a period about one year shorter than present. The A2 wavelet is interesting as it has a double peak of 4.3 and 6.1 years, which brackets the 1x simulation. Although the A2 wavelet is not contoured as significant, the first part of the record (1960-1990) appears to have the most power in the 6 - 9 year range, whereas the latter portion of the record (2050-2100) has more power near 4 - 6 years, potentially indicating that GENMOM is capable of switching between S and T-modes. The conclusion that GENMOM is able to switch between S and T-modes may be premature since the spectral peaks are not contoured as significant in the A2 simulation and a double peak spectra is not seen in the longer equilibrium simulations, which would indicate a shift in mode.

A noteworthy feature of the GENMOM wavelet spectra is the strong presence of a 6-month frequency, which is caused by simulation of a semi-annual cycle in eastern Pacific SSTs over the Niño 3 region. It is unclear how this semi-annual cycle influences the development of ENSO events. The observed Niño 3 index show that El Niño events typically intiate in late spring/early summer, reach their peak strength in winter, and then decay the following spring. While GENMOM does have a slight preference to peak in late winter/early spring, events can initiate anytime of the year, which is uncharacteristic of the observations (not shown).

3.5.2 Changing spatial patterns and teleconnections

A key question in understanding the potential response of ENSO to global warming is not only evaluating changes in strength and period, but also in evaluating changes in the spatial patterns of global teleconnections. Large changes in simulated ENSO dynamics are not confined to the Niño 3 region, but also occur in both Niño 3.4 and 4 regions (Fig. 3.15). Both the 2x and 4x simulations have stronger Niño 3 and 3.4 indices, but the index declines in the Niño 4 region. In the 4x case, the Niño 4 index is greatly reduced, implying an eastward contraction of the warm tongue. To provide independent confimation of this finding we apply Empirical Orthogonal Functions, which are commonly used in the fields of oceanography and atmospheric sciences to spatialy decompose different modes of independent variability (Fig. 3.16). Unlike the Niño indices that collapse the spatial variability of SSTs down to one number, EOFs are calculated on a per-grid-cell basis to reveal the spatial changes of variability in the tropical Pacific. The first EOF for the 4x scenario indicates that the western edge of the warm tongue is displaced between 15-20° to the east. The eastward shift of the warm tongue western edge is likely caused by a general weakening of the Walker circulation and a shift in the zone of convection. Under the 4x scenario, Niño 4 windstress is reduced in the western Pacific by 38% annually (Table 3.2). Reduction in west Pacific windstress is driven by a ~34% reduction in the east-west Pacific temperature gradient, which increases the western surface pressure and reduces the eastern surface pressure, thereby reducing the east-west pressure gradient and weakening the easterly tradewinds

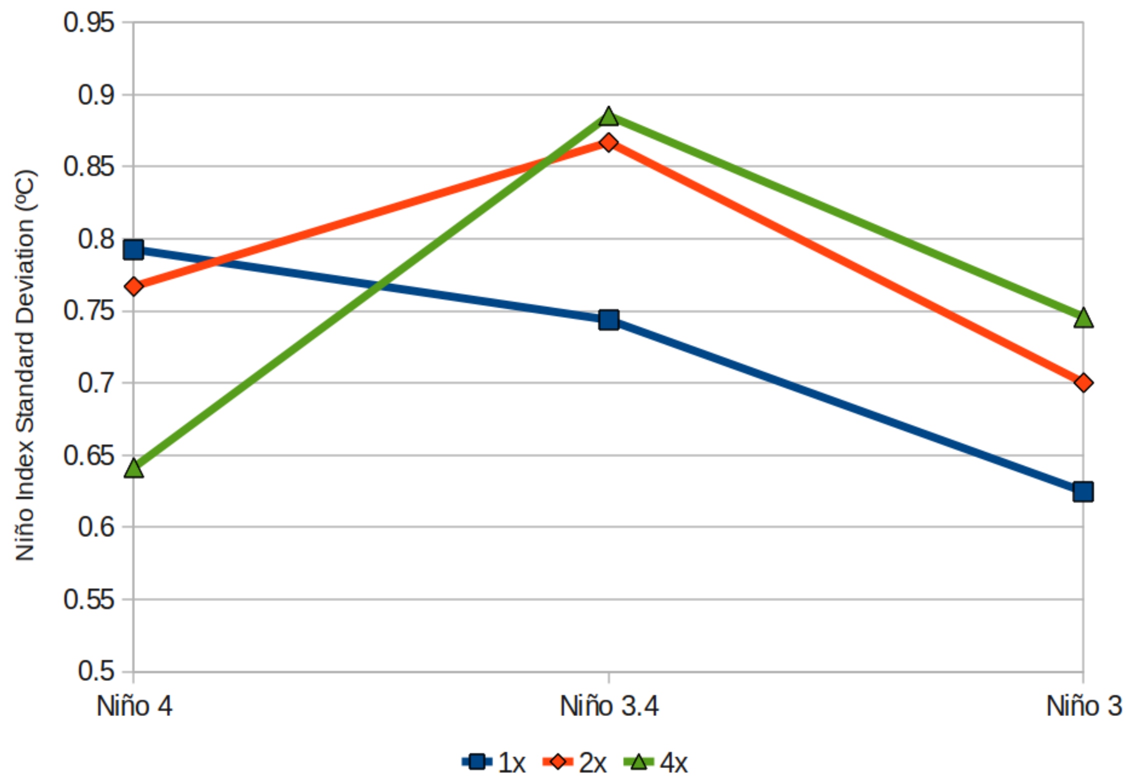

Figure 3.15 Change in Niño indices standard deviation.

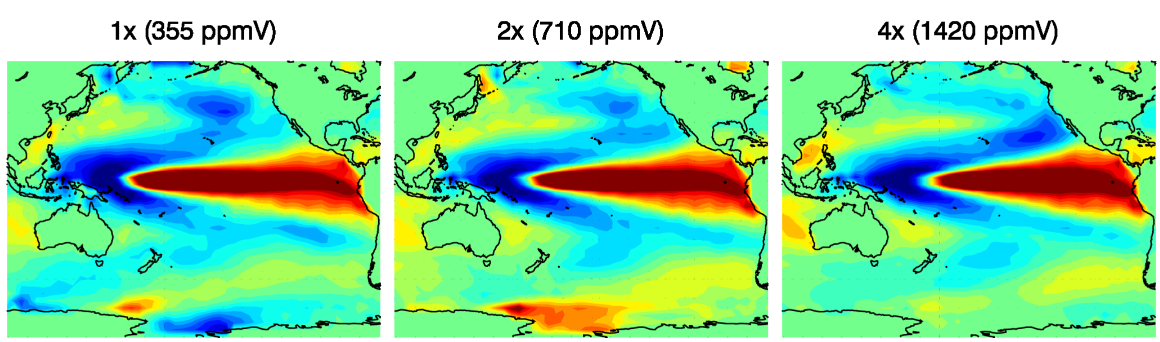

Figure 3.16 First Empirical Orthogonal Function (EOF1) of SST anomalies for the Pacific basin.

Table 3.2 Metrics of Bjerknes feedbacks. All values are shown as annual means for the full 300-year simulations. Windstress is shown as Tx. The Warm Pool (WP) is defined as 5°N - 5°S, 130°E - 170°E and the Cold Tongue (CT) as 5°N - 5°S, 130°W - 170°E. The themocline gradient is calculated as the Niño 3 SST minus the ocean subsurface temperature at 112 m for the same region. Upwelling is calculated by volume at 112 m in the Niño 3 region.

	1x	2x	4x
Niño 3 stddev (°C)	0.62	0.70	0.75
# El Niños >= 1.5	6	9	8
Niño 3 T_x (dynes/cm^2)	-0.30	-0.28	-0.26
Niño 4 T_x (dynes/cm^2)	-0.26	-0.21	-0.16
WP SST (°C)	28.14	29.51	31.39
CT SST (°C)	24.39	26.33	28.91
WP-CT (°C)	3.75	3.18	2.48
Niño 3 SST (°C)	24.58	26.55	29.15
T@112m (°C)	18.63	20.14	22.04
SST-T@112m (°C)	5.96	6.41	7.12
Niño 3 Upwelling (Sv)	119.0	101.6	80.5

(not shown). The Walker circulation in the 4x simulation is weakened and is characterized by reduced convection in the west and reduced subsidence in the east. Convection increases in the central Pacific (centered at ~160º W), indicating an eastward shift of the zone of convection. The 2x scenario generally exhibits similar patterns, but the changes are smaller than those of the 4x simulation. In both 2x and 4x scenarios the equator to pole temperature gradient is reduced relative to present day, which may be contributing to the changes in the Walker circulation.

A noteworthy feature of first EOF is that the traditional horseshoe shape is progressively more constrained to the equator in the 2x and 4x simulations in the northern hemisphere, whereas it extends to higher latitudes in the 1x simulation. This rearrangement of variability could be the expression of changes in mid-latitude teleconnections. Global surface temperature teleconnections during DJF using the Niño 3 index are shown in Fig. 3.17. Regions where the teleconnections are statistically significant ($\sigma = 0.05$) are highlighted with hatching. These results demonstrate that the teleconnections may not be stationary and could be subject to considerable reorganization in a warming world.

A notable feature in Fig. 3.17 is that during El Niño events the warm tongue appears weaker in 4x than that of the 1x simulation, despite the fact that the 4x simulation has a stronger ENSO. This apparent reduction is actually an artifact of the method used to create the composite maps, where the 4x simulation includes many more events (see Fig. 3.13), including smaller events, which collectively reduce the magnitude of the average composite. This potential pitfall could be avoided by including only the top 10-15 strongest ENSO events as opposed to all events; however the composite anomalies of

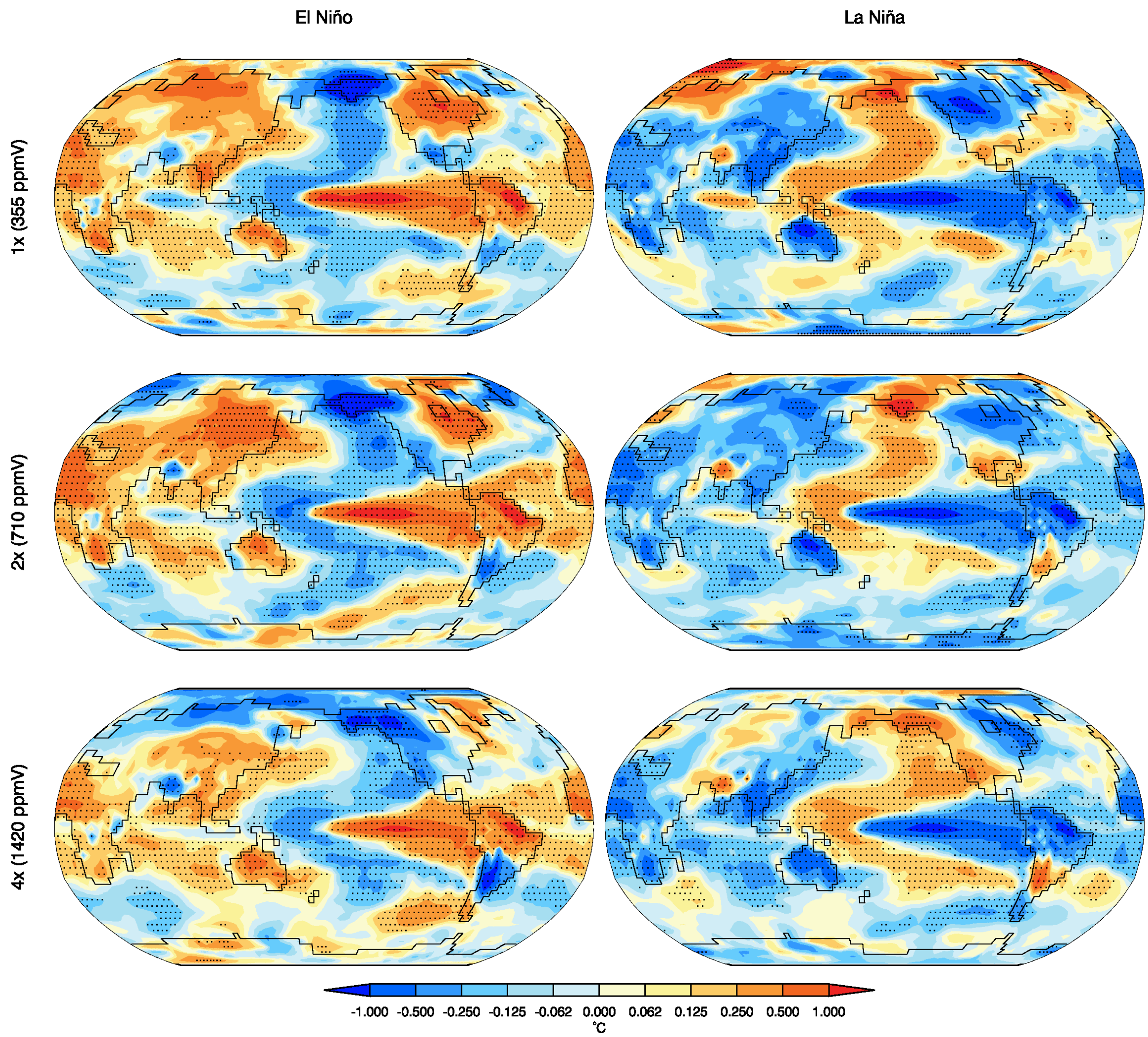

Figure 3.17 Changes in DJF surface temperature teleconnections. Statistically significant (T-test, σ = 0.05) teleconnection regions are hatched.

the teleconnections would represent only the strongest ENSO events rather than the average event.

North American teleconnections vary among the simulations and the changes from normal conditions are statistically significant in only a few regions because, as in nature, the ENSO signal is obscured by interannual variability. The cold anomaly during El Niño events and a warm anomaly during La Niña events over Alaska are weakened under the 2x and 4x simulations. The western United States has a reversal of sign in the temperature teleconnection for both El Niño and La Niña events from the 1x simulation towards the 4x simulation. Eastern Canada has a large reduction in the warm temperature anomaly during El Niño events, where the 4x simulation have a coherent pattern of sign reversal to cold temperature anomalies, although they are not hatched as significant. Over Southern South America the temperature teleconnection (negative anomalies during El Niño events and positive anomalies during La Niña events) strengthens in the 2x and 4x simulations. Africa appears to have little change in temperature teleconnections and Australia has generally the same teleconnection with only a slight reduction in the cold temperature anomaly during La Niña events. Northern Asia has a postive temperature teleconnection during El Niño events that strengthens in the 2x simulation, then weakens and reverses sign to a negative cool anomaly in the 4x simulation, which similar to the NCEP present-day teleconnection (Fig. 3.8).

Precipitation teleconnections (Fig. 3.18) are far less globally extensive than temperature teleconnections. Despite large changes in the temperature teleconnection over North America, the precipitation teleconnections in the 1x and 4x simulations are generally similar with a small reduction of precipitation anomalies in the 4x simulation

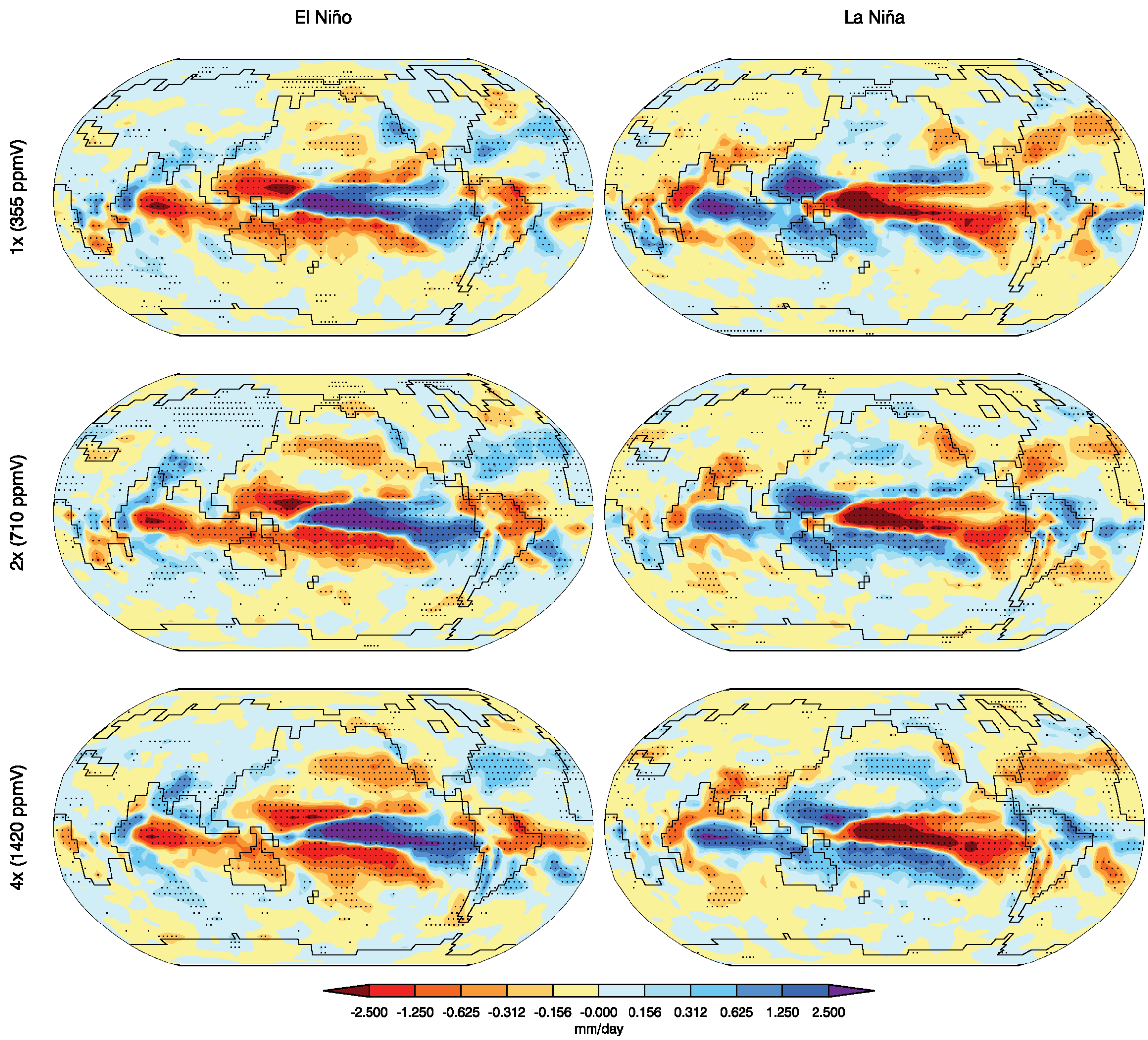

Figure 3.18 Changes in DJF precipitation teleconnections. Statistically significant (T-test, σ = 0.05) teleconnection regions are hatched.

over eastern and western United States during both El Niño and La Niña events. Similar to temperature, southern South America has a strengthening precipitation teleconnection. Again, Africa has little change in the spatial pattern of ENSO teleconnections. The Indian subcontinent has a stronger wet anomaly under the 2x simulated and 4x simulated El Niño events while also having a similar dry anomaly during La Niña events. Eastern Australia has a weakening precipitation anomaly from the 1x simulation to the 4x simulation for both El Niño and La Niña events, perhaps due to the eastward shift of the Walker Circulation.

3.5.3 Metrics and mechanisms of ENSO

Our analysis demonstrates that GENMOM produces stronger and more frequent ENSO events with increased atmospheric CO_2 concentrations. Potential sources for driving the increased amplitude of ENSO are 1) steepening of the tropical thermocline temperature gradient, 2) weakening of the zonal east-west Pacific surface temperature gradient and or 3) the meridional extent of the zonal wind stress response to equatorial SST anomalies (Merryfield, 2006). The combination of these sources can be viewed in the context of positive and negative feedbacks that enhance or suppress ENSO events in the model. Relaxing the Bjerknes feedbacks and the Walker Circulation can allow larger SST and wind anomalies to build, thereby setting the stage for the development of stronger El Niño events. In contrast, enhancing the Walker Circulation and Bjerknes feedbacks would result in a tendency for a more ‘locked’ system that would suppress building of SST which in turn would weaken ENSO events.

To determine the driving force behind changes in ENSO strength, Otto-Bliesner et al. (2003) investigated mean state changes in the tropical Pacific finding that changes in the strength of Bjerknes feedbacks can be tied to ENSO strength. In Table 3.2 we list some of the basic metrics of the Bjerknes feedbacks that control the strength of ENSO in an attempt to understand why GENMOM simulates stronger ENSO events under global warming. One of the simplest metrics is the zonal SST gradient across the Pacific basin. Here we use the Warm Pool (WP, 5°N - 5°S, 130°E - 170°E) and the Cold Tongue (CT, 5°N - 5°S, 130°W - 170°E) to define the zonal temperature gradient as WP-CT. There is a decreasing zonal temperature gradient from the 1x simulation to the 4x simulation, with the 4x simulation exhibiting the weakest zonal gradient (Table 3.2).

Another metric for ENSO related variability in the eastern Pacific is the vertical thermocline temperature gradient, which is used to infer both upper ocean temperature stratification and the strength of upwelling. To quantify the thermocline gradient, we use the sea surface temperature minus the ocean temperature at 112 meters in the Niño 3 region. The thermocline gradient is weakened from 3.75 °C in the 1x simulation to 2.48 °C in the 4x simulation, which is a reduction of ~34%. East Pacific coastal upwelling is by and large driven by the windstress from easterly trade winds, where stronger winds strengthen the upwelling of cold subsurface water. Stronger upwelling will generally cool the eastern Pacific, which increases the east-west temperature gradient, as the western Warm Pool remains warm, resulting in stronger trade winds and more upwelling. Here we calculate upwelling as the volume of water moving vertically at 112 m depth in the Niño 3 region. Upwelling in this region is reduced from 119.0 Sv in the 1x simulation to 80.5 in the 4x simulation (~32%). The reduction in upwelling corresponds to a 38% reduction in west Pacific Niño 4 windstress and ~34% reduction in the east-west Pacific temperature gradient, all of which culminate to strengthen ENSO events in the 4x simulation.

In agreement with Otto-Bliesner et al. (2003), the strongest ENSO events simulated with GENMOM display the weakest zonal temperature gradient, the steepest thermocline gradient and the weakest wind stress (T_x), which together indicate weakening of Bjerknes feedbacks which reinforce building of larger anomalies, thereby strengthening ENSO events. From these Bjerknes feedbacks, we would expect a weaker zonal SST gradient, weaker wind stress and reduced upwelling, which is indicated by a sharper themocline. Of our equilibrium simulations, the 4x simulation displays these aspects of Bjerknes feedbacks and the resulting strongest ENSO events of our three equilibrium simulations.

The strength of the AMOC is thought to play a role as an extra-tropical control of ENSO strength by altering the background seasonal cycle in the Pacific via an atmospheric bridge to the Atlantic. Using five AOGCMs, Timmermann et al. (2007) finds weakening the AMOC tends to weaken the annual cycle in the Pacific, which in turn strengthens ENSO. Our simulations display a weakening of the AMOC and a strengthening ENSO with global warming. The AMOC strength is reduced from 14.5 ± 0.7 Sv in the 1x simulation to 11.5 ± 0.7 Sv and 11.3 ± 2.0 Sv in the 2x and 4x simulations respectively. Our results corroborate with those of Timmermann et al. (2007), where the AMOC is weakened from the 1x to 4x simulation, which corresponds to the annual cycle weakening in our 2x and 4x wavelet spectra (Fig. 3.14). However, it is unclear how the strength of the AMOC alters the semi-annual cycle, and how the semi-annual cycle alters GENMOM's ability to simulate ENSO events.

To explain changes in the frequency of ENSO events in a warming world, we must consider how El Niño events first develop. In the delayed-oscillator paradigm (Schopf and Suarez, 1988; Suarez and Schopf, 1988; Battisti and Hirst, 1989), Kelvin and Rosby waves are thought to be associated with the triggering of ENSO events. Both Kelvin and Rosby waves are formed from anomalous westerly wind bursts in the equatorial Pacific. A fast moving (~1 m/s) downwelling Kelvin wave will propagate eastward from the location of the wind burst, deepening the thermocline, reducing upwelling, and effectively warming east Pacific SSTs. Whereas the slower (2.5 - 3m/s) westward propagating upwelling Rosby wave raises the thermocline as it travels towards the western boundary. These two opposite moving waves setup a temporary weakening of the Pacific east-west surface temperature gradient, which is strengthened by wind-SST feedbacks that further weaken the temperature gradient, leading to the development of an El Niño event. However, as the eastward propagating Kelvin wave reaches the eastern boundary, it is reflected back westward as a slow moving downwelling Rosby wave, just as the Rosby wave is reflected eastward as an upwelling Kelvin wave. The reflected waves will essentially reverse the warming of the original two waves, aiding to the decay of the El Niño event. The leading proposed mechanism to explain why ENSO events would be more frequent with global warming is that the rate at which Kelvin and Rosby waves propagate across the Pacific basin increases as water temperature increases (Chelton et al., 1998; Merryfield, 2006). If the waves propagate faster across the Pacific Basin, then the frequency of ENSO events would increase.

3.6 Discussion

GENMOM produces a realistic ENSO that is on par with the eight IPCC AR4 models evaluated here by simulating Niño 3 - 4 indices that have a standard deviation within 0.3 °C of the observations. The model simulates ENSO events with a realistic frequency and generally correct spatial patterns of temperature and precipitation teleconnections. GENMOM simulates a weaker-than-observed Peru Current and coastal upwelling in the eastern Pacific, both of which contribute to the simulated eastern Pacific SSTs being too warm and too zonal. The wintertime (DJF) Walker Circulation is well simulated with generally the correct positioning, albeit with slightly weaker-than-observed convection and subsidence. The summertime (JJA) Walker Circulation is also weaker-than-observed, however both the zone of convection and subsidence are displaced westward due to an incorrect simulation of east and west Pacific SSTs. GENMOM produces a semi-annual temperature seasonal cycle that is not seen in the observations but is not uncommon in AOGCMs (Guilyardi, 2006). GENMOM incorrectly produces peak SST variability in the Niño 4 region as opposed to the observed Niño 3 region, which is also common in other non-flux corrected AOGCMs, and is another indication that the model produces ENSO events with incorrect seasonal timing. Wavelet analysis indicates that GENMOM produces ENSO events with an average period of 5.6 years. However, the shorter A2 simulation hints that GENMOM is capable of simulating the two distinct spectral peaks seen in the observations that indicate that GENMOM correctly simulates both the S-mode and T-mode mechanisms that drive ENSO.

Long (300-year) CO_2 sensitivity experiments show that GENMOM simulates more frequent and higher amplitude ENSO events with CO_2-driven global warming, specifically at 4x atmospheric CO_2 levels. ENSO events are more intense due to CO_2 induced warming disproportionately heating the eastern Pacific more than the western Pacific, such that the east-west temperature gradient is reduced by ~34% in the 4x simulation. The weakened east-west temperature gradient slackens weak Pacific windstress by 38% and thereby weakening upwelling by ~32% in the 4x simulation. As these Bjerknes feedbacks are weakened in the equatorial Pacific, larger anomalies, and hence ENSO events, develop. This result should, however, be interpreted with caution as the IPCC AR4 indicates that there is yet to be consensus among the models on how ENSO will respond to global warming. The IPCC AR4 models are divided between a more intense ENSO and a weakened ENSO in response to global warming (Merryfield, 2006). The A2 emission scenario is too short in length to be able to definitively detect changes in the ENSO spectra, yet wavelet analysis tentatively mirror the same trend of increased frequency with increasing green house gases.

The simulations performed here not only have a strengthened and more frequent ENSO in a warming world, but also one with a changing spatial pattern. The sharp reduction of SST variability in the Niño 4 region under the 4x scenario is representative of an eastward contraction of the region of action of ENSO. This finding is confirmed by the first EOF of SST anomalies showing a 15-20° shift in the region of action. The strength of the Walker Circulation is found to be reduced through a weakening of Bjerknes feedbacks (western windstress and convection are reduced, eastern subsidence and upwelling are reduced, and the west-east Pacific temperature gradient is weakened) while the zone of deep tropical convection is displaced eastward.

Although each ENSO event is unique and GENMOM produces substantial spatial variability between events, focusing on regions where teleconnections are statistically significant leads to some interesting findings. The GENMOM simulations have a complete sign reversal for the temperature anomalies for the western United States during both El Niño and La Niña events from the 1x simulation towards 4x atmospheric CO_2. If such a reversal were to occur in the future, it would undoubtedly have vast ecological, agricultural and economical impacts. La Niña events are associated with dry conditions in the southwest United States, where strong or prolonged La Niña conditions can trigger drought that can persist beyond the duration of the La Niña event (Cole and Overpeck, 2002). Although La Niña events bring dry conditions to the southwest, the temperature teleconnection is one of cooling. If the temperature teleconnection reverses, while the precipitation teleconnection generally stays the same, the warm temperature teleconnection could exasperate La Niña triggered drought. GENMOM also simulates reduced precipitation teleconnections to both coasts of the United States in the 2x and 4x simulations. Southern South America has strengthening temperature and precipitation anomalies during both El Niño and La Niña events. The Indian subcontinent has a stronger precipitation anomalies under 2x and 4x El Niño events.

As simulations for the Fifth Assessment Report (AR5) are completed, additional attention should be given to studying ENSO by encouraging modeling groups to submit long (300+ year) equilibrium simulations for both 2x and 4x atmospheric CO_2. Although transient simulations are more realistic, it becomes difficult to detect changing teleconnection patterns or to place significance on teleconnections when the simulations are short or the forcing is constantly changing. Moreover, models that exhibit multi-decadal modulation of ENSO amplitude (Timmermann, 2003; Yeh and Kirtman, 2004; Lin, 2007), as GENMOM displays, require longer simulations, as it becomes difficult to separate a CO_2 forced change from the modulation. Perhaps having long equilibrium simulations for all AR5 models will help build a consensus on how models predict ENSO will respond to increasing green house gases, unlike the division between models seen today. This proposed set of long equilibrium simulations could also be explored to determine if there is any consistency within the models to support changing spatial teleconnections with global warming.

3.7 Acknowledgements

We thank the UK Meteorological Office Hadley Centre and NOAA/OAR/ESRL PSD, Boulder, Colorado, USA for providing access to datasets. We acknowledge the modeling groups, the Program for Climate Model Diagnosis and Intercomparison (PCMDI) and the WCRP's Working Group on Coupled Modelling (WGCM) for their roles in making available the WCRP CMIP3 multi-model dataset. Support of this dataset is provided by the Office of Science, U.S. Department of Energy. The GECCO dataset was provided by the ECCO Consortium for Estimating the Circulation and Climate of the Ocean funded by the National Oceanographic Partnership Program (NOPP).

3.8 References

AchutaRao, K. and K. R. Sperber, 2002: Simulation of the El Niño Southern Oscillation: Results from the Coupled Model Intercomparison Project. Climate Dyn., 19, 191–209.

AchutaRao, K. and K. R. Sperber, 2006: ENSO simulation in coupled ocean-atmosphere models: Are the current models better? Climate Dynamics, 10.1007/s00382-006-0119-7.

Alder, J.R., Hostetler, S., Pollard, D., Schmittner, A.: Evaluation of a present day climate simulation with a new coupled atmosphere-ocean model GENMOM, Geoscientific Model Development, 4, 69-83, doi:10.5194/gmd-4-69-2011, 2011.

Battisti, D. S., and Hirst, A. C.: Interannual variability in the tropical atmosphere/ocean system: Influence of the basic state, ocean geometry and nonlinearity, J. Atmos.Sci., 46, 1687-1712, 1989.

Bjerknes, J.: Atmospheric teleconnections from the equatorial Pacific. Monthly Weather Review, 96, 163-172, 1969.

Chelton, D. B., deSzoeke, R. A., Schlax, M. G., Naggar, K. E., and Siwertz, N.: Geographical variability of the first baroclinic Rossby radius of deformation. J. Phys. Oceanogr., 28, 433–460, 1998:.

Clement, A.C., Seager, R., and Cane, M.A.: Orbital controls on the El Niño/Southern Oscillation and the tropical climate, Paleoceanography, 14, 441 – 456, 1999.

Cole, J.E., and Overpeck, J.T.: Multiyear La Nina events and persistent drought in the contiguous United States. Geophysical Research Letters, vol 29, no. 13, pg 1647, doi:10.1029/2001GL013561, 2002.

Collins, M.: Uncertainties in the response of ENSO to Greenhouse Warming, Geophys. Res. Lett., 27, 3509–3513, 2000a.

Collins, M.: The El-Niño Southern Oscillation in the second Hadley Centre coupled model and its response to greenhouse warming. J. Climate, 13, 1299–1312, 2000b.

Collins, W.D., et al.: Description of the NCAR Community Atmosphere Model (CAM3.0). Technical Note TN-464+STR, National Center for Atmospheric Research, Boulder, CO, 214 pp, 2004.

Dettinger M.D., Ghil, M., Strong C.M., Weibel, W., Yiou, P.: Software expedites singular-spectrum analysis of noisy time series. Eos 76: 12, 1995.

Flato, G.M.: The Third Generation Coupled Global Climate Model (CGCM3) (and included links to the description of the AGCM3 atmospheric model). http://www.cccma.bc.ec.gc.ca/models/cgcm3.shtml , 2005

GFDL GAMDT (The GFDL Global Atmospheric Model Development Team): The new GFDL global atmosphere and land model AM2- LM2: Evaluation with prescribed SST simulations. J. Clim., 17, 4641– 4673, 2004.

Giannini, A., Chiang, J. C. H., Cane, M. A., Kushnir, Y. and Seager, R.: The ENSO teleconnection to the tropical Atlantic Ocean: Contributions of the remote and local SSTs to rainfall variability in the tropical Americas. J. Clim.,14, 4530 – 4544, 2001.

Gnanadesikan, A., Dixon, K.W., Griffies, S.W., et al.: GFDL's CM2 global coupled climate models–Part 2: The baseline ocean simulation, J. Climate, 19, 675–697, 2004.

Gordon, C., et al.: The simulation of SST, sea ice extents and ocean heat transports in a version of the Hadley Centre coupled model without flux adjustments. Clim. Dyn., 16, 147–168, 2000.

Gordon, H.B., et al.: The CSIRO Mk3 Climate System Model. CSIRO Atmospheric Research Technical Paper No. 60, Commonwealth Scientific and Industrial Research Organisation Atmospheric Research, Aspendale, Victoria, Australia, 130 pp, http://www.cmar.csiro.au/e-print/ open/gordon_2002a.pdf, 2002.

Guilyardi, E.: El Niño–mean state–seasonal cycle interactions in a multi-model ensemble. Climate Dynamics, 26, 329–348, 2006.

Horel, J. D., and Wallace, J. M.: Planetary-scale atmospheric phenomena associated with the Southern Oscillation. Mon. Wea. Rev., 109, 813–829, 1981.

K-1 Model Developers.: K-1 Coupled Model (MIROC) Description. K-1 Technical Report 1 [Hasumi, H., and S. Emori (eds.)]. Center for Climate System Research, University of Tokyo, Tokyo, Japan, 34 pp., http://www.ccsr.u-tokyo.ac.jp/kyosei/hasumi/MIROC/tech-repo.pdf, 2004.

Kalnay, E., Kanamitsu, M., Kistler, R., Collins, W., Deaven, D., Gandin, L., Iredell, M., Saha, S., White, G., Woollen, J., Zhu, Y., Leetmaa, A., Reynolds, B., Chelliah, M., Ebisuzaki, W., Higgins, W., Janowiak, J., Mo, K.C., Ropelewski, C., Wang, J., Jenne, R., and Joseph, D.: The NCEP/NCAR 40-Year Reanalysis Project. Bulletin of the American Meteorological Society, 77, 437-471, 1996.

Köhl, A. and Stammer, D.: Decadal sea level changes in the 50-year GECCO ocean synthesis. J. Climate, 21, 1876–1890, 2008.

Lin, J.L.: Interdecadal variability of ENSO in 21 IPCC AR4 coupled GCMs, Geophys. Res. Lett., 34: L12702, doi:10.1029/2006GL028937, 2007.

Liu, Z., Kutzbach, J. and Wu, L.: Modeling climate shift of El Nino variability in the Holocene, Geophys. Res. Lett., 27, 2265 – 2268, 2000.

Marsland, S.J., Haak, H., Jungclaus, J.H., Latif, M., and Röske, F.: The Max-Planck-Institute global ocean/sea ice model with orthogonal curvilinear coordinates. Ocean Modelling, 5, 91–127, 2003.

McFarlane, N.A., Boer, G.J., Blanchet, J.-P. and Lazare, M.: The Canadian Climate Centre second-generation general circulation model and its equilibrium climate. J. Clim., 5, 1013–1044, 1992.

Meehl, G.A., Stocker, T.F., Collins, W.D., Friedlingstein, P., Gaye, A.T., Gregory, J.M., Kitoh, A., Knutti, R., Murphy, J.M., Noda, A., Raper, S.C.B., Watterson, I.G., Weaver, A.J., and Zhao, Z.-C.: Global Climate Projections. In: Climate Change 2007: The Physical Science Basis. Contribution of Working Group I to the Fourth Assessment Report of the Intergovernmental Panel on Climate Change [Solomon, S., D. Qin, M. Manning, Z. Chen, M. Marquis, K.B. Averyt, M. Tignor and H.L. Miller (eds.)]. Cambridge University Press, Cambridge, United Kingdom and New York, NY, USA, 2007.

Merryfield, W. J.: Changes to ENSO under CO2 doubling in a multimodel ensemble. J. Climate, 19, 4009–4027, 2006.

Nakićenović, N, Davidson, O., Davis, G., Grübler A., Kram, T., La Rovere, E.L., Metz, B., Morita, T., Pepper, W., Pitcher, H., Sankovski, A., Shukla, P., Swart, R., Watson, R., Dadi, Z.: IPCC Special Report on Emissions Scenarios. Cambridge Univ. Press, Cambridge,UK, 2000.

Neelin, J. D., Battisti, D. S., Hirst, A. C., Jin, F.-F., Wakata, Y., Yamagata, T. and Zebiak, S.E.: ENSO theory, J. Geophys.Res., 103, 14,261–14,290, 1998.

Otto-Bliesner, B. L., Brady, E. C., Shin, S.-I., Liu, Z. and Shields, C.: Modeling El Niño and its tropical teleconnections during the last glacial–interglacial cycle. Geophys. Res. Lett., 30, 2198, doi:10.1029/2003GL018553, 2003.

Pacanowski, R.C., Dixon, K. and Rosati, A.: The GFDL Modular Ocean Model Users Guide, Version 1.0. GFDL Ocean Group Technical Report No. 2, Geophysical Fluid Dynamics Laboratory, Princeton, NJ, 1993.

Pacanowski, R.C.: MOM 2 Version 2.0 (Beta) Documentation: User's Guide and Reference Manual. NOAA GFDL Ocean Technical Report 3.2, 329 pp, 1996.

Pollard, D. and Thompson, S.L.: Use of a land-surface-transfer scheme (LSX) in a global climate model (GENESIS): The response to doubling stomatal resistance. Global and Planetary Change, 10, 129-161, 1995.

Pollard, D. and Thompson, S.L.: Climate and ice-sheet mass balance at the last glacial maximum from the GENESIS version 2 global climate model. Quaternary Science Reviews, 16, 841–864, 1997.

Pope, V.D., Gallani, M.L., Rowntree, P.R. and Stratton, R.A.: The impact of new physical parametrizations in the Hadley Centre climate model: HadAM3. Clim. Dyn., 16, 123–146, 2000.

Quinn, W. H., Zopf, D.O., Short, K. S. and Yang Kuo, R.T.W.: Historical trends and statistics of the Southern Oscillation, El Niño, and Indonesian droughts. Fish. Bull., 76,663–678, 1978.

Randall, D.A., Wood, R.A., Bony, S., Colman, R., Fichefet, T., Fyfe, J., Kattsov, V., Pitman, A., Shukla, J., Srinivasan, J., Stouffer, R.J., Sumi, A., and Taylor, K.E.: Climate Models and Their Evaluation. In: Climate Change 2007: The Physical Science Basis. Contribution of Working Group I to the Fourth Assessment Report of the Intergovernmental Panel on Climate Change [Solomon, S., D. Qin, M. Manning, Z. Chen, M. Marquis, K.B. Averyt, M.Tignor and H.L. Miller (eds.)]. Cambridge University Press, Cambridge, United Kingdom and New York, NY, USA, 2007.

Rasmusson, E. M., and T. H. Carpenter, 1982: Variations in tropical sea surface temperature and surface wind fields associated with the Southern Oscillation/El Niño. Mon. Wea. Rev.,110, 354–384.

Roeckner, E., et al.: The Atmospheric General Circulation Model ECHAM4: Model Description and Simulation of Present-Day Climate. MPI Report No. 218, Max-Planck-Institut fü r Meteorologie, Hamburg, Germany, 90 pp, 1996.

Roeckner, E., Bäuml, G., Bonaventura, L., et al.: The Atmospheric General Circulation Model ECHAM5. Part I: Model Description, MPI Report 349, Max Planck Institute for Meteorology, Hamburg, Germany, 127 pp., 2003.

Ropelewski, C. F. and Halpert, M. S.: Global and regional scale precipitation patterns associated with the El Niño/Southern Oscillation cycle. Mon. Wea. Rev., 115, 1606-1626, 1987.

Schopf, P.S., and Suarez, M. J.: Vacillations in a coupled ocean-atmosphere model, J. Atmos. Sci., 45, 549-566, 1988.

SCOR.: Prediction of El Niño. Proc. No. 19, Paris, France, Scientific Committee for Ocean Research Working Group 55, 47–51, 1983.

Smith, R.D., and Gent, P.R.: Reference Manual for the Parallel Ocean Program (POP), Ocean Component of the Community Climate System Model (CCSM2.0 and 3.0). Technical Report LA-UR-02-2484, Los Alamos National Laboratory, Los Alamos, NM, http://www.ccsm. ucar.edu/models/ccsm3.0/pop/, 2002.

Suarez, M. J., and Schopf, P.S.: A delayed action oscillator for ENSO, J. Atmos. Sci., J5, 3283-3287, 1988.

Timmermann, A.: Decadal ENSO amplitude modulations: A nonlinear paradigm. Global Planet. Change, 37, 135-156, 2003.

Timmermann, A., Latif, M., Bacher, A., Oberhuber, J. and Roeckner, E.: Increased El Niño frequency in a climate model forced by future greenhouse warming. Nature, 398, 694-696, 1999.

Timmermann A., Okumura, Y., An, S.-I., Clement, A., Dong, B., Guilyardi, E., Hu, A., Jungclaus, J., Krebs, U., Renold, M., Stocker, T.F., Stouffer, R.J., Sutton, R., Xie, S.-P., Yin, J.: The influence of a weakening of the Atlantic meridional overturning circulation on ENSO. Journal of Climate, 20, 4899- 4919, 2007.

Thompson, S.L. and Pollard, D.: A global climate model (GENESIS) with a land-surface-transfer scheme (LSX). Part 1: Present-day climate. J. Climate, 8, 732-761, 1995.

Thompson, S.L. and Pollard, D.: Greenland and Antarctic mass balances for present and doubled CO2 from the GENESIS version 2 global climate model. J. Climate, 10, 871-900, 1997.

Trenberth, K.E.: The definition of El Niño. Bulletin of the American Meteorological Society 78, 2771–2777, 1997.

UK Meteorological Office, Hadley Centre: HadISST 1.1 - Global sea-Ice coverage and SST (1870-Present), [Internet]. British Atmospheric Data Centre, Downloaded 2/8/2010. Available from http://badc.nerc.ac.uk/data/hadisst/, 2006.

Wolff, J.-O., Maier-Reimer, E. and Lebutke, S.: The Hamburg Ocean Primitive Equation Model. DKRZ Technical Report No. 13, Deutsches KlimaRechenZentrum, Hamburg, Germany, 100 pp., http://www.mad.zmaw.de/Pingo/reports/ReportNo.13.pdf, 1997.

Wolter, K., and Timlin, M.S.: Monitoring ENSO in COADS with a seasonally adjusted principal component index. Proc. of the 17th Climate Diagnostics Workshop, Norman, OK, NOAA/NMC/CAC, NSSL, Oklahoma Clim. Survey, CIMMS and the School of Meteor., Univ. of Oklahoma, 52-57, 1993.

Yeh, S. and Kirtman, B.P.: Tropical Pacific decadal variability and ENSO amplitude modulation in a CGCM, J. Geophys. Res., 109, C11009, doi:10.1029/2004JC002442, 2004.

Chapter 4: Simulating ENSO from LGM to present and beyond: Part I Analysis of Simulated Global Paleoclimate

J. R. Alder[1] and S. W. Hostetler[2]

[1]Oregon State University, Department of Geosciences, Corvallis, OR 97331, United States

[2]US Geological Survey, Oregon State University, Department of Geosciences, Corvallis, OR 97331, United States

4.1 Abstract

A new coupled atmosphere-ocean climate model, GENMOM, is applied to simulate past changes in the strength of the El Niño/Southern Oscillation (ENSO) to help expand our knowledge of both changes in past ENSO and to provide context for future changes. Equilibrium simulations are performed for the LGM (21ka), delgacial (18ka and 15ka), Holocene (12ka, 9ka, 6ka, 3ka), present-day, as well as a doubling (2x) and quadrupling (4x) of atmospheric CO_2. The paleo simulations are forced with time-appropriate changes in insolation, trace gas concentrations, sea level, and ice sheets. The mid-Holocene (6ka) and LGM (21ka) simulations are compared to the best available proxy reconstructions for sea surface temperature, precipitation and net moisture to ensure the simulations are plausible. Surface temperatures in the remaining paleo simulations are compared to new proxy compilations that have reduced spatial coverage but far improved temporal coverage. We find that the model is in good agreement over broad spatial scales, with regional discrepancies between the model and proxy data. Analysis of the simulated tropical Pacific and change in ENSO strength are detailed in Part II of our paper.

4.2 Introduction

Climate for the past 21,000 years is by in large regulated by changes in earth-sun orbital geometry, changes in trace gas concentrations, and the presence and melting of the northern hemisphere ice sheets. Changes in the seasonal distribution of solar radiation (insolation) are controlled by the 22,000-year precession cycle and the 40,000-year tilt cycle (obliquity). The precession cycle regulates the seasonal timing of when the Earth-sun distance is at maximum and minimum, thereby influencing seasonality. The obliquity cycle varies the Earth's axial tilt by ±1.5° from its present angle of ~23.5°, affecting the latitudinal distribution of insolation through time. Atmospheric CO_2 was greatly reduced at the LGM, and generally rises in a stepwise fashion to pre-industrial levels. The LGM was characterized by the Laurentide, Cordilleran, Scandinavian ice sheets in the northern hemisphere, which, due to their height altered atmospheric and oceanic circulation patterns and due to their extent increased the global albedo and thus altered the global energy balance that favored a cooler world.

Past climate has been extensively studied by two international collaborative projects: Climate: Long range Investigation, Mapping, and Prediction (CLIMAP, CLIMAP Project Members, 1981) and Cooperative Holocene Mapping Project (COHMAP, COHMAP Members, 1988). While CLIMAP focused on the LGM, COHMAP concentrated on seven time periods: 18, 15, 12, 9, 6, and 3ka (thousand years ago) and the present-day. Both projects reconstructed past climate using new paleoclimate proxies, developed new techniques for proxy analysis, and used the best climate models available at the time for data-model comparison. Climate models were used to help explain mechanisms that controlled the climate seen in proxy records and to help fill gaps in knowledge when proxy data was sparse. Both CLIMAP and COHMAP provided major contributions to the field of paleoclimatology and modeling, but were conducted in the late 1970's and mid-1980's so are now a bit dated. The Paleoclimate Modelling Intercomparison Project (PMIP) is now active in integrating paleoclimate data models as the present continuation of the CLIMAP and COHMAP projects. PMIP is entering its third phase (PMIP3) using the latest climate models available, some of which not only have dynamic atmosphere, ocean, and vegetation interactions but also include biogeochemical (carbon cycle) models. Mid-Holocene modeling studies consistently show summertime (June, July, August, JJA) positive insolation anomalies due to a change in precession, causing increased northern hemisphere seasonality. The increased land-sea contrast strengthens the Indian summer monsoon, which in turn enhances easterly trade winds from June – September (Kutzbach and Otto-Bleisner, 1982, Braconnot et al., 2007). During this period, proxy reconstructions indicate the El Niño/Southern Oscillation (ENSO) was greatly weakened by as much as 60%. The monsoon enhanced easterly trade winds interact with ENSO dynamics by strengthening windstress, increasing convection, and steepening the east-west Pacific surface temperature gradient, all of which are thought to dampen ENSO strength in the mid-Holocene (Liu et al., 2000).

Here our goal is to explore past changes in ENSO from the LGM to present-day using the new AOGCM, GENMOM. Rather than limiting ourselves to a single mid-Holocene and LGM simulation, we apply the model to simulate the time slices used in both CLIMAP and COHMAP (21, 18, 15, 12, 9, 6, 3, 0ka). Our seven paleosimulations include time-appropriate insolation, atmospheric greenhouse gas concentrations, continental ice sheets, and sea level as boundary conditions. Each simulation is run for 700-years to insure equilibrium conditions with the appropriate boundary conditions and to represent the average climatology for each time period. Part I of our paper focuses on a data-model comparison with our paleo simulations prior to analyzing changes in past and future ENSO in Part II. We compare our simulations with the latest proxy reconstructions used by PMIP for the mid-Holocene and LGM simulations. To evaluate the time periods not covered by PMIP, we apply new proxy compilation datasets with less spatial coverage but better temporal coverage. Our simulation of the past also serves a dual purpose: the Coupled Model Intercomparison Project (CMIP5) in preparing for the upcoming Fifth Assessment Report of the Intergovernmental Panel on Climate Change (IPCC AR5) has deemed that the ability of a climate model to simulate the present climate is not in itself sufficient to judge the quality of models used to simulate the future. To gauge the ability of a climate model to simulate climates significantly different from present, CMIP5 will include simulations for the Last Glacial Maximum (LGM, ~21,000 years ago) and mid-Holocene (~6,000 years ago) to test the model's ability to simulate climate different than today (Taylor et al., 2011). Comparing our LGM and mid-Holocene simulations to both data and other models with provide us with a new method to evaluate the quality of climate simulated by GENMOM.

The paper is organized as follows: in section 4.3 we describe our model GENMOM and the boundary conditions used to force the model. In section 4.4 we perform a data-model comparison for all our paleo time periods using the best available proxy reconstructions. In section 4.5 we conclude our paper with a discussion and summary of our main results. An analysis of the simulation of the tropical Pacific climatology and past and future changes in ENSO is found in Part II of our paper.

4.3 Methods

4.3.1 The model

To perform our simulations of the past and future, we apply the new AOGCM, GENMOM, which combines the atmospheric model GENESIS version 3 (Thompson and Pollard, 1995; Thompson and Pollard, 1997; Pollard and Thompson, 1997) with the ocean model MOM version 2 (Pacanowski, 1996). The nominal AGCM resolution is spectral T31 (3.75° x ~3.75°) with 18 levels. MOM2 is implemented on essentially the same T31 grid and uses 20 fixed-depth levels. A land-surface transfer model (Land Surface eXchange) accounts for the physical effects of vegetation (Pollard and Thompson, 1995). The two models interact in an essentially synchronous manner, communicating every 6 h. A detailed description of GENMOM is presented in Alder et al (2011).

Formal evaluation of the present-day climatology simulated by GENMOM (Alder et al, 2011) indicates that the model captures global circulation patterns. Atmospheric fields such as the jet stream structure and major MSLP features are well simulated. The simulated global 2 m air temperature is 0.6 ºC warmer over oceans and 1.3 ºC colder over land. The model has a warm SST bias (1 – 2.5 ºC) in the Southern Ocean and a subsurface warm temperature bias (exceeding 2 ºC) between 200–1000 m in the tropics and mid-latitudes. Similar to other AOGCMs, GENMOM simulates a weaker-than-observed Atlantic Meridional Overturning Circulation (AMOC): the maximum simulated overturning is 14.5 ± 0.9 Sv, whereas the observed range is 16 - 18 Sv. Also similar to other AOGCMs, GENMOM produces a split ITCZ. An evaluation of ENSO in the GENMOM present-day simulations indicates the model produces a realistic ENSO that is on par with the IPCC AR4 class models by simulating Niño 3 - 4 indices that have a standard deviation within 0.3 °C of the observations, a realistic frequency (5.6 year period), and generally correct spatial patterns of temperature and precipitation teleconnections (Alder et al., *in prep*).

GENMOM is applied to simulate seven paleo time slices (21ka, 18ka, 15ka, 12ka, 9ka, 6ka, and 3ka), present-day, and two CO_2 sensitivity simulations (2x and 4x atmospheric CO_2) for a total of ten equilibrium simulations. The paleo simulations are forced with the appropriate changes in sea level, ice sheets, insolation and trace gas concentrations, while the CO_2 sensitivity simulations only alter atmospheric CO_2. Each of the ten simulations is run for 700-years, discarding the first 400-years as spin up, leaving 300-years for our analysis.

4.3.2 Boundary conditions

In order to simulate climates of the past with reasonable quality, forcing the model with realistic boundary conditions is vital. Unlike other mid-Holocene modeling studies (Otto-Bliesner et al., 2003), we force each simulation with changes in insolation (Berger, 1978), topography, bathymetry, ice sheet height and extent, atmospheric CO_2, CH_4, and N_2O. Vegetation is kept at modern distributions for all simulations because global vegetation patterns at each time slice are not well constrained. For orographic changes and changes in ice sheets, we make use of the ICE-4G model reconstruction (Peltier, 2002). Anomalies between each time slice and the ICE-4G 0ka orography are interpolated from 1°×1° degree resolution to our T31 grid and applied to present-day Scripps orography (Gates and Nelson, 1975). At T31 resolution, the Bering Strait is closed and is allowed to remain so through all our simulations. Forcing the Bering Strait to be open weakens the GENMOM present-day global ocean overturning, which is already found to be weaker than observed (Alder, 2011). The Strait of Gibraltar is also closed, leaving the Mediterranean isolated from the main ocean.

Our derived land masks (Fig. 4.1) include ice sheet height and extent, as well as isostatic effects caused by the depression of ice sheets and rebound once the ice sheets are removed. Our land masks also include forebulging where much of the northern high latitude bathymetry is raised in response to the crustal depression under the ice sheets. Eustatic sea level lowering from reduced ocean volume is accomplished by a datum shift to the new sea level, such that all land topography is increased accordingly. Shallow ocean grid cells can become exposed to form new land grid cells (ie Indonesia, Papua New Guinea and much of northern Europe and Asia). MOM2 uses a fixed depth grid, so bathymetry is only changed if the datum shift forces the grid cell to the next depth level, which leaves mid and deep ocean cells unaltered because the change in sea level is less than the grid cell height.

The Laurentide, Cordilleran, Scandinavian, and Patagonian ice sheets are easily identified in our land masks, as are their subsequent ablation through the Holocene. Changes to ice sheet height are also implicitly made to both Greenland and Antarctica. The paleo Lake Agassiz formed after glacial melt is simulated in the 9ka and 6ka time slices, but is represented as an expansion of the Hudson Bay, which is not unexpected at T31 resolution. The ICE-4G dataset includes an Eastern Siberian Ice Sheet, which is included in the GENMOM land masks at 21ka and 18ka, though more recent evidence suggests that this ice sheet did no exist (Sher, 1995; Felzer, 2001).

Insolation changes between LGM and present are largely dominated by the precessional cycle, which shifts peak insolation (perihelion) from the Northern Hemisphere winter to the summer. The changes in top of atmosphere (TOA) insolation across our time slices are shown in Fig. 4.2. The 9ka simulation shows a large reduction

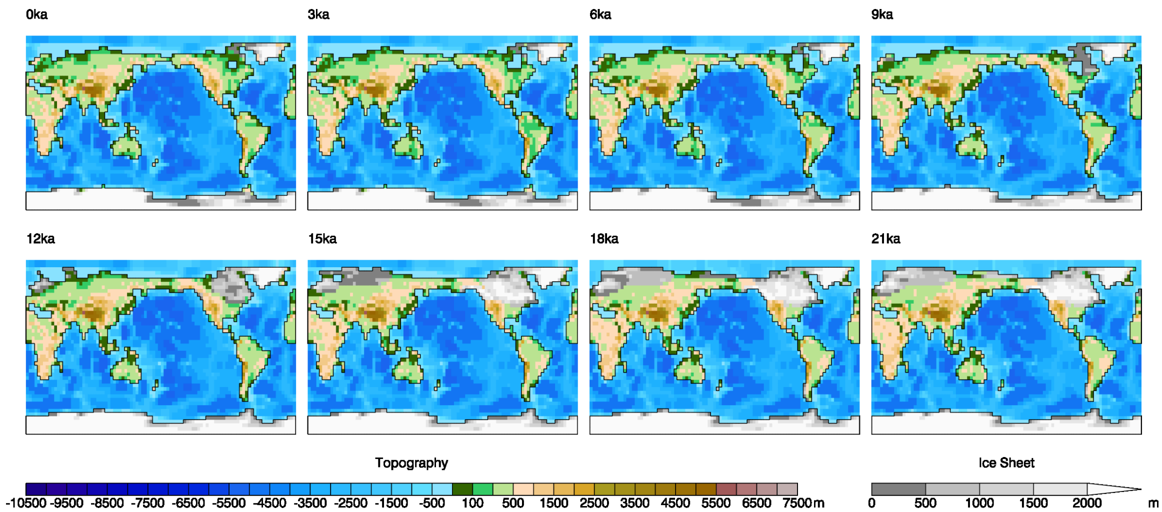

Figure 4.1 ICE-4G derived orography with ice sheet height and extent.

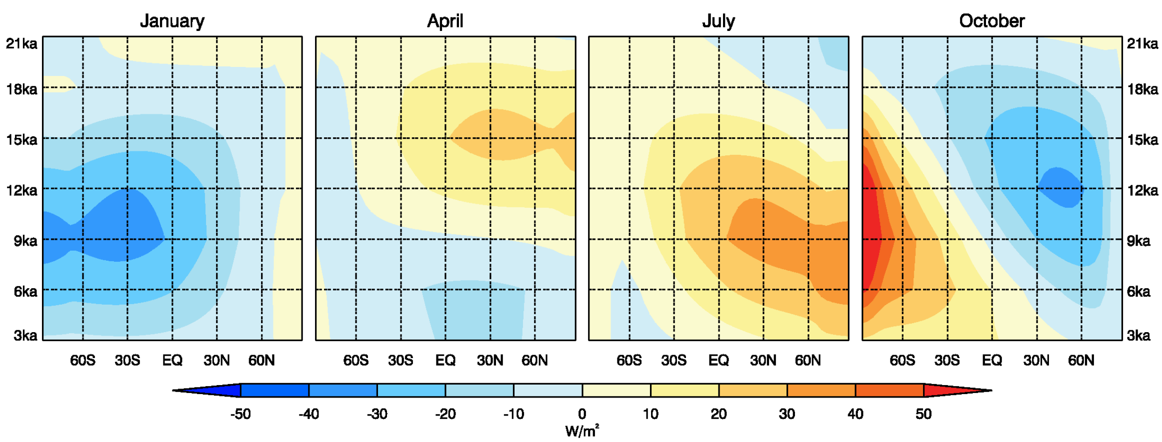

Figure 4.2 Changes in top of atmosphere (TOA) insolation from the 0ka simulation.

in Southern Hemisphere insolation during January, whereas the Northern Hemisphere has an increase in insolation during July. A reduction in Southern Hemisphere winter insolation, and subsequent increase in Northern Hemisphere summer, between 15ka and 3ka, is the expected pattern of the precession of perihelion.

In addition to changes in land mask configuration and insolation, past trace gas concentrations are applied as boundary conditions (Table 4.1). Trace gas concentrations used in the model are estimated from ice core records by using a ± 300 yr averaging window around our time slice so that concentrations represent average conditions. The 0ka simulation is forced with 1995 trace gas concentrations, so that it is neither pre-industrial nor true 0 years BP (1950), but is considered to be a present-day simulation. As in Alder et al. (2011, *in prep*), the 2x and 4x simulations double (710 ppmV) and quadruple (1420 ppmV) atmospheric CO_2 only, leaving CH_4 and N_2O at their 1995 concentrations.

4.3.3 Proxy reconstructions

A key aspect to using numerical climate models is being able to validate the model output against observations, so that confidence can be built that the model is capturing the dynamics needed to produce a realistic climate. In the present, this is relatively easy as model output can be compared to real world observed data. The issue becomes more complex when observations are sparse. Fields such as temperature, precipitation, cloud cover, longwave and shortwave flux, and land cover are readily available from satellite observations; although, those records are relatively short and only extend to the late 1970s when satellite observations began. Other fields such as snow depth and soil moisture are not well constrained even with the use of satellites. When

Table 4.1 Atmospheric trace gas concentrations used in each simulation time slice. 21ka to 3ka values are estimated from ice core records by averaging the gas concentration with a ± 300 yr averaging window (CO_2 from Monnin et al., 2001, CH_4 from Brook et al. 2000, N_2O from Sowers et al. 2003).

	CO_2 (ppmV)	CH_4 (ppbV)	N_2O (ppbV)
4x	1420	1714	311
2x	710	1714	311
0ka	355	1714	311
3ka	275	627	264
6ka	260	596	227
9ka	260	677	244
12ka	240	500	246
15ka	220	500	216
18ka	188	382	219
21ka	188	392	199

longer records are needed that satellites cannot provide we must fall back solely to instrumental observations that are taken at particular locations and times. Products such as the HadISST v1 dataset provide a long record of sea surface temperatures from station data, buoys, and onboard ship measurements that span back to the 1880s (UK Meteorological Office, 2006). However, building a global dataset from sparse point data has its own limitations. In many cases, very long qualitatively measured observations exist such as crop yields in Europe or the flooding cycle of the Nile River. While these records may extend many hundreds if not thousands of years, they are spatially limited to only a few locations and can only be applied to those locations.

When reconstructing climates of the more distant past, climate archives such as pollen records, ice cores, tree rings, and ocean sediments can be used as proxies for fields such as temperature and moisture, thereby extending climate records well beyond the instrumental record. Ice cores, for example, provide a wealth of information ranging from trace gas concentrations to temperature and the frequency of volcanic eruptions (Brook et al., 2000). There are many forms of paleothermometers that can be used to reconstruct past temperatures. Ocean sediments can be cored and examined to determine the ratio of Magnesium to Calcium (Mg/Ca) in the shells of planktic or benthic foraminifera, which can then be used to infer past temperatures. Pollen assemblages found in lakes can be used to determine past changes in plant species distributions. By assuming that plant physiology was essentially the same in the past as it is today, pollen records can be used to infer changes in temperature, moisture, and growing degree days (Bartlein et al., 2010) by constructing analogues to modern plant distributions. Changes in the extent of closed basin lakes can be utilized to infer changes in the moisture balance of the surrounding basin and hence region. Although many of these proxy records are both spatially and temporally sparse, taken together they can be leveraged to evaluate the quality of our paleo climate simulations. We utilize the best and most current proxy reconstructions to evaluate how well our model simulations reflect reconstructed climates of the past.

4.4 Data-model comparison

We compare our GENMOM paleo time slice simulations to available proxy reconstructions to determine if the model can produce plausible LGM, deglacial and Holocene climates. The PMIP project uses LGM simulations as to test models during time periods with large, well defined, northern hemisphere ice sheets and a mid-Holocene simulations to test the model response to known changes in seasonal insolation (ie precession). Although we seek to evaluate all our paleo time slices, proxy reconstructions tend to focus on the LGM and mid-Holocene, leaving us with sparse data to evaluate the intervening periods. Proxy records such as ice cores have excellent temporal coverage, but very poor spatial coverage at essentially one point in space. At the other end of the spectrum, marine sediment based reconstruction datasets can have excellent spatial coverage (near global), but are only available for a few time periods (ie LGM and mid-Holocene). We make use of both types of records to evaluate our model time slices, but also include new proxy compilations from Shakun et al. (*in prep*) and Marcott et al. (*unpublished*) that balance reasonable spatial coverage with excellent temporal coverage.

4.4.1 Temperature

To evaluate the simulated large-scale changes in temperature, we compare GENMOM to ice core isotope records at the North and South Poles (Fig. 4.3). The GENMOM temperature is taken from essentially the same location as the real world ice core sites. For Greenland we use the NGRIP $\partial^{18}O$ oxygen isotope record (NGRIP dating group, 2008) and for Antarctica we use ∂D hydrogen isotope from EPICA Dome C (Jouzel et al., 2007). Both records measure the ratio of the rare isotope (deuterium and ^{18}O) to their much more abundant counterparts (hydrogen and ^{16}O). The difference between these ratios can be used as a paleothermometer. It should be noted that both isotopic ratios are not strictly a reflection of temperature only, but can also be influenced by changes in moisture. We assume these records primarily reflect changes in temperature.

GENMOM captures the overall warming trend from glacial to interglacial but does not capture finer features such as abrupt climate changes (ie Younger Dryas) seen in the ice core records (Fig. 4.3). GENMOM captures the Antarctic warming between 18ka and 15ka, although the warming is not as rapid as the observations indicate, the warming is greater in Antarctica than in Greenland for this period. GENMOM shows a much more gradual Greenland warming between 15ka and 9ka, however 12ka in the ice core is at the onset of a rapid climate change event (the end of the Younger Dryas). If the 12ka boundary conditions for trace gas concentrations and land mask configuration were ~500 years too young, the simulation would be further into the transition, as it appears to be in Fig. 4.3. GENMOM does not exhibit much, if any, sign of a Holocene 'climatic optimum' between 9ka and 6ka with a gradual cooling to 0ka.

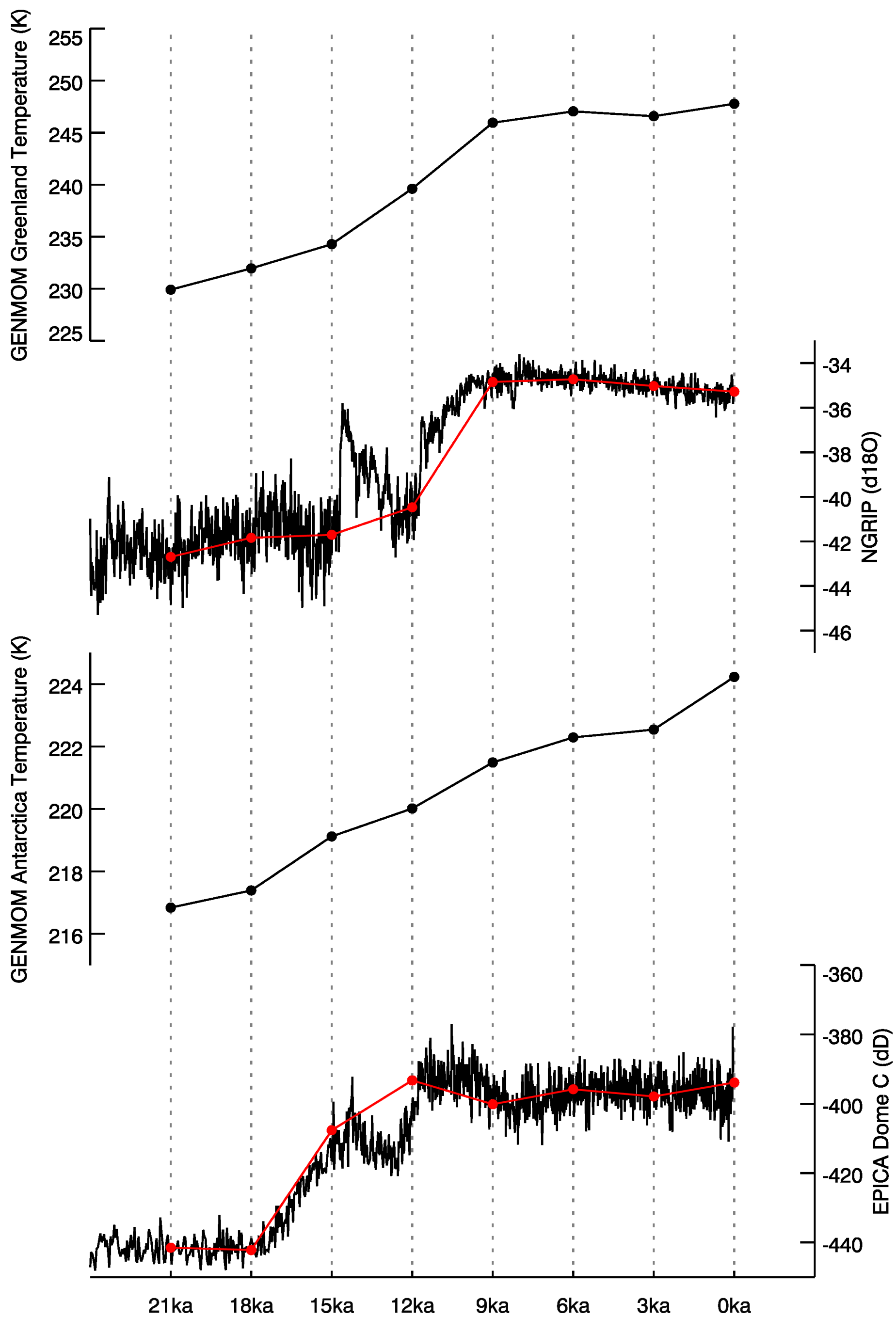

Figure 4.3 GENMOM simulated temperature changes from 21ka to present for both Greenland and Antarctica (a. and c.) along with isotopic proxy reconstruction from ice cores (b. and d.). The Greenland ice core comes from NGRIP (NGRIP dating group, 2008). The Antarctic ice core comes from EPICA Dome C (Jouzel et al., 2007). The GENMOM temperature time series are taken from the single grid cell that each ice core is located in. Also note the GENMOM 0ka is essentially 1995, the NGRIP data is from 2000 while the Dome C data is from 1950. A ±300-year average of each ice core record is plotted in red to compare the high-resolution data to the coarse GENMOM time slices.

Instead, GENMOM has a warming to 0ka, which may be attributed to our 0ka simulation actually being present-day rather than pre-industrial. A pre-industrial simulation may have reflected the observed cooling. In Antarctica during the mid to late Holocene, GENMOM simulates a gradual warming towards 0ka rather than the stabilization at 9ka – 6ka levels as seen in the Dome C record.

Fig. 4.4 compares GENMOM SST anomalies for the mid-Holocene (6ka) and LGM (21ka) versus the GHOST (Leduc et al., 2010) and MARGO (MARGO Project Members, 2009) reconstruction datasets. The MARGO dataset is the most complete spatial reconstruction used in our analysis with nearly 700 data points. MARGO uses paleothermometers in the form of microfossil-based transfer functions (planktonic foraminifera, diatom, dinoflagellate cyst and radiolarian abundances) and geochemical (alkenones and planktonic foraminifera Mg/Ca) analysis. The GHOST dataset also uses alkenones and foraminifera Mg/Ca, but is much sparser with ~100 data points.

The simulated 6ka SST anomalies compare well to GHOST on the western coast of North and Central America. GENMOM matches the cluster of data points off the coast of Ecuador well, though there is one anomalous 1 °C warm record that stands apart from the other points. The large positive anomalies along the coast of Chile are not simulated, nor are any positive SST anomalies in that region. The GHOST dataset has many positive anomalies in the Atlantic that GENMOM compare well to, where the model displays cooling in the Atlantic at 6ka and the data generally indicate a warming. GENMOM does simulate a warming in the Norwegian Sea, likely due to an insolation driven sea-ice reduction. However, the warming is far below the 2°C anomalies in the GHOST data. The simulated 6ka Mediterranean has a ~1°C anomaly, which is at odds

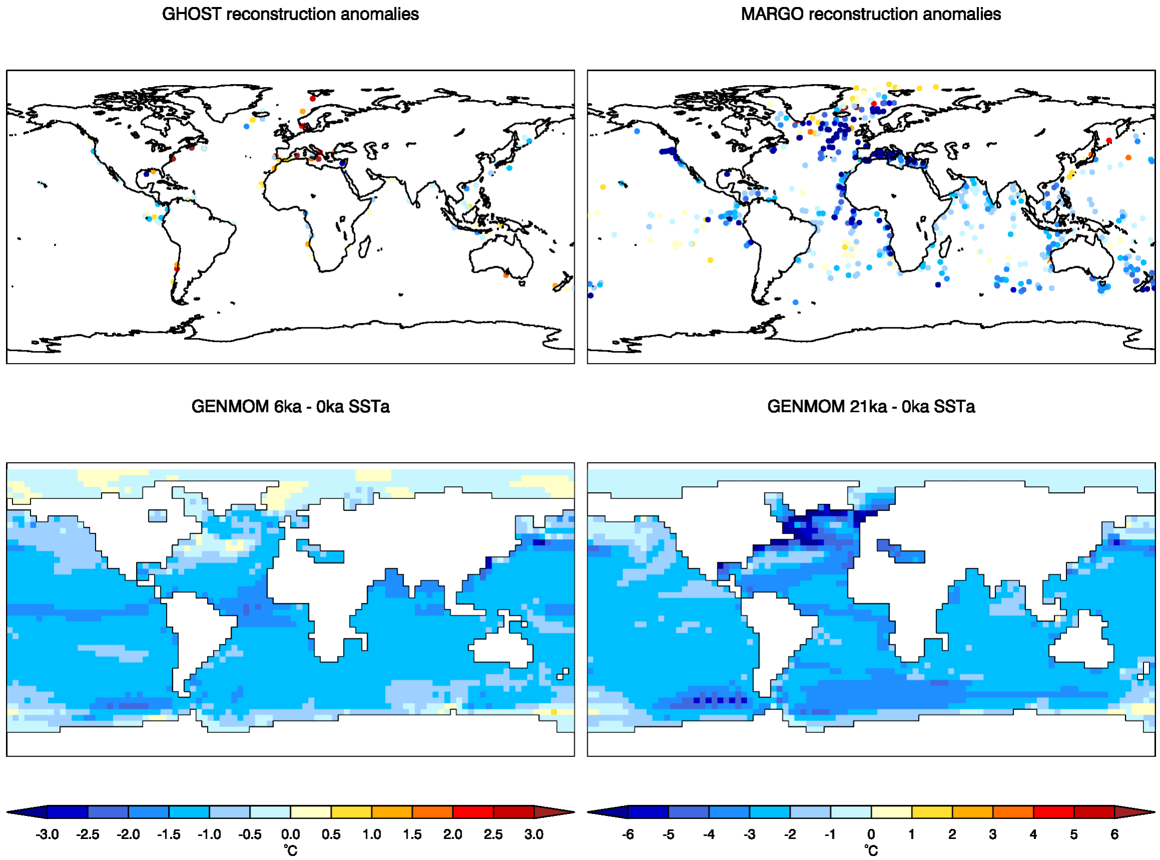

Figure 4.4 GENMOM sea surface temperature anomalies from 0ka compared to the mid-Holocene GHOST dataset (Leduc et al., 2010) and the LGM MARGO dataset (MARGO Project Members, 2009).

with the reconstruction that indicate strong warming. The eastern coastline of Asia is well simulated; however the reconstruction of the warm pool region of Indonesia and the Philippines have a warming whereas GENMOM indicate up to -1.5 °C cooling. Likewise, GENMOM does not simulate a warming on the southern coast of Australia or near New Zealand. In general, GENMOM has greater than 1 °C cooling in much of the mid and tropical latitudes, and weak warming at some polar latitudes where sea ice plays a strong role. Globally, the GHOST dataset indicates a mix of both regional warming and cooling, but the data point coverage are predominantly coastal with no open ocean data.

The MARGO reconstruction provides a much more comprehensive dataset than GHOST, with global coverage that is not confined to the coastlines. The GENMOM 21ka simulation compares well to MARGO over much of the Pacific. GENMOM does not simulate the strong negative anomalies along the western coast of the United States; perhaps these anomalies are caused by changes in the California Current, which GENMOM does not resolve (Alder et al., 2011). The MARGO reconstruction shows a mix of positive and negative anomalies in the Pacific basin, most of these anomalies are small regardless of sign, indicating GENMOM is too cold despite the ambiguity in the observed record. The MARGO dataset exhibits stronger cooling in the far eastern Pacific off the coast of Ecuador with less cooling in the central Pacific. GENMOM does not simulate this uneven cooling, but rather has consistent cooling along the entire equatorial Pacific. The GENMOM LGM anomalies in the Atlantic are similar to those of MARGO, with perhaps somewhat too weak cooling in the equatorial Atlantic. The MARGO reconstructions of the far north Atlantic are somewhat contradictory, with strong positive anomalies adjacent to strong negative anomalies. Anomalies greater than 1 °C in the Arctic Circle imply warming relative to present-day, when sea-ice was surely more extensive. Unlike the GHOST dataset, the MARGO reconstruction indicates the Mediterranean as much cooler; GENMOM does simulate this but not to the same degree as the proxies. The Indian Ocean and eastern Pacific are generally in good agreement, where GENMOM is perhaps 0.5 °C too cold.

In order to evaluate the simulated surface temperature anomalies we use the proxy compilations of Shakun et al. (*in prep*) for the deglacial and Marcott et al. (*unpublished*) for the mid to late Holocene. Both of these compilations take existing published proxy records with accurate dating control and apply them to a common chronology and temporal resolution. Compared to MARGO, these proxy compilations sacrifice spatial coverage (~70 – 80 data points each), but span more time periods. To apply these proxy time series to our respective simulations, we take a ±500-year average around each GENMOM time slice, so that each point is representative of the mean temperature for those millennia. Since both proxy compilations cover such a long period of time, but many records do not span to 0ka, all anomalies are taken from a 9ka mean (9.5ka – 8.5ka) rather than to present-day.

Compared to the proxy reconstructions at 21ka, the GENMOM anomalies are well simulated in the Pacific where the proxies indicate the model may be slightly too warm near Japan, Indonesia, and the Philippines relative to 9ka (Fig. 4.5). Anomalies in the Atlantic and Gulf of Mexico are well simulated, however the southern hemisphere mid latitude Atlantic is too warm in GENMOM. The southern Australia and New Zealand records also indicate GENMOM is too warm in the Southern Ocean. Similar to

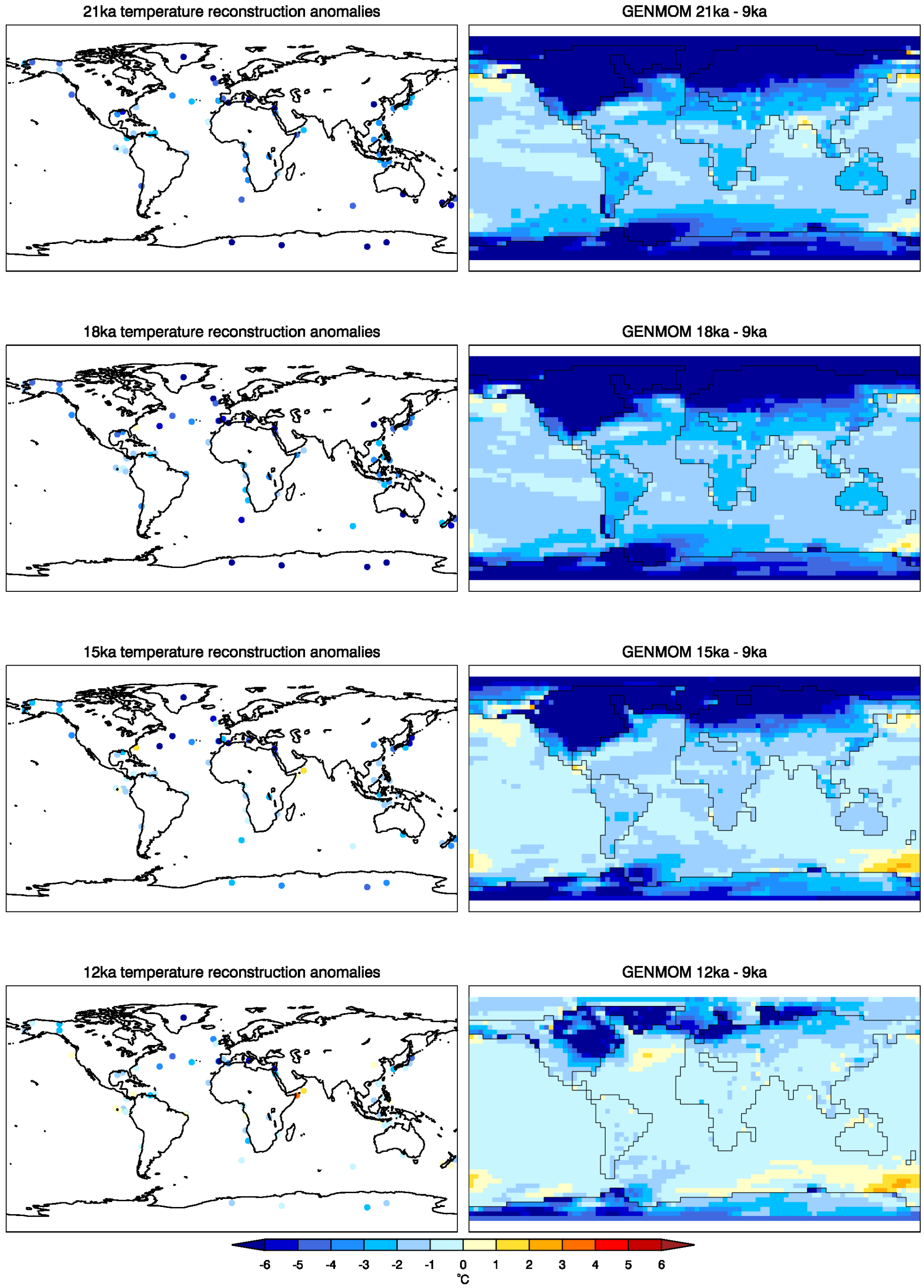

Figure 4.5 GENMOM 2 m air temperature anomalies (right) from 9ka compared to the proxy compilation of Shakun et al. (*in prep*) for the deglacial period (left). Each record is averaged using a ±500-year window around each GENMOM time slice, to represent mean conditions for those millennia.

MARGO, the proxy records indicate the Mediterranean as much cooler, whereas GENMOM does not fully capture this cooling. The proxy and GENMOM anomalies at 18ka are by and large similar to those of 21ka.

At 15ka and 12ka the large Northern Hemisphere ice sheets had retreated substantially and the seasonal timing of insolation had shifted. In both 15ka and 12ka simulations the Gulf of Mexico and Ecuadorian proxies match well to the simulations. The North Atlantic warmed relative to 21ka, but GENMOM is ~2 °C warmer than the proxies indicate. During both 15ka and 12ka, the Southern Ocean warmed relative to 21ka, which GENMOM captures well, with the exception of the New Zealand proxies at 15ka. GENMOM compares well to the Indonesian and the Philippines anomalies, yet the proxy records surrounding Japan indicate that GENMOM is too warm in this region.

At both 6ka and 3ka GENMOM simulates strong warming at high latitudes in both hemispheres relative to 9ka (Fig. 4.6). As mentioned previously, the GENMOM 6ka and 3ka polar temperatures continue to increase, whereas ice core records indicate a stabilization and even mild cooling (Fig. 4.3). The 6ka and 3ka proxy records show a mix of positive and negative anomalies relative to 9ka, whereas GENMOM predominately shows warming. The eastern coast of the United States and the Gulf of Mexico show a mild to strong cooling, whereas GENMOM indicates mild to strong warming. The high latitude northern Atlantic records show the same data-model discrepancy. Proxies in Southeast Asia indicate a mix of positive and negative anomalies, where GENMOM consistently has 0 – 1 °C warm anomalies.

While comparing model results to proxies provides an important metric of model quality compared to observations, the sparse annual proxy data do not present a complete

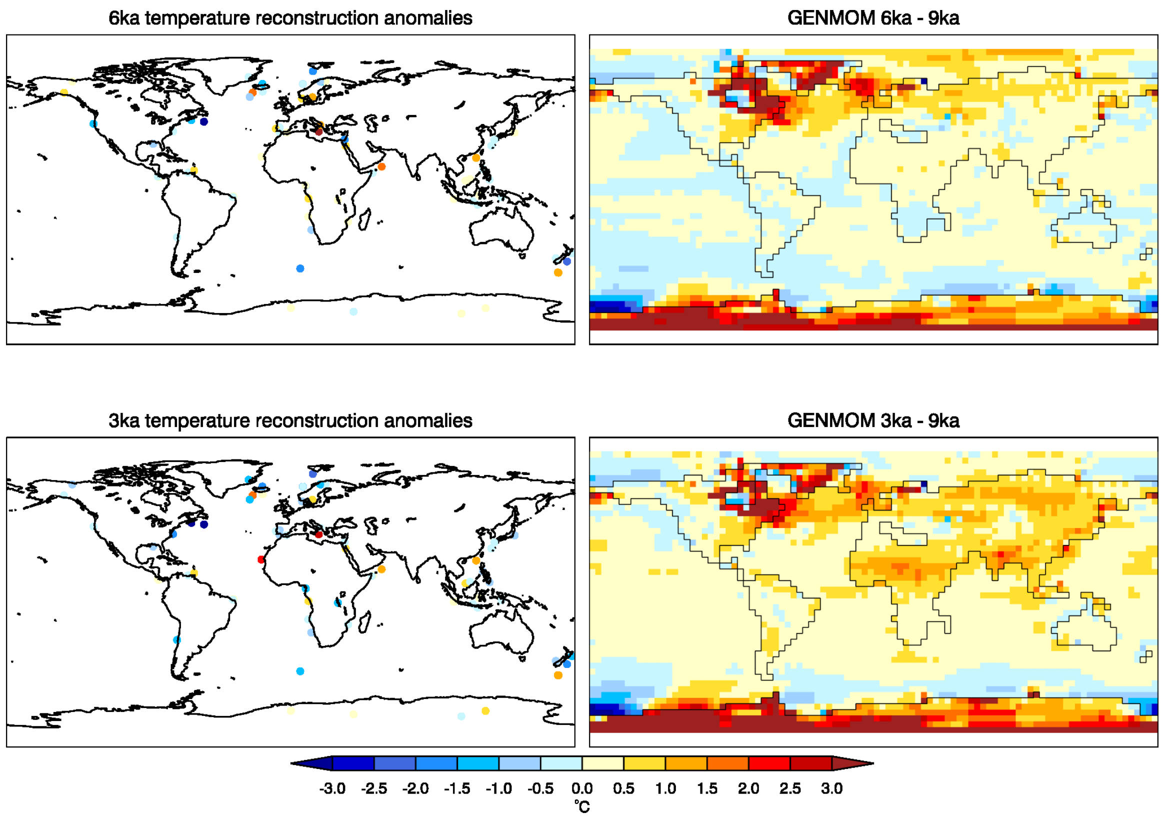

Figure 4.6 GENMOM 2 m air temperature anomalies (right) from 9ka compared to the proxy compilation of Marcott et al. (*unpublished*) for the mid to late Holocene (left). Each record is averaged using a ±500-year window around each GENMOM time slice, to represent mean conditions for those millennia.

picture of past temperatures that include possible changes in seasonality. Model to model anomalies clearly show the influence of precession on insolation, where mid-Holocene northern hemisphere winter is significantly colder than present over the large northern hemisphere landmasses, due to a wintertime deficit in insolation (Fig. 4.7). Unlike other mid-Holocene simulations that test precessional changes only (Otto-Bliesner et al., 2003), our 6ka simulation includes a 95 ppmV reduction in atmospheric CO_2 with a corresponding ~1.5 °C decrease in global temperature. At 12ka, winter temperatures over the northern hemisphere continents are reduced by greater than 6 °C and cool further in the 21ka to 15ka simulations. The northern hemisphere Holocene had a wintertime deficit in insolation relative to today, however, due to a precessional shift, summertime correspondingly had a net positive anomaly. The 12ka – 6ka simulations all show strong summertime warm anomalies over the Eurasian landmass, despite reduced greenhouse gases (Fig. 4.8). The 21ka - 15ka simulations each exhibit larger than 6 °C cold anomalies over the Laurentide, Cordilleran, Scandinavian ice sheets during summer demonstrating the local and regional impact of the ice sheets. At 21ka insolation was similar to present, yet the combined effect of albedo from massive northern hemisphere ice sheets and lower greenhouse gases resulted in a ~6.8 °C global cooling annually (~9.8 °C cooling over land, ~5.2 °C cooling over the oceans).

4.4.2 Precipitation

While paleothemometers available in climate archives can be used to reconstruct past temperature, past changes in precipitation can be quantitatively inferred from spatial changes in pollen. Modern plant taxa ranges are defined by bioclimatic envelopes derived from associating the observed distribution with a combination of climatic

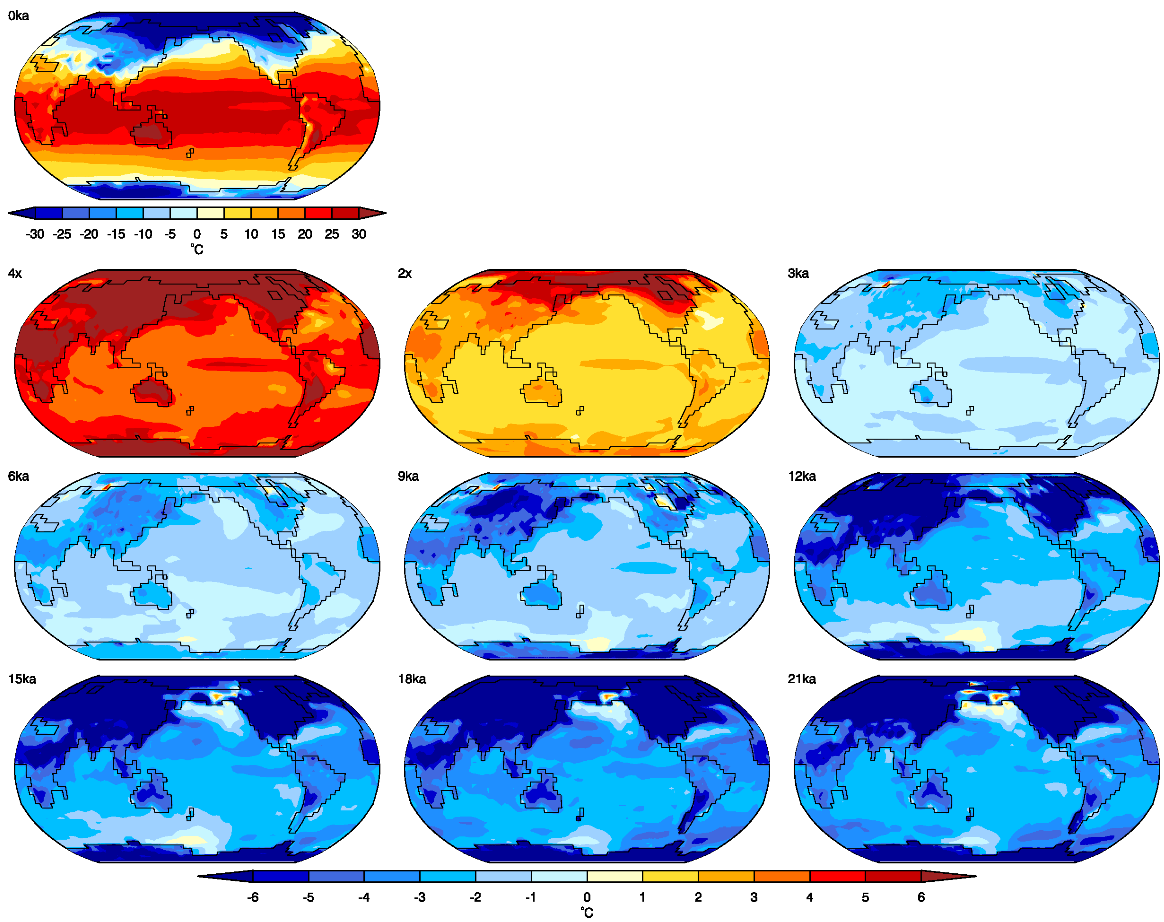

Figure 4.7 GENMOM December, January, February (DJF) 2 m air temperature anomalies from 0ka.

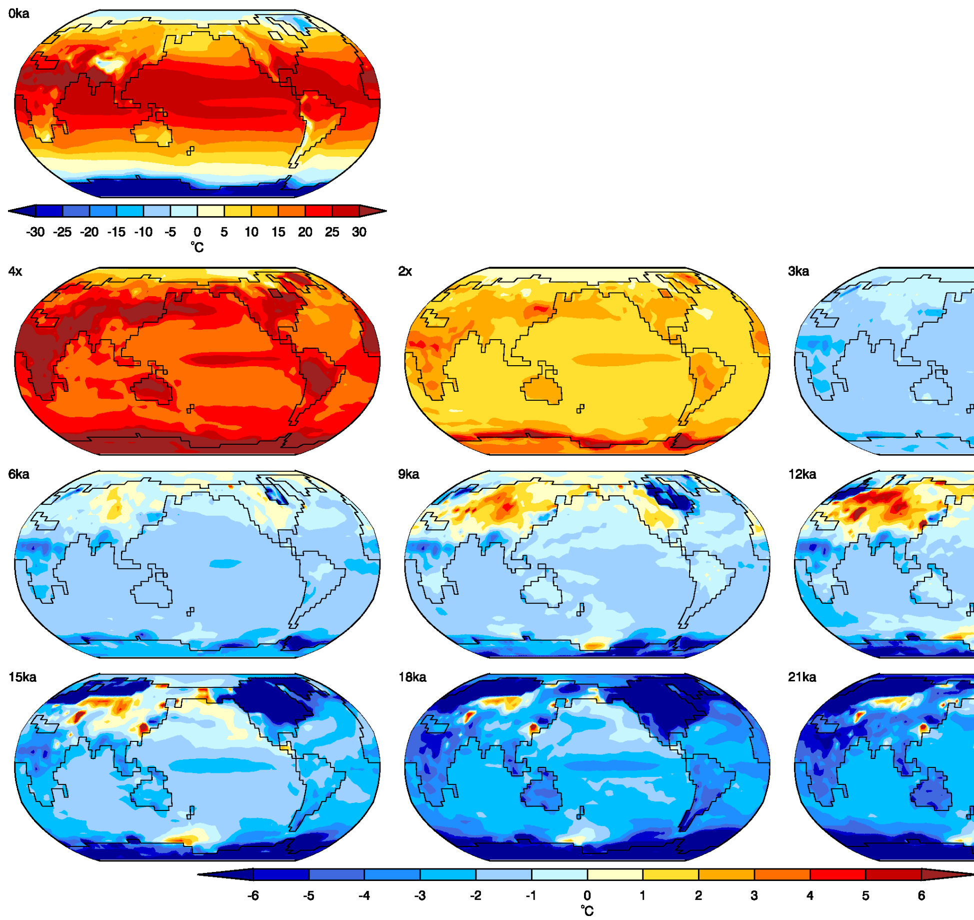

Figure 4.8 GENMOM June, July, August (JJA) 2 m air temperature anomalies from 0ka.

parameters such as mean annual temperature, precipitation, growing-degree days and the number of freezing days. The bioclimatic envelopes can then be used to develop a relationship between climatic parameters and species distributions. Fossil pollen records provide insight into how plant distributions changed in the past, and by inference, how the climatic envelopes must have been altered to support those changes in plant distributions. A variety of statistical methods (inverse regression, weighted average, artificial neural networks, modern analogue, response surface, and inversion of species envelope models) are available to qualitatively infer climate from pollen distributions, however each has its own strengths and limitations (Bartlein et al., 2010).

We use the fossil pollen reconstruction of Bartlein et al (2010) for the mid-Holocene and LGM to evaluate changes in mean annual precipitation (MAP) in our 6ka and 21ka simulations (Fig. 4.9). The mid-Holocene pollen reconstructions indicate the western United States was wetter-than-present, while the east was predominantly drier. Much of Africa, Europe and Asia were considerably wetter-than-present. Exceptions to these generalizations are a localized drying in Scandinavia and a drying in southeast Africa, including Madagascar. GENMOM captures the eastern United States drying at 6ka, but simulates drying in the west in contrast to the records indicating wetter-than-present conditions. GENMOM simulates the mid-Holocene wet African conditions well, with perhaps too much drying in the southeast region. The mid-Holocene simulations indicate pervasive drying over northern Europe, northern Asia and China, where the proxies exhibit coherently wetter conditions. In agreement with the pollen records, GENMOM simulates increased precipitation in northeast China and Mongolia during the mid-Holocene.

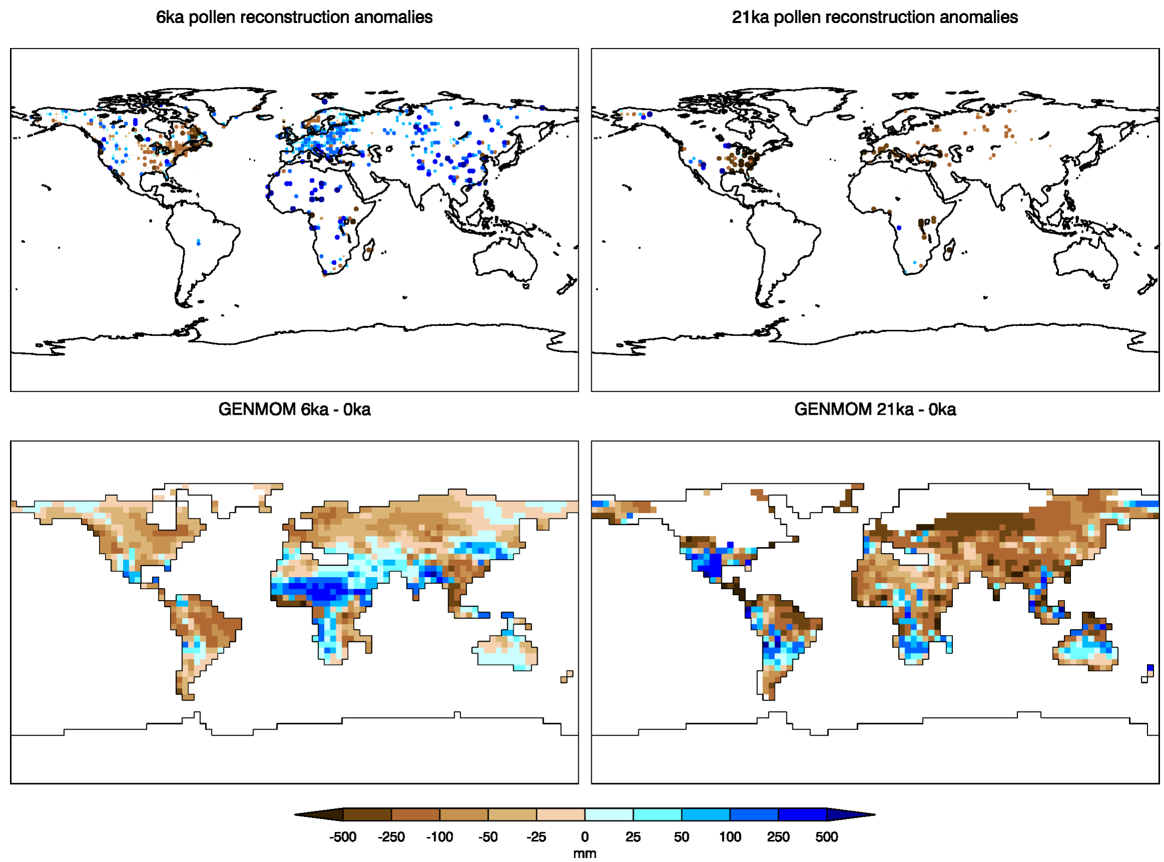

Figure 4.9 Reconstructed changes in mean annual precipitation (MAP) from pollen assemblages (Bartlein et al., 2010) for the mid-Holocene and LGM compared to GENMOM simulated annual precipitation anomalies for the same time slices relative to the 0ka simulation.

The GENMOM 21ka simulation is in better agreement with pollen records than the 6ka simulation. GENMOM captures both increased precipitation in the southwest United States and drying in the east. The simulation has drying over much of Alaska, which is not in agreement with two records that indicate a strong increase in precipitation. The simulated widespread drying over Europe and Asia agrees well with the pollen records. The 21ka simulation has drying along equatorial Africa and a slight increase in precipitation over South Africa. These patterns compare well to the proxy records, however GENMOM has increased precipitation over Madagascar whereas one pollen record indicates strong drying.

During the mid-Holocene, the precessional cycle shifts annual peak insolation from northern hemisphere winter in present-day to summer during the Holocene. This change in the seasonal timing of insolation enhances the temperature contrast between winter and summer. The strengthened summertime (JJA) warming of northern hemisphere continents enhances seasonal monsoons, which are driven by the contrast in land and ocean temperatures. The 15ka – 6ka simulations have a strengthened African and Indian summer monsoons, driven by the seasonal shift in peak insolation (Fig. 4.11). As previously mentioned, the enhanced North Africa and Indian precipitation corroborates well with the mid-Holocene pollen reconstructions. The GENMOM simulation of enhanced monsoons corroborates with previous mid-Holocene modeling studies (Kutzbach and Otto-Bleisner, 1982, Braconnot et al., 2007). The 21ka – 12ka simulations have increased precipitation over Mexico and the southwest United States, which is perhaps less due to a strengthened monsoon (as the 21ka precessional cycle is similar to present-day), but rather a shift in the summer position of the subtropical jet

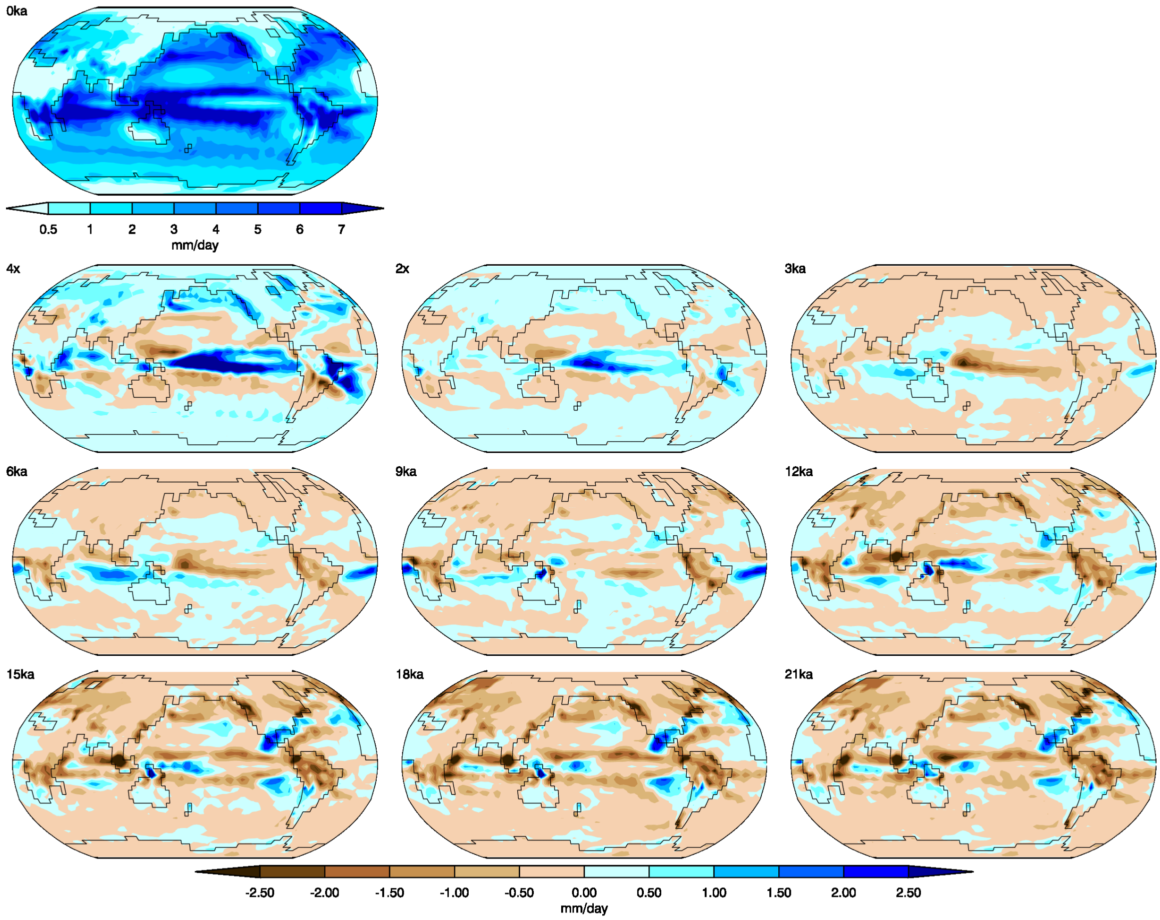

Figure 4.10 GENMOM December, January, February (DJF) precipitation anomalies from 0ka.

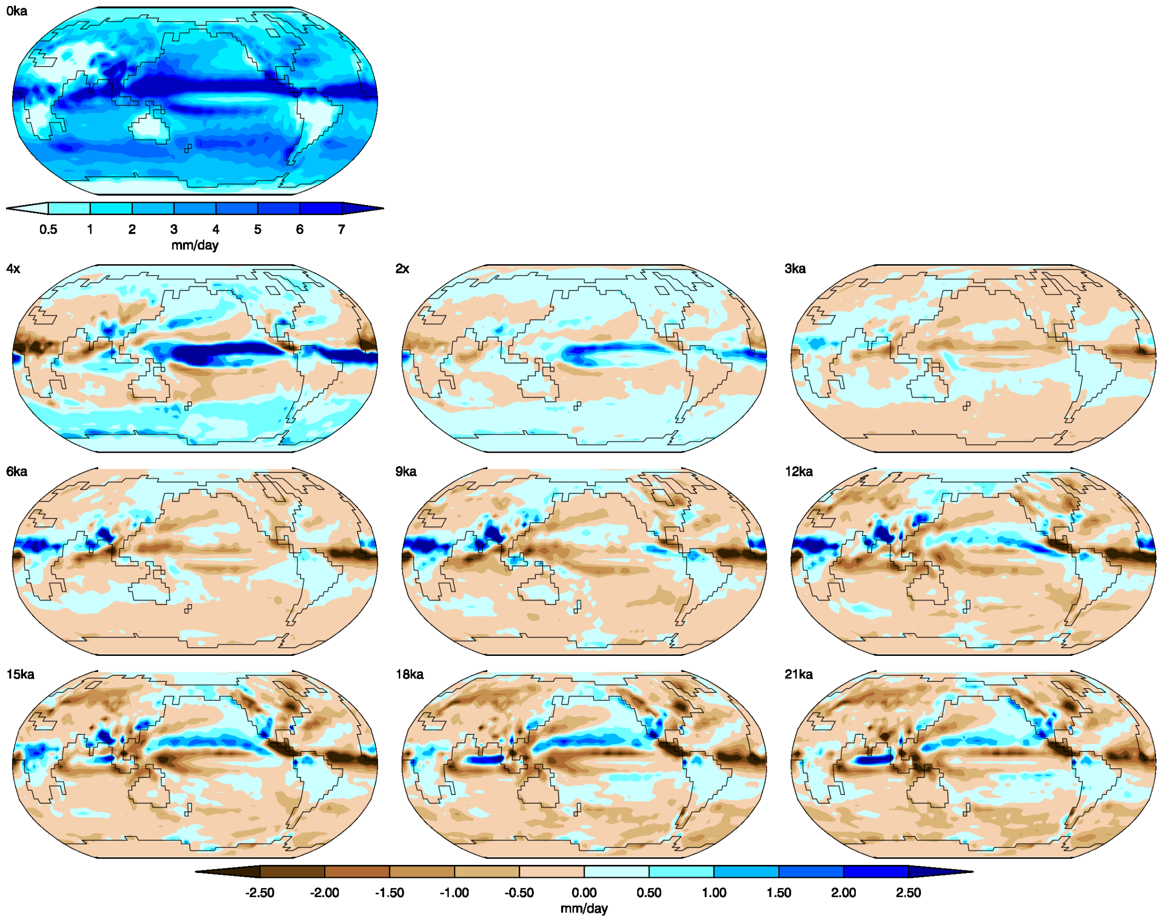

Figure 4.11 GENMOM June, July, August (JJA) precipitation anomalies from 0ka.

stream. The strong drying in Central America between 21ka and 12ka support the hypothesis of a shifted subtropical jet stream. Likewise, the LGM pollen records indicate increased precipitation in the southwest United States. During winter (DJF) between 21ka and 15ka, much of Mexico is simulated to have strongly increased precipitation (Fig. 4.10), which indicates the Central American drying is limited to summertime (JJA).

4.4.3 Net moisture

In addition to reconstructed temperature and precipitation, we would also like to have information on how the net moisture balance changed in the past to evaluate our paleo simulations. Net moisture (precipitation minus evaporation, P-E) can be inferred from geological evidence for changes in height and extent (collectively know as status) of lakes in the past. Closed basin lakes respond to changes in net moisture in a relatively straightforward and well-understood way. Over some time period, closed basin lakes attain equilibrium with their inputs (streamflow and precipitation) and their outputs (evaporation from the lake surface). If a region becomes drier, lake volume is lost, resulting in a reduction of height and extent (status). In overflowing lakes, changes in status can be determined by the change in discharge. The Global Lake Status Data Base (GLSDB, Kohfeld and Harrison, 2000; Harrison et al., 2003; Yu et al., 2001) records the status of present and past lakes by using three values of status (high, intermediate, and low). Taking anomalies between the past and present lake level status produces five broad categories of change: much wetter than present, wetter than present, no change, drier than present, much drier than present.

We use changes in lake status from the GLSDB from the mid Holocene and LGM to present to compare to GENMOM simulated P-E anomalies between 6ka – 0ka and

21ka - 0ka (Fig. 4.12). The 6ka reconstructed lake status for North America is primarily a mix of reduced and no change, with only a few locations indicating increased lake volume. GENMOM generally captures this pattern with a mix of little change and a few regions of reduced net moisture. South America has a similarly mixed reconstruction that GENMOM generally matches. The lake status data for the western coast of South America indicate contradictory information, where regions of reduced lake volume are directly adjacent to regions with increases in volume. In these locations, GENMOM simulates reduced net moisture. Mid-Holocene northern Africa is particularly interesting because past evidence of ecological and biological changes indicate that regions that are now arid desert were lush savanna at the time (known as Green Sahara). The GLSDB data clearly support this hypothesis with increased lake status across the northern portion of the continent. In corroboration with the simulated 6ka precipitation, GENMOM shows strongly increased net moisture, but, similar to nearly all mid-Holocene model experiments, the wetting is confined to the equatorial region and does not expand as far north as the lake status records indicate is should. Northern Europe and Asia are characterized by either larger lakes or no change, with only a few isolated records indicating lower lake status. As in the precipitation anomalies, GENMOM simulates less precipitation and correspondingly reduced P-E in these regions at 6ka, which is in conflict with the lake status records. GENMOM does simulate increased net moisture in the Indian subcontinent, in agreement with the lake records.

At 21ka, the GENMOM simulation has increased net moisture in the southwestern United States and Mexico, and reduced P-E in Central America, both of which compare well to the lake status records. The combination of southwestern United

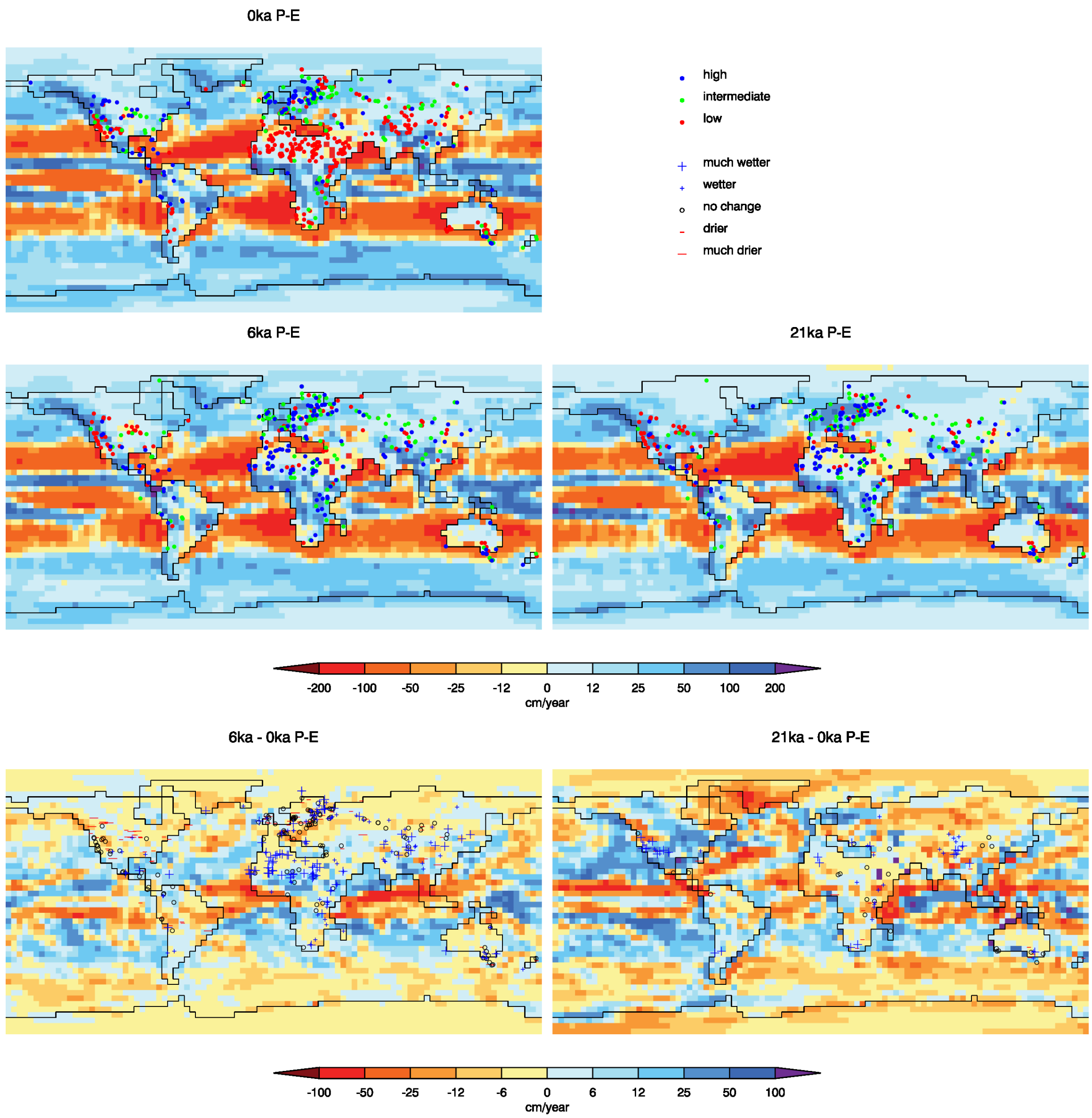

Figure 4.12 Annual net moisture (precipitation minus evaporation, P-E) for 0ka, 6ka, and 18ka with paleo lake level status over plotted (Kohfeld and Harrison, 2000; Harrison et al., 2003; Yu et al., 2001). Anomalies between 6ka – 0ka and 21ka – 0ka are shown (bottom) with changes in lake level status over plotted.

States wetting and Central American drying is in agreement with our hypothesis that the subtropical jet stream shifted for part of the year during the LGM. The LGM lake status for Africa are highly mixed with intermingled combinations of larger, smaller and unchanged lakes. Despite the regional heterogeneity, the GENMOM 21ka simulation appears to be in conflict with African LGM lake records in many locations. Lake levels in northern China, Mongolia, and southern Russia are curious as they all indicate larger lakes, whereas GENMOM generally shows reduced net moisture at these locations. The Asian pollen records consistently show less precipitation, but there are no pollen records for this region of northern China to help resolve this apparent contradiction. It may also be that the drastic LGM temperature cooling overcomes the balance of P-E, such that lakes are larger despite a general reduction in precipitation by evaporating less than the input from precipitation.

4.4.4 Atmospheric fields

During both boreal winter (DJF, Fig. 4.13) and summer (JJA, Fig. 4.14) the largest simulated changes in mean sea-level pressure occur over the northern hemisphere ice sheets, where high pressure centers form in response to cold surface temperatures. In winter, the Aleutian Low is strengthened in all past time slice simulations. Sea-level pressure is increased over Asia between 9ka and 3ka, which is a response to precessional induced cooling (Fig. 4.7). Between 21ka and 12ka, all high northern latitudes, including areas not covered by ice sheets, have increased pressure due to general cooling. The wintertime high-pressure region over North America is weaker than observed in 0ka (Alder et al., 2011), but is greatly strengthened between 21ka and 15ka due to the Laurentide Ice Sheet. As first noted by COHMAP (COHMAP Members, 1988) a strong

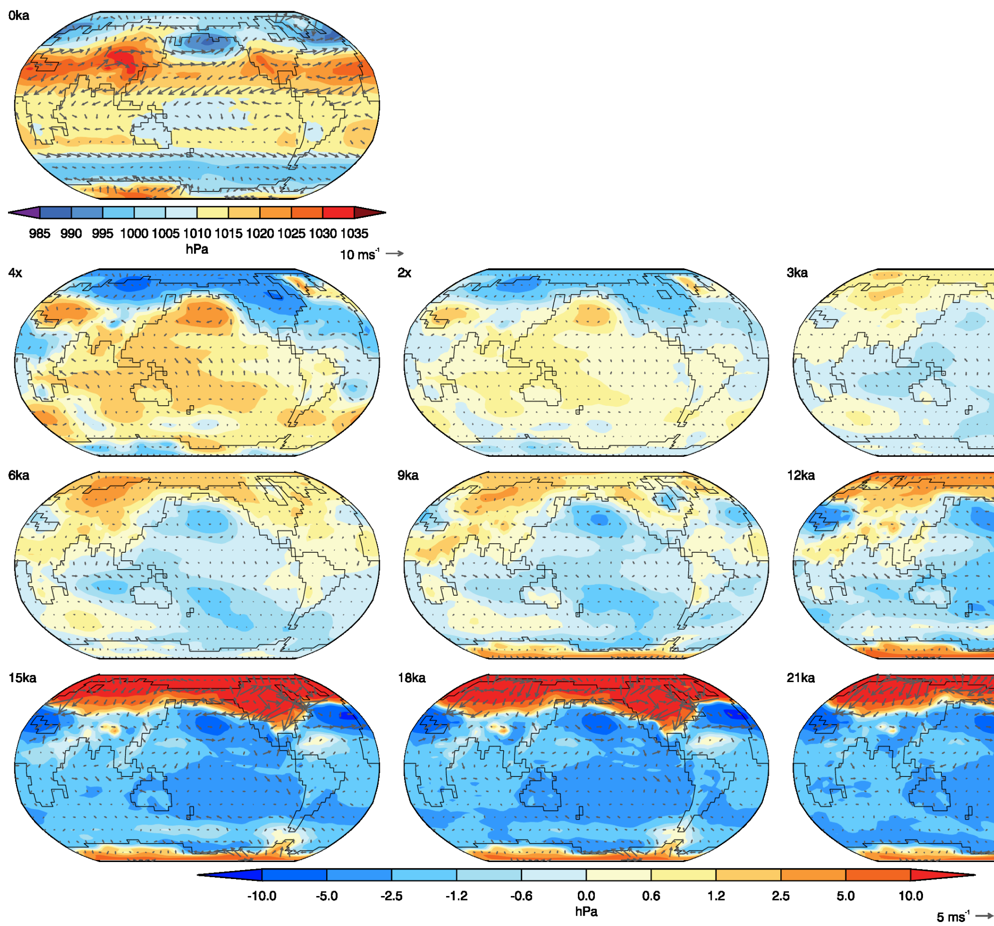

Figure 4.13 GENMOM December, January, February (DJF) sea-level pressure and wind anomalies from 0ka.

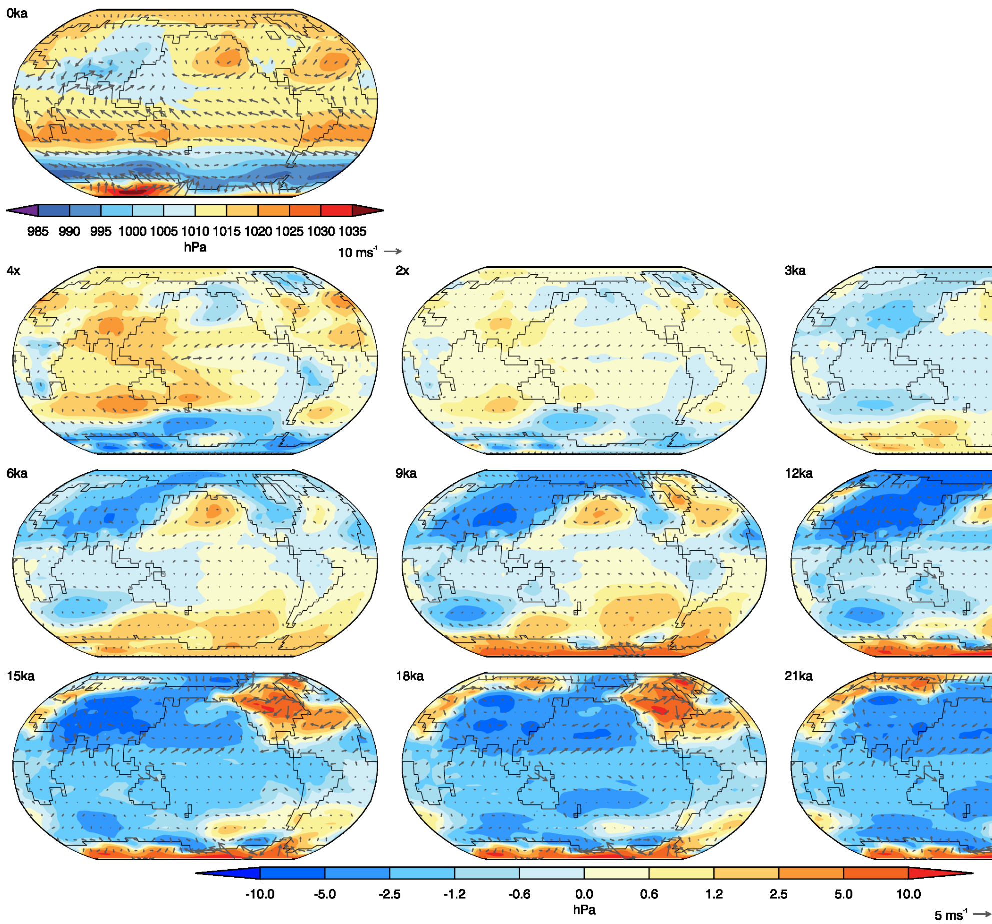

Figure 4.14 GENMOM June, July, August (JJA) sea-level pressure and wind anomalies from 0ka.

anticyclone develops over the Laurentide Ice Sheet during winter. During summer (JJA) between 12ka and 3ka, the sea-level pressure anomalies over northern hemisphere landmasses are the opposite of winter, because pressure is decreased due to insolation driven warming. During the same periods, the Hawaiian High is strengthened. Between 21ka and 6ka the Azores High is strengthened during summer. Similar to winter, pressure is greatly increased over the ice sheets.

The northern hemisphere winter (DJF) 500 hPa geopotential heights are generally reduced due to global cooling (Fig. 4.15). Similar to sea-level pressure, the largest changes in geopotential height is restricted to the northern hemisphere. The present-day wintertime North American 500 hPa ridge is displaced eastward relative to observations and is slightly too zonal (Alder at el., 2011). In our 21ka through 15ka time slice simulations, the North American ridge is greatly increased meridionally resulting in changes in geopotential height and wind patterns centered on Alaska. The 500 hPa jet stream south of the Laurentide Ice Sheet is compressed meridionally and greatly intensified between 21ka and 15ka. However, GENMOM does not simulate a distinct split jet as found by COHMAP (COHMAP Members, 1988). Summertime (JJA) also shows decreased 500 hPa geopotential heights in most latitudes, but with an increase between 15ka and 6ka in the northern mid latitudes, associated with increased summertime temperatures due to insolation in these periods (Fig. 4.16). Along with increases in northern mid latitudes geopotential height, the northern hemisphere jet stream is generally weakened between 15ka and 6ka during summer. Near the Laurentide Ice Sheet between 21ka and 15ka, the jet stream shows the same meridional compression and intensification as seen in winter.

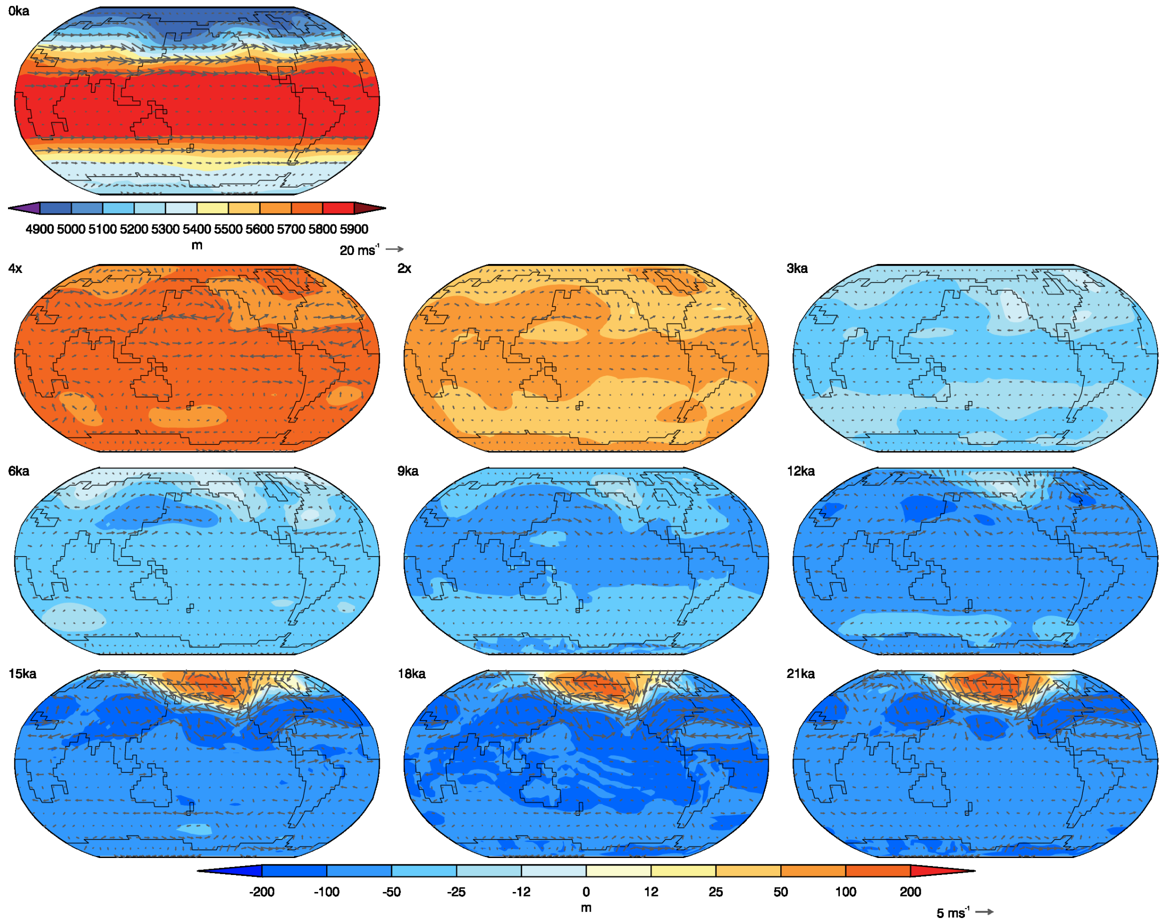

Figure 4.15 GENMOM December, January, February (DJF) 500 hPa geopotential height and wind anomalies from 0ka.

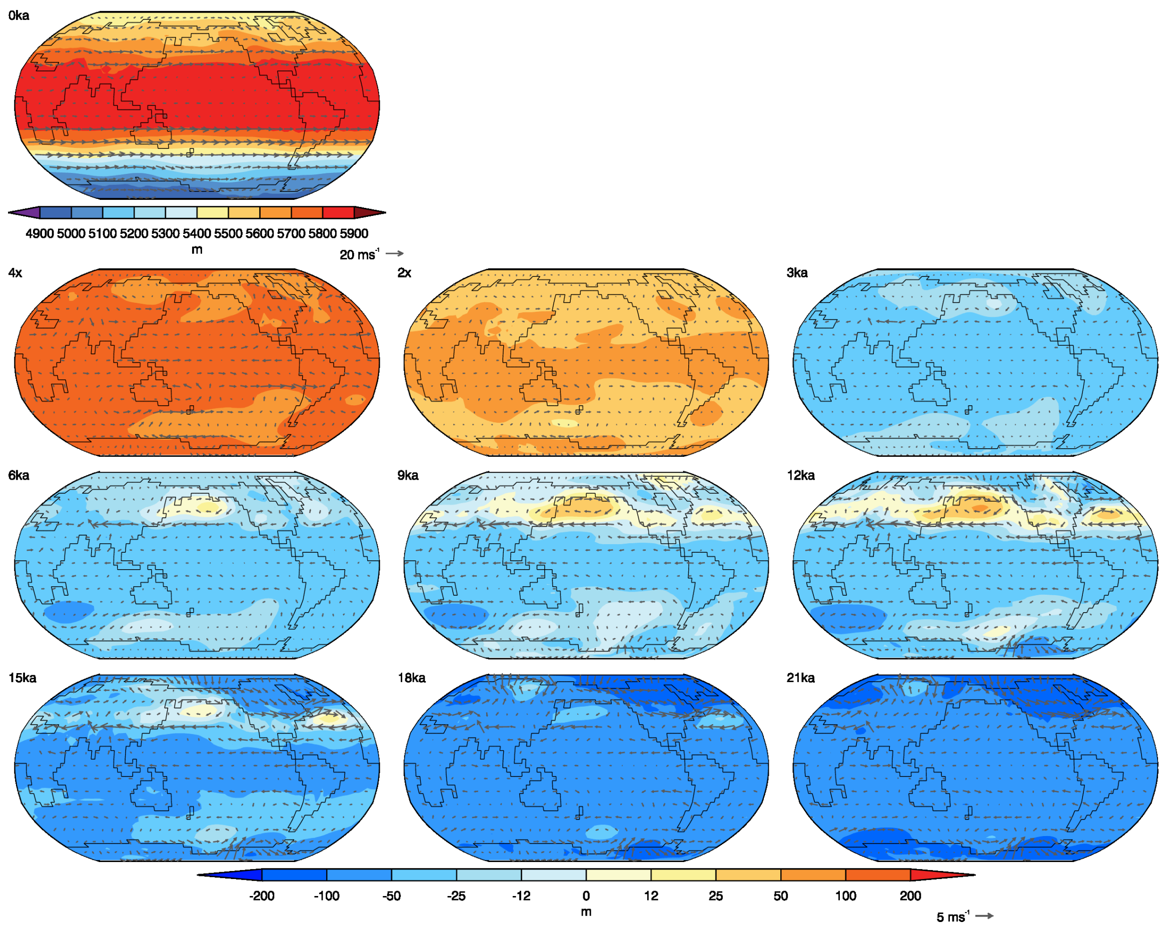

Figure 4.16 GENMOM June, July, August (JJA) 500 hPa geopotential height and wind anomalies from 0ka.

4.4.5 Atlantic Meridional Overturning Circulation

The Atlantic Meridional Overturning Circulation (AMOC) is part of a global oceanic circulation that brings warm, salty water to the surface of the North Atlantic and exports cold relatively fresh water southward in the deep ocean. This conveyor belt of energy facilitates transporting warm tropical water to high latitudes and is a major mechanism for distributing solar heating at the equator. A slowing or complete shutdown of the AMOC reduces ocean heat transport to the North Atlantic and would subsequently cool much of Europe (Rind et al., 1986). The GENMOM simulated AMOC is weaker than observed in the present-day simulation (Alder et al., 2011). In addition, the simulated AMOC time series does not follow the trend derived from Pa $^{231}Pa/^{230}Th$ in marine sediments which is a proxy for past AMOC strength (McManus et al., 2004; Fig. 4.17). Our GENMOM simulations are not expected to capture rapid or abrupt climate change events with only eight time slices, such as the slowdown of Heinrich event 1 (~17ka). We did not include site-specific freshwater injection ("hosing") in the North Atlantic in our experiments so they cannot capture abrupt events that alter the AMOC (Clark et al., 2001). The $^{231}Pa/^{230}Th$ record shows a gradual increase in AMOC strength from LGM to 0ka, whereas GENMOM shows a glacial to interglacial decline in AMOC strength, with a rapid delcine and resumption at 9ka. An AMOC induced cooling of Europe is not detectable in our time slices, which are dominated by the much stronger forcings of ice sheets, insolation changes and greenhouse gases.

4.5 Discussion and Conclusions

This study is the first attempt at data-model comparison for the LGM, deglacial, and Holocene using the new AOGCM, GENMOM, with a focus on reproducing past

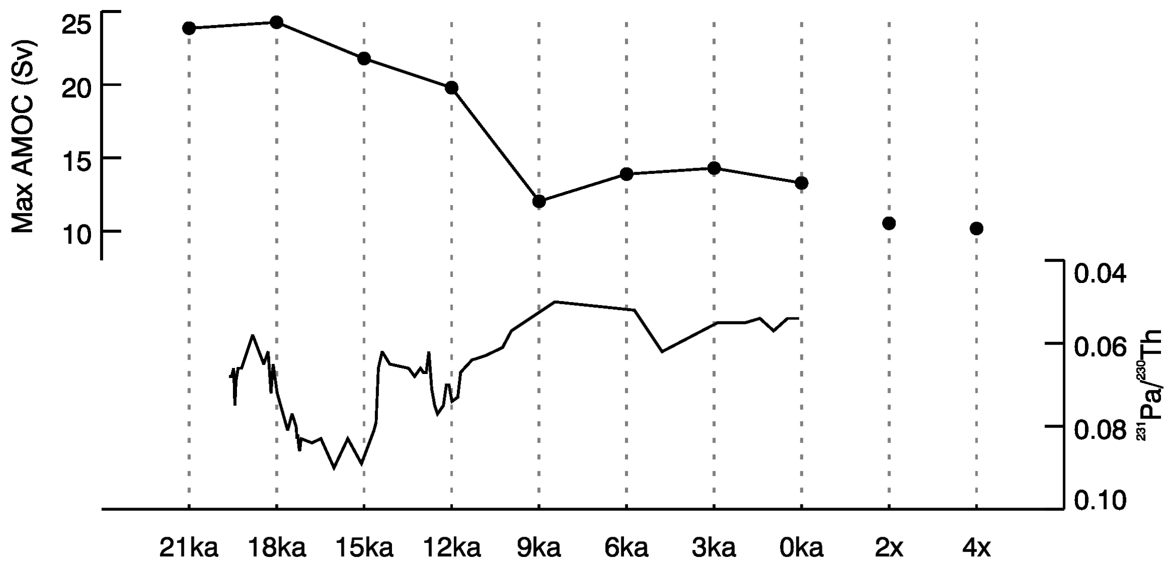

Figure 4.17 GENMOM simulated maximum Atlantic Meridional Overturning Circulation (AMOC) compared to $^{231}Pa/^{230}Th$ marine sediment record from the Bermuda Rise (McManus et al., 2004).

Pacific climate and changes in ENSO strength, which is addressed in Part II of our paper. Globally, GENMOM captures the glacial-interglacial changes in polar temperature relative to ice core isotope paleothermometer records. Although the model captures the general Holocene warming trend, with only eight simulations it is not expected to capture finer scale details such as rapid climate change (ie the Younger Dryas) because the runs are equilibrium simulations without event specific forcings such as freshwater injection. The model also does not simulate a 6ka ‘climatic optimum’, but rather continues to warm progressively to present. Reconstructed SSTs from the MARGO project are used to validate the 21ka simulation. We find that the model is in good agreement over broad spatial scales, with regional discrepancies between the model and proxy data. The simulated LGM is globally ~6.8 °C cooler than present due to an increase in northern hemispheric albedo from continental ice sheets and greatly reduced greenhouse gases. To evaluate our 6ka mid-Holocene simulation we utilize the GHOST SST reconstruction dataset. The reconstruction exhibits a mix of both regional SST warming and cooling relative to present-day, whereas GENMOM simulates overall global cooling of SST, which is associated with the lack of a simulated mid-Holocene ‘climatic optimum’. To evaluate temperature for the time slice simulations not covered by MARGO and GHOST we apply the new data compilations of Shakun et al. (*in prep*) for the deglacial and Marcott et al. (*unpublished*) for the mid to late Holocene. Using these new proxy compilations requires creating all anomalies from the 9ka simulations, stipulating any biases in our 9ka simulation will propagate to the anomalies in all other time slices Comparisons with these datasets suggests GENMOM is 1 - 2 °C too warm over Japan, Indonesia, Philippines, and the Southern Ocean during the deglacial and generally too warm in the mid to late Holocene where the proxies show a mix of warming and cooling at 6ka and 3ka.

Fossilized pollen reconstructions from the mid-Holocene indicate the western United States was wetter-than-present, while the east was predominantly drier. Much of Africa, Europe and Asia were considerably wetter-than-present. The GENMOM 6ka simulation agrees well with pollen records from Africa and the eastern United States, but does not agree with pollen proxies from the western United States, Europe and Asia. LGM pollen reconstructions exhibit widespread drying over Europe and Asia, while indicating increased precipitation in the southwest United States and drying in the east. The GENMOM 21ka simulation agrees very well with these patterns, but also recognizing that the pollen data are sparse.

The GENMOM mid-Holocene and LGM simulations are compared to reconstructed lake status records from the Global Lake Status Data Base (GLSDB) to evaluate changes in net moisture (precipitation – evaporation, P-E) to changes in lake volume. The model captures the observed mid-Holocene drying in the western United States and increased moisture in northern Africa, though the increased moisture does not extend to the northern most limit of the continent. GENMOM simulates a mid-Holocene reduction in net moisture over much of Europe, which is in conflict with pollen reconstructions that generally indicate larger or unchanged lake levels. GENMOM agrees well with an LGM increase in P-E in the western United States. GENMOM does support an expansion of northeastern Chinese lakes at the LGM, where Asian pollen records show decreased annual rainfall. These larger lakes could be caused by reduced evaporation due to cold LGM continental temperatures, despite reduced precipitation (Hostetler and Benson, 1990).

Globally, GENMOM simulates a reasonable climatology that is in general agreement with the best proxy reconstructions available. Our mid-Holocene simulations have a strengthened Indian summer monsoon, which is in agreement with previous modeling and proxy studies. The enhanced mid-Holocene monsoon is expected to influence the strength of ENSO events by strengthening west Pacific trade winds, thereby suppressing large events from developing. A detailed analysis of the tropical Pacific climatology and its influence on past and future strength of ENSO is provided in Part II of our paper.

4.6 Acknowledgments

We thank Jeremy Shakun, Shaun Marcott, Pat Bartlein, the MARGO and GHOST project members as well as the GLSDB lake database for making their proxy reconstructions available to us.

4.7 References

Alder, J. R., Hostetler, S. W., Pollard, D., and Schmittner, A.: Evaluation of a present-day climate simulation with a new coupled atmosphere-ocean model GENMOM, Geosci. Model Dev., 4, 69-83, doi:10.5194/gmd-4-69-2011, 2011.

Alder, J. R., Hostetler, S. W. and Pollard, D.: The sensitivity of ENSO to increased atmospheric CO2 as simulated by the atmosphere-ocean model GENMOM, *in prep*.

Bartlein, P. J., Harrison, S. P., Brewer, S., Connor, S., Davis, B. A. S., Gajewski, K., Guiot, J., Harrison-Prentice, T. I., Henderson, A., Peyron, O., Prentice, I. C., Scholze, M., Seppä, H., Shuman, B., Sugita, S., Thompson, R. S., Viau, A. E., Williams, J., Wu, H.: Pollen-based continental climate reconstructions at 6 and 21 ka: a global synthesis. Climate Dynamics, 10.1007/s00382-010-0904-1, 2010.

Berger, A. L.: Long-term variations of daily insolation and Quaternary climatic change. J. Atmos. Sci. 35, 2362 – 2367, 1978.

Braconnot, P., Otto-Bliesner, B., Harrison, S., Joussaume, S., Peterchmitt, J.-Y., Abe-Ouchi, A., Crucifix, M., Driesschaert, E., Fichefet, Th., Hewitt, C. D., Kageyama1, M., Kitoh, A., Loutre, M.-F., Marti, O., Merkel, U., Ramstein, G., Valdes, P., Weber, L., Yu, Y., and Zhao, Y.: Results of PMIP2 coupled simulations of the Mid-Holocene and Last Glacial Maximum – Part 2: feedbacks with emphasis on the location of the ITCZ and mid- and high latitudes heat budget. Clim. Past, 3, 279–296, 2007.

Brook, E. J., Harder, S., Severinghaus, J., Steig, E. J., and Sucher, C. M.: On the origin and timing of rapid changes in atmospheric methane during the last glacial period, Global Biogeochem. Cycles, 14(2), 559–572, 2000.

Clark, P.U., Marshall, S.J., Clarke, G.K. C., Hostetler, S. W., Licciardi, J.M., and Teller, J. T.: Freshwater Forcing of Abrupt Climate Change During the Last Glaciation. Science, Vol. 293 no. 5528 pp. 283-287, DOI: 10.1126/science.1062517, 2001.

CLIMAP Project Members: Seasonal reconstructions of the earth's surface at the Last Glacial Maximum, pp. 18, Geol. Soc. Am. Map and Chart Series, MC-36, 1981.

COHMAP Members: Climatic Changes of the Last 18,000 Years: Observations and Model Simulations. Science, New Series, Vol. 241, No. 4869, pp. 1043-1052, 1988.

Felzer, B.: Climate impacts of an ice sheet in East Siberia during the Last Glacial Maximum. Quaternary Science Reviews, 20, 437-447, 2001.

Gates, W. L., and Nelson, A. B.: A new (revised) tabulation of the Scripps topography on a 1° global grid. Part I: Terrain heights. RAND Corporation Tech. Rep. R-1276-1-ARPA, 132 pp, 1975.

Harrison, S. P., Kutzbach, J. E., Liu, Z., Bartlein, P. J., Otto-Bliesner, B., Muhs, D., Prentice, I. C., and Thompson, R. S.: Mid-Holocene climates of the Americas: a dynamical response to changed seasonality. Climate Dynamics 20, 663-688, doi:10.1007/s00382-002-0300-6, 2003.

Hostetler, S. and Benson, L.V.: Paleoclimatic implications of the high stand of Lake Lahontan derived from models of evaporation and lake level. Climate Dynamics, vol 4, num 3, 207-217, doi: 10.1007/BF00209522, 1990.

Jouzel, J., et al.: EPICA Dome C Ice Core 800KYr Deuterium Data and Temperature Estimates. IGBP PAGES/World Data Center for Paleoclimatology Data Contribution Series # 2007-091. NOAA/NCDC Paleoclimatology Program, Boulder CO, USA, 2007.

Kohfeld, K. E., and Harrison, S. P.: How well can we simulate past climates? Evaluating the models using global palaeoenvironmental datasets. Quaternary Science Reviews 19(1-5), 321-346, 2000.

Kutzbach, J.E. and Otto-Bleisner, B. L.: The sensitivity of the African-Asian monsoonal climate to orbital parameter changes for 9000 years in a low resolution general circulation model. J.Atmos.Sci., 39, 1177-1188, 1982.

Leduc, G., Schneider, R., Kim, J.-H., Lohmann, G.: Holocene and Eemian sea surface temperature trends as revealed by alkenone and Mg/Ca paleothermometry. Quaternary Science Reviews, vol 29, pg. 989–1004, doi:10.1016/j.quascirev.2010.01.004, 2010.

Liu Z, Kutzbach, J., Wu, L.: Modeling climate shift of El Nino variability in the Holocene. Geophys Res Lett 27:2265–2268, 2000.

MARGO Project Members: Constraints on the magnitude and patterns of ocean cooling at the Last Glacial Maximum. Nature Geoscience, vol 2, pp 127- 132, doi: 10.1038/NGEO411, 2009.

McManus, J. F., Francois, R., Gherardi, J.- M., Kelgwin, L. D. and Brown-Leger, S.: Collapse and rapid resumption of Atlantic meridional circulation linked to deglacial climate changes, Nature, 428, 834-837, 2004.

Monnin, E., Indermühle, A., Dällenbach, A., Flückiger, J., Stauffer, B., Stocker, T. F., Raynaud, D., and Barnola, J.-M.: Atmospheric CO2 concentrations over the last glacial termination. Science 291, 112-114, 2001.

NGRIP dating group: IGBP PAGES/World Data Center for Paleoclimatology Data Contribution Series # 2008-034 NOAA/NCDC Paleoclimatology Program, Boulder CO, USA, 2008.

Otto-Bliesner, B, Brady, E., Shin, S., Liu, Z., Shields, C.: Modeling El Nino and its tropical teleconnections during the last glacial-interglacial cycle. Geophys Res Lett 30 DOI 10.1029/2003GL018553, 2003.

Pacanowski, R.C.: MOM 2 Version 2.0 (Beta) Documentation: User's Guide and Reference Manual. NOAA GFDL Ocean Technical Report 3.2, 329 pp, 1996.

Peltier, W. R.: Global glacial isostatic adjustment: palaeogeodetic and space-geodetic tests of the ICE-4G (VM2) model. J. Quaternary Sci., Vol. 17 pp. 491–510. ISSN 0267-8179, 2002.

Pollard, D. and Thompson, S. L.: Climate and ice-sheet mass balance at the last glacial maximum from the GENESIS version 2 global climate model, Quaternary Sci. Rev., 16, 841–864, 1997.

Rind, D., Peteet, D., Broecker, W., McIntyre, A. and Ruddiman, W.: The impact of cold North Atlantic sea surface temperatures on climate: implications for the Younger Dryas cooling (11–10 k). Climate Dynamics, Vol 1, Num 1, pg 3-33, DOI: 10.1007/BF01277044, 1986.

Shakun, J. D., Clark, P. U., He, F., Liu, Z., Otto-Bliesner, B. L, Marcotts, S. A., Mix, A. C., Schmnittner, A., and Bard, E.:CO2 forcing of global climate during the last deglaciation, *in prep*.

Sher, A.: Is there any real evidence for a huge ice sheet in East Siberia? Quaternary International 28, 39-40, 1995.

Sowers, T., Alley, R.B., and Jubenville, J.: Ice Core Records of Atmospheric N2O Covering the Last 106,000 Years, Science, Volume 301, Number 5635, pp. 945-948, 2003.

Taylor, K.E., Stouffer, R.J., and Meehl, G.A.: A Summary of the CMIP5 Experiment Design. http://cmip-pcmdi.llnl.gov/cmip5/docs/Taylor_CMIP5_design.pdf, 2011.

Thompson, S.L. and Pollard, D.: A global climate model (GENESIS) with a land-surface-transfer scheme (LSX). Part 1: Present-day climate. J. Climate, 8, 732-761, 1995.

Thompson, S.L. and Pollard, D.: Greenland and Antarctic mass balances for present and doubled CO2 from the GENESIS version 2 global climate model. J. Climate, 10, 871-900, 1997.

UK Meteorological Office, Hadley Centre: HadISST 1.1 - Global sea-Ice coverage and SST (1870-Present), [Internet]. British Atmospheric Data Centre, Downloaded 2/8/2010. Available from http://badc.nerc.ac.uk/data/hadisst/, 2006.

Yu, G., Harrison, S. P., and Xue, B.: Lake status records from China: Data Base Documentation. Technical Reports - Max-Planck-Institut für Biogeochemie 4, 243 pp, 2001.

Chapter 5: Simulating ENSO from LGM to present and beyond: Part II Analysis of Past and Future ENSO Strength

J. R. Alder[1] and S. W. Hostetler[2]

[1]Oregon State University, Department of Geosciences, Corvallis, OR 97331, United States

[2]US Geological Survey, Oregon State University, Department of Geosciences, Corvallis, OR 97331, United States

5.1 Abstract

A new coupled atmosphere-ocean climate model, GENMOM, is applied to simulate past changes in the strength of the El Niño/Southern Oscillation (ENSO) to help expand our knowledge of both changes in past ENSO and to provide context for future changes. Equilibrium simulations are performed for the LGM (21ka), delgacial (18ka and 15ka), Holocene (12ka, 9ka, 6ka, 3ka), present-day, as well as a doubling (2x) and quadrupling (4x) of atmospheric CO_2. A global description and data-model comparison for these simulations are detailed in Part I of our paper. Mean state changes in the strength of Bjerknes feedbacks are analyzed to find ENSO was weaker and less frequent in the past and is simulated to be stronger and more frequent under the 2x and 4x atmospheric CO_2 scenarios. The Holocene simulations indicate a ~20% reduction in ENSO strength, in good agreement with the proxy reconstructions from corals and laminated lake records that indicate a 15% - 60% reduction in ENSO strength. A precessionally forced strengthening of the Indian summer monsoon, enhancing west Pacific trade winds that in turn inhibit ENSO development, drives weakening of ENSO in the Holocene. ENSO strength in the LGM is simulated to be weakened by ~25%, which is not found to be caused by changes in equatorial Pacific dynamics but rather mean state cooling that weakens the tropical thermocline. The 2x and 4x simulations have a strongly enhanced ENSO caused by disproportionate warming of the eastern Pacific relative to the western Pacific, which weaken the east-west Pacific surface temperature gradient, allowing larger anomalies, and hence ENSO events, to develop.

5.2 Introduction

The 1982-83 and 1997-98 El Niño events were the strongest in the historical record, leaving scientists asking if the El Niño/Southern Oscillation (ENSO) is changing because of global warming (Fedorov and Philander, 2000). A great number of studies have been performed to understand changes in ENSO using climate models forced with increased greenhouse gases (Collins, 2000a; Collins, 2000b; Guilyardi, 2006; Merryfield, 2006). Studying changes in future ENSO is complicated by the fact that only about 26 El Niño events have occurred since the early 1900s. The sea surface temperatures (SSTs) prior to the 1940s are sparse in coverage and different measurement techniques were used, which reduces the number of events for which we have accurate data to compare models to. To improve our knowledge of how ENSO may change in the future, we applied an Atmosphere-Ocean General Circulation Model (AOGCM) to simulate past ENSO, which can be compared to proxy records from corals and lake sediment records. Our simulation of the past also serves a dual purpose: the Coupled Model Intercomparison Project (CMIP5) in preparing for the upcoming Fifth Assessment Report of the Intergovernmental Panel on Climate Change (IPCC AR5) has deemed that the ability of a climate model to simulate the present climate is not in itself sufficient to judge the quality of models used to simulate the future. To gauge the ability of a climate model to simulate climates significantly different from present, CMIP5 will include simulations for the Last Glacial Maximum (LGM, ~21,000 years ago) and mid-Holocene (~6,000 years ago) to test the model's ability to simulate climate different than today (Taylor et al., 2011). Comparing our LGM and mid-Holocene simulations to both data and other models with provide us with a new method to evaluate the quality of climate simulated by GENMOM.

Fossilized corals from Papua New Guinea have been used to reconstruct near monthly variations in sea surface temperature and salinity during distinct periods in the past. These variations have been used to gauge the strength of ENSO in the past (Tudhope et al. 2001; McGregor and Gagan, 2004), where reduced variability in the Sr/Ca ratio in the corals implies weakened ENSO. The Tudhope et al. (2001) coral record is particularly important because the youngest corals display variability that matches well with observed ENSO events within the instrumental record, but the coral record also spans 130,000 years and indicates ENSO was active during glacial times. The Papua New Guinea corals (Tudhope et al. 2001; McGregor and Gagan, 2004) indicate weakened ENSO during the mid-Holocene, but and stronger-than-present ENSO between 2.5-1.7ka.

Laminated lake sediments in Ecuador that span the past 12,000 years continuously, imply a weakened ENSO during the mid-Holocene (Rodbell et al., 1999; Moy et al., 2002). The lake sediment record overlaps and correlates well with the historical record, adding confidence that the data captures past ENSO strength reasonably well. This sediment record indicates that ENSO was stronger-than-present at 1.5ka, weaker during the mid-Holocene, and very weak or not existent between 7ka – 10ka. The laminated lake data were reanalyzed by Rodo and Rodriguez-Arias (2004) who found the original analysis of Moy et al. (2002) was in error and that the 7ka - 10ka reduction in ENSO was greatly overstated. The revised analysis indicates ENSO was reduced by about a third during this period but was still clearly present.

Interpretation of each of these records implicitly assumes the temperature and precipitation teleconnection to the proxy location was essentially stationary, that is, the same in the past as it is today, which can be questioned with independent evidence. Although each proxy estimates ENSO strength differently, a 15 – 60% reduction in mid-Holocene ENSO strength is a consensus range supported by the proxy records. Sea surface temperature reconstructions for the LGM are difficult to interpret regarding ENSO changes as many reconstructions show conflicting results regarding changes in the Pacific east-west temperature gradient (CLIMAP Project Members, 1981; Lea et al., 2000; Koutavas et al., 2002; MARGO Project Members, 2009). Cole (2001) provides a summary of mid-Holocene ENSO changes and Donders et al. (2008) provides a listing of ENSO related proxies.

Climate models of intermediate complexity (EMICs) and coupled models atmospheric and ocean general circulation models (AOGCMs) broadly capture the mid-Holocene reduction in ENSO strength, but often exhibit modest reductions that are below or in the lower range supported by proxies. Using the Zebiak-Cane ENSO model, Clement et al. (1999) found that ENSO strength could be orbitally controlled by forcing their model with Milankovitch changes in insolation. The mid-Holocene reduction in their simulation was explained as being forced by precession, which caused asymmetric east-west heating of the Pacific during summer (JJA) when ENSO events typically develop. The asymmetric heating would strengthen the summertime east-west Pacific temperature gradient and the easterly trade winds that would inhibit development of El Niño events (Clement et al., 2000).

Many fully coupled AOGCM simulations have been performed that generally find a precession-driven strengthening of the Indian summer monsoon caused the mid-Holocene reduction in ENSO rather than an asymmetric heating of the Pacific. The monsoon enhanced easterly trade winds interact with ENSO dynamics by strengthening windstress, increasing convection, and steepening the east-west Pacific surface temperature gradient, all of which are thought to dampen ENSO strength in the mid-Holocene (Liu et al., 2000). Liu et al., (2000) originally put forth the Indian summer monsoon – ENSO hypothesis and supported the hypothesis by applying an AOGCM. Simulated reductions of ENSO strength of about 20% at 6ka and 14% at 11ka, corroborates well with the coral and lake proxies. Brown et al. (2006) found a somewhat weaker reduction of 12%.

Otto-Bliesner et al. (2003) performed a more extensive study including simulations for 3.5ka, 6ka, 8.5ka and the LGM. Their mid-Holocene simulations show a reduction (8%, 15%, and 10% respectively) whereas the LGM simulation shows a 20% increase in ENSO strength. Otto-Bliesner et al. (2003) invoke changes in the mean state of the tropical thermocline gradient as the cause of weakened ENSO rather than the monsoon enhancement hypothesis put forth by Liu et al. (2000). An et al. (2004) simulate a stronger LGM ENSO, but for the opposite reason identified by Otto-Bliesner et al. (2003). More recently, Zheng et al (2008) show that many of the PMIP2 model simulate a monsoon-driven weakening of ENSO during the Holocene (six models have a 2.9 – 22.5% reduction) but the models show mixed results at the LGM (three out of four models have a reduction). The simulated weakening of LGM ENSO lacks a mechanistic explanation; Zheng et al (2008) concluded the changes are less related to windstress and equatorial dynamics but rather to a mean state cooling of the tropical Pacific with a weakened thermocline gradient. While these models do simulate a mid-Holocene reduction in ENSO strength, many of them are on the low end of the 15 – 60% reduction found in the proxy records.

Here our goal is to explore past changes in ENSO from the LGM to present-day using the new AOGCM, GENMOM. GENMOM is applied to simulate past climate for 21, 18, 15, 12, 9, 6, 3, 0ka. These time-slice simulations illustrate how the simulated ENSO strength varied in the past compared to proxies, and they provide context for quantifying the evolution of ENSO under changes in trace gas forcing through a doubling (2x) and quadrupling (4x) of atmospheric CO_2. A full description of our experimental design and methods are given in Part I of our paper. We assume changes of the tropical Pacific climatology are due to the boundary conditions we impose on the model, not a strengthening or weakening of ENSO, which becomes circular. For the purpose of comparing past changes in ENSO strength to proxy reconstructions, we are not interested in specific mechanisms of ENSO development such as the delayed-oscillator (Schopf and Suarez, 1988; Suarez and Schopf, 1988; Battisti and Hirst, 1989), recharge-discharge oscillator (Jin 1997), or extra-tropically forced by North Pacific storms (Chiang et al., 2009).

The paper is organized as follows: in section 5.3 we discuss climatological changes in the tropical Pacific and components related to mechanisms of ENSO development and how those changes impact the overall strength of ENSO. Using the MARGO (MARGO Project Members, 2009) and GHOST (Leduc et al., 2010) datasets, as described in Part I, we compare the simulated tropical Pacific SSTs to proxy reconstructions. In section 5.4 we detail changes in the strength and frequency of ENSO in our simulations as well as a brief discussion of the simulated teleconnections. Finally, we conclude our paper with a discussion and summary of our main results.

5.3 Simulated pacific climatology

Prior to analyzing changes in ENSO strength, we first assess changes in the tropical Pacific climatology and how differences in Bjerknes feedback related components is expected to alter ENSO strength. Alder et al. (*in prep*) concluded that GENMOM simulates a tropical Pacific climatology that is generally similar to IPCC AR4 class models. However, the western warm pool is found to be too cool and eastern cold tongue too warm relative to observations. Although the model does not produce a tropical Pacific that is identical to the real world, simulated past and future changes in the east-west temperature gradient, equatorial windstress, east Pacific upwelling, and the strength of the tropical are expected to interact to alter the strength of ENSO.

During non-ENSO periods, the tropical Pacific is in a quasi-stable balance between SSTs and windstress related to trade wind convergence in the Intertropical Convergence Zone (ITCZ). Warm westerly waters give rise to buoyant air masses that drive deep tropical convection. Once lifted to the upper atmosphere, these air masses become divergent and are propagated eastward by upper atmospheric westerly winds. Cool eastern Pacific surface temperature causes surface divergence, which causes the upper atmospheric air mass to subside. Once at the surface, easterly winds complete the loop by forcing the air mass westward to the region of deep tropical convection. This convective loop is known as the Walker Circulation. Windstress caused by strong easterly winds force an oceanic response in the form of eastern coastal upwelling. The upwelled water is cool and is brought to the surface, helping to maintain the east-west temperature gradient. This balance of winds, water temperature and upwelling interactions are collectively known as Bjerknes feedbacks (Bjerknes, 1969).

ENSO events are a disruption of the Walker Circulation where the Bjerknes feedbacks are either weakened (El Niño) or strengthened (La Niña). El Niño events occur when the easterly trade winds relax, allowing the warm western waters to propagate eastward, thereby weakening the east-west temperature gradient. Since the convective branch of the Walker Circulation is centered on the region of warmest water, the eastward expansion of warm water forces an eastward shift of the convective branch. The position of convection strongly influences the location and intensity of rainfall over Southeast Asia and South America. The reduced windstress caused by the relaxed winds weakens upwelling, which helps to further reduce the east-west temperature gradient. La Niña events are generally the opposite of El Niño: the easterly trade winds strengthen which enhances upwelling along the coast of South America bringing more cool water to the surface thereby strengthening the east-west surface temperature gradient (Neelin et al., 1998). The increased easterly wind strength forces warm westerly surface waters west with the accompanying westward shift of rainfall.

Some authors use the terminology ‘La Niña-like’ or ‘El Niño-like’ to describe changes in mean Pacific SSTs under global warming scenarios or when describing past climate. We avoid this terminology here as we feel it adds confusion regarding the cause and effect of the warming or cooling. Changes in eastern Pacific SSTs can be caused by non-ENSO related sources, such as changes in the heat transport of subtropical gyres.

5.3.1 Comparison of simulated Pacific sea surface temperature with data

The degree to which sea surface temperatures changed in the tropical Pacific during the LGM and mid-Holocene is a widely debated topic. The CLIMAP LGM reconstruction (CLIMAP Project Members, 1981) indicates cooling of 2 °C in the west Pacific and 0 - 1 °C in the east Pacific, while other reconstructions indicate eastern Pacific cooling was much greater (Trend-Staid and Prell, 2002; Feldberg and Mix, 2003). For our purpose here, we use proxy records from the MARGO and GHOST reconstructions over the western and eastern Pacific to compare with our simulated changes in SST (Table 5.1). The MARGO reconstruction indicates ~2 °C cooling in the equatorial Pacific, with no change in east-west gradient. Our GENMOM 21ka simulation also display ~2 °C cooling, with no change in basin SST gradient. The GHOST mid-Holocene data indicate cooling of less than 0.5 °C with a small change in gradient, which matches our 6ka simulation. It should be noted, however, that our 6ka simulation has a net cooling of ~1 °C greater than seen in GHOST. Although the GHOST dataset does not show a significant change in east-west gradient, Mg/Ca based records from the Galapagos Islands indicate the gradient increased by ~0.5 °C between 5ka and 8ka (Koutavas et al., 2002). Although our lack of simulated gradient change at 21ka and minimal change at 6ka are in conflict with other modeling studies (Otto-Bliesner et al., 2003) they are consistent with the MARGO and GHOST datasets, indicating GENMOM is simulating realistic past temperature changes in the equatorial Pacific.

Comparison of the model time slice simulations for boreal winter (Fig. 5.1) and summer (Fig. 5.2) changes in tropical Pacific SSTs clearly indicate the 3ka, 2x and 4x simulations have a reduced east-west temperature gradient. Wintertime (DJF) cooling of

Table 5.1 Observed and simulated changes in SSTs for the West Pacific (10°S – 20°N, 100°E – 140°E) and the East Pacific (10°S – 10°N, 120°W – 80°W). MARGO and GHOST values are averages for all data points within the region.

	West Pacific (°C)	East Pacific (°C)	Gradient Change (°C)
MARGO (21ka)	-1.97	-1.98	0.01
GENMOM (21ka)	-2.27	-2.30	0.03
GHOST (6ka)	-0.24	-0.40	0.16
GENMOM (6ka)	-1.24	-1.41	0.17

the eastern cold tongue is present at 6ka, but not during summer (JJA), resulting in a modest annual change in the east-west gradient. There is disproportionately more cooling in the North Pacific than in the south between 15ka – 6ka, which is indicative of the wintertime (DJF) deficit in insolation. Changes in the east-west temperature gradient are calculated as the difference in SSTs between the Warm Pool (WP, 5°N - 5°S, 130°E - 170°E) and the Cold Tongue (CT, 5°N - 5°S, 130°W - 170°E). Using the more narrowly defined WP and CT regions (Fig. 5.3a), the 21ka simulation has a small gradient change relative to 0ka (-0.17), which is not in conflict with earlier finding of no gradient change compared to MARGO. The regions used in Table 5.1 were chosen to represent average changes in western Pacific and eastern Pacific temperature, and to include as many proxy reconstructions in the region as possible, whereas the smaller WP and CT regions have very few proxy records. The simulated temperature gradient is stronger from 9ka to 3ka, which would result in weakening of ENSO strength through Bjerknes feedbacks. The 2x and 4x temperature gradient is reduced substantially beyond any of the other time slices, implying strengthened ENSO.

5.3.2 Windstress

The east-west Pacific temperature gradient serves to enhance the strength of the easterly winds, such that a stronger gradient should enhance windstress along the equatorial Pacific. Indeed, the simulated Niño 4 (5°N – 5°S, 160°E – 150°W) windstress is a mirror image of the east-west temperature gradient (Fig. 5.3b), indicating the degree to which they are coupled. Similar to the temperature gradient, the 6ka and 9ka simulations have the strongest windstress, whereas the 2x and 4x simulations have the weakest windstress. Enhanced windstress inhibits the formation of anomalies (ENSO

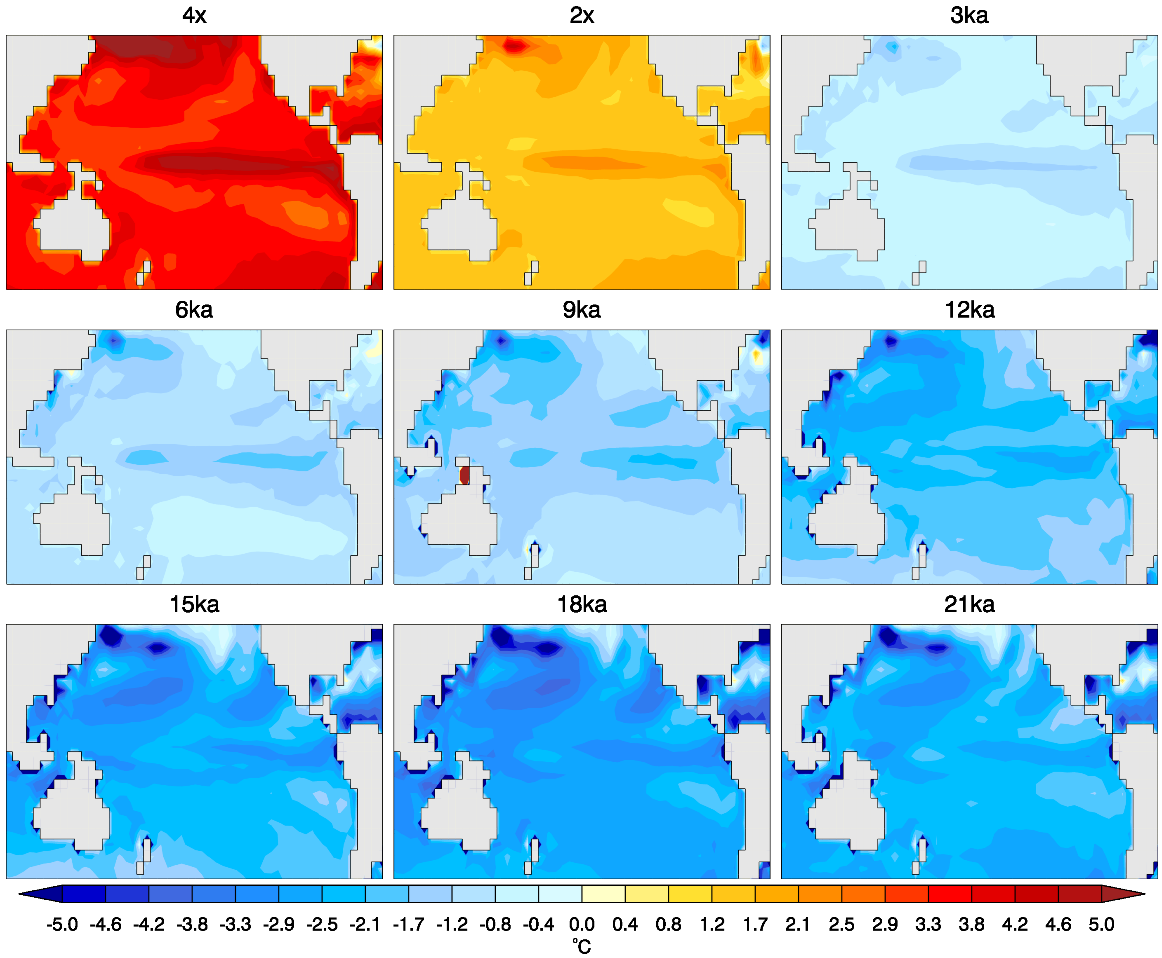

Figure 5.1 Detailed Pacific SST changes relative to 0ka during December, January, February (DJF).

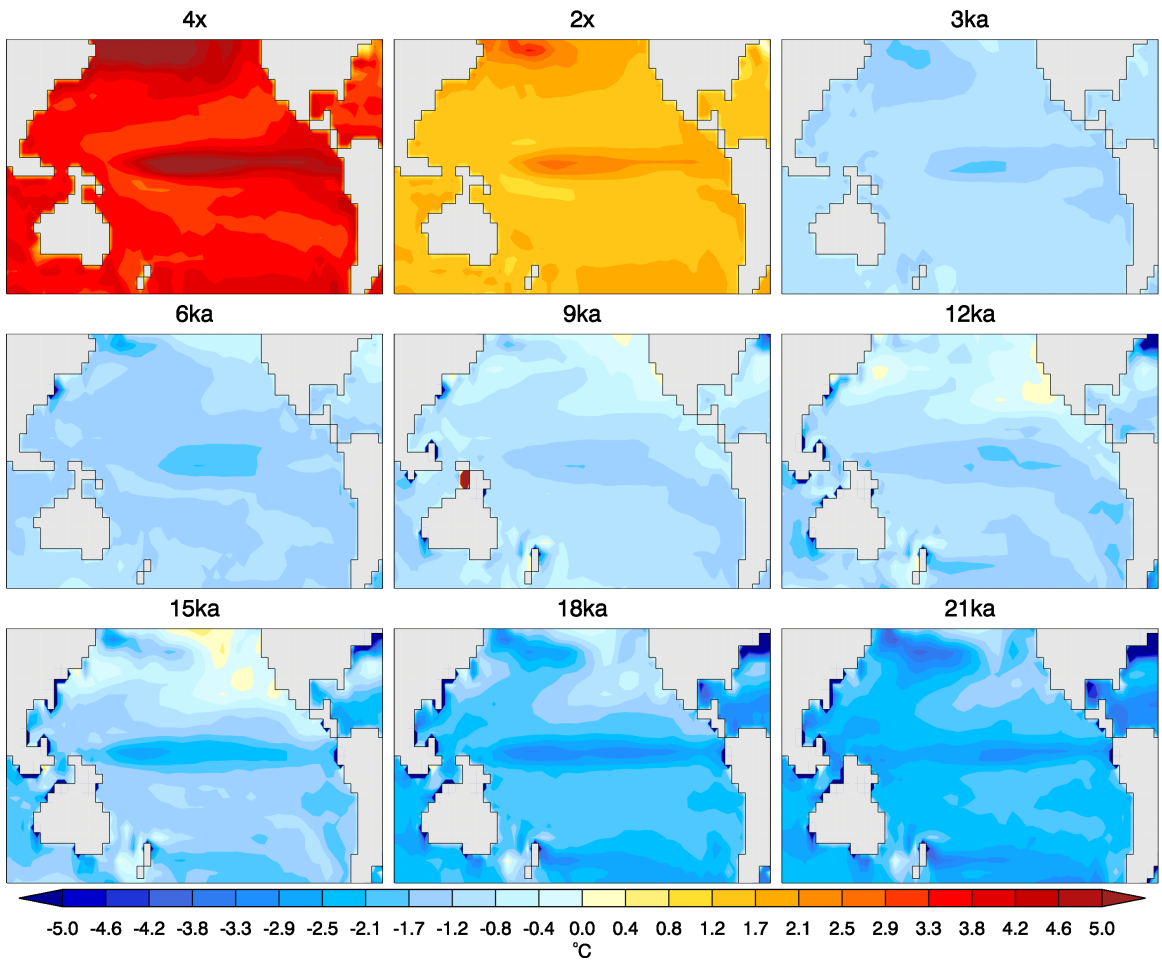

Figure 5.2 Detailed Pacific SST changes relative to 0ka during June, July, August (JJA).

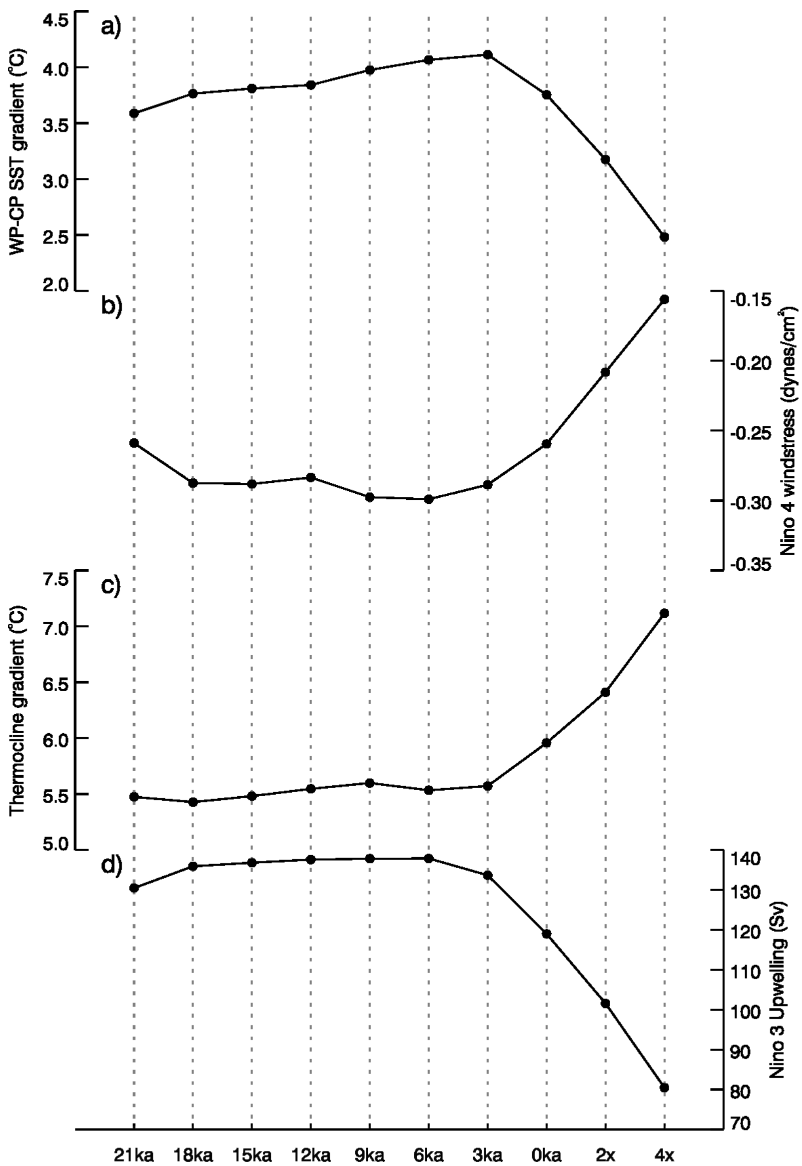

Figure 5.3 Changes in past and future mean state conditions related to Bjerknes feedbacks. a) The difference in the Warm Pool (WP, 5°N - 5°S, 130°E - 170°E) and the Cold Tongue (CT, 5°N - 5°S, 130°W - 170°E) SSTs, b) Niño 4 windstress, c) Vertical temperature gradient between the surface and 113 m depth in the Niño 3 region, d) Volume of annually upwelled water in the Niño 3 region.

events), whereas weak windstress favors the development of stronger anomalies, which lead to ENSO events.

5.3.3 Monsoon interactions

Based on analyses of ENSO dynamics, Liu et al. (2000) hypothesized that enhanced Niño 4 windstress during the mid-Holocene was associated with a strengthening of the Indian monsoon, which is known to influence ENSO strength in the present-day (Webster and Yang, 1992). Using an AOGCM, Liu et al. (2000) found that insolation driven strengthening of the Indian summer monsoon increased west Pacific windstress subsequently reducing ENSO strength in mid-Holocene simulations. Our 21ka – 15ka simulations produce enhanced windstress between January and June, and weakened windstress between August and November. Whereas the 12ka – 3ka increase in windstress primarily occurs between June and September (not shown), which are the key months for the Indian summer monsoon. The annual average Niño 4 windstress for our 9ka and 6ka simulations is enhanced by ~15%, near the 20% increase reported by Liu et al. (2000). In contrast, the Niño 4 windstress is reduced by 20% and 40% in the 2x and 4x simulations respectively, which will allow larger ENSO events to develop.

5.3.4 Upwelling and thermocline

Both the simulated thermocline gradient (Fig. 5.3c) and Niño 3 upwelling (Fig. 5.3d) are consistent with strengthened Bjerknes feedbacks during the paleo simulations and weakened feedbacks during the 2x and 4x simulations. The thermocline gradient is a measure of the strength of upper ocean temperature stratification. Stratification is thought to have been weakened during the Holocene by equatorward transport of warm subducted water from southern mid latitudes (Liu et al., 2003). These warm subsurface waters are caused by insolation anomalies during summer (JJA). Modeling studies have identified a more diffuse and weakened thermocline as a potential cause of reduced ENSO strength (Liu et al., 2000; Meehl et al., 2001; Otto-Bliesner et al., 2003). Enhanced equatorial windstress will strengthen east Pacific upwelling, bringing additional cold water to the surface. A cooler eastern Pacific will increase the east-west temperature gradient and drive stronger trade winds, both of which culminate to suppress ENSO development. Our 12ka – 3ka simulations show increased Niño 3 upwelling between June and September, which corroborates with timing of enhanced Niño 4 increase in windstress. All of our paleo time slice simulations have a thermocline gradient that is weaker than 0ka, with corresponding stronger than 0ka upwelling. The 2x and 4x simulations show distinctly weaker upwelling and sharper thermocline, indicating GENMOM is simulating a new regime in the tropical Pacific that is not seen in the paleo simulations, which will undoubtedly impact the strength of ENSO events.

5.3.5 Walker Circulation

Changes in the strength and location of the Walker Circulation are an integral part of ENSO variability, but proxy evidence to support such atmospheric changes does not exist. All of our paleo simulations have stronger Bjerknes feedbacks relative to 0ka, they also all display increased convection in the west and increased subsidence in the east (Fig. 5.4). The 21ka – 12ka simulations display increased subsidence at 100 °E, increased convection between 110 °E and 160 °W, and increased subsidence between 160 °W and 80 °W during winter (DJF). The westernmost positive anomalies in these time periods indicate subsidence over Indonesia and the Philippines during winter, a feature not present in the 0ka simulation or observations. Shin et al. (2003) found an eastward

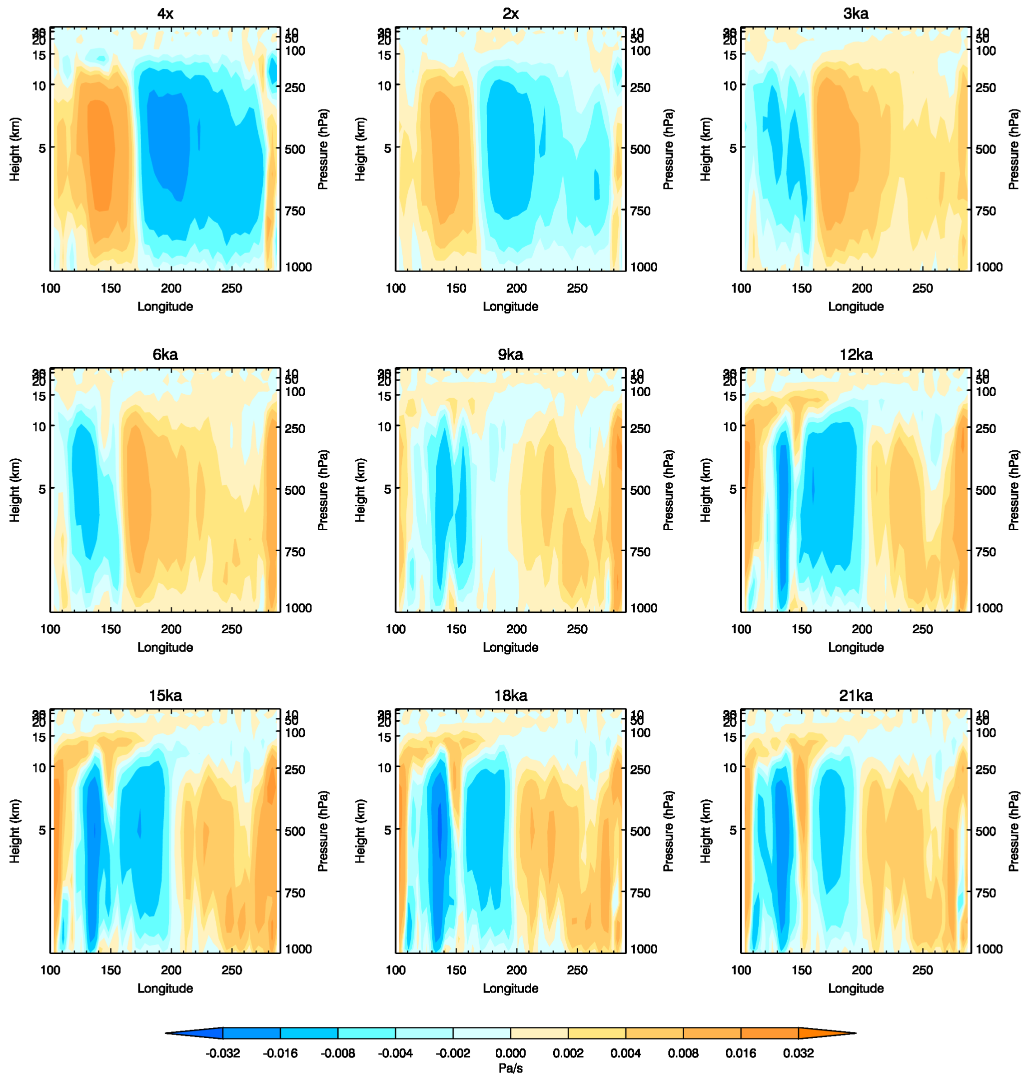

Figure 5.4 Changes in the Walker Circulation in the tropical Pacific relative to 0ka. Negative omega values indicate a tendency for increased vertical convection whereas positive omega values represent a tendency for increased subsidence.

shift of the Walker Circulation in a LGM simulation with an associated reduction in west Pacific precipitation. The 21ka simulation does have an eastward expansion of the zone of convection, with the accompanying changes in precipitation, but the western boundary of the region of convection is generally in the same location as in the 0ka simulation. Both the 6ka and 3ka simulations have strongly reduced convection centered at ~170 °E, indicating the zone of convection is more confined westward, yet negative anomalies in the far western Pacific indicate convection is strengthened despite being more confined. In the 2x and 4x simulations presented here, Alder et al. (*in prep*) found that with increased warming the western zone of deep tropical convection weakened and was displaced eastward by 15 - 20° and the corresponding zone of subsidence in the east was also weakened. The mean state eastward displacement produced a more confined region of ENSO action, and significantly reduced SST variability in the Niño 4 region in the 4x simulation.

5.4 Analysis of past and future ENSO

Thus far we have demonstrated that the GENMOM time slice simulations are generally in good agreement with the MARGO and GHOST proxy SST reconstructions, combined with the analysis of Alder et al. (*in prep*), we conclude that our simulations of Pacific climate are reasonable. In agreement with Liu et al. (2000), Otto-Bliesner et al. (2003), Brown et al. (2006), GENMOM simulates a mid-Holocene strengthening of the Indian summer monsoon, a weaker and more diffuse thermocline, and an increase in the east-west Pacific temperature gradient with attendant enhancement of equatorial trade winds. All of these modeling studies produce a 12-20% reduction in mid-Holocene ENSO strength, which is at the lower end of the reduction inferred from lake sediments and coral. Since our simulated strengthening of Bjerknes feedbacks is similar to these studies, we expect GENMOM to have a comparable reduction in mid-Holocene ENSO strength.

Proxy records are used to infer ENSO strength in a number of different ways, which are often inconsistent both among the types of proxies and authors. For example, Tudhope et al (2001) estimate ENSO strength as the variability in $\partial^{18}O$ within the ENSO band; however, the Ecuadorian lake sediment records analyzed by Rodbell et al. (1999) are interpreted as recording discrete El Niño events that are strong enough to cause geomorphological responses in lake laminates. Thus there are records of high frequency, lower amplitude ENSOs and records of lower frequency, and higher magnitude threshold ENSO responses. To address the differences in how corals and lakes measure ENSO, we analyze both changes in variability in the ENSO band (3 – 8 years) and changes in the number of El Niño event occurrences.

5.4.1 The Niño 3 index

Monthly sea surface temperature anomalies in the Niño 3 region provide a useful metric for ENSO strength (the Niño 3 index). Although GENMOM produces peak variability in the Niño 4 region (Alder et al., *in prep*), we adopt the Niño 3 index, which is where variability is greatest in the observations. There are many ways to define what constitutes an ENSO event (Quinn et al., 1978; SCOR, 1983; Wolter and Timlin, 1993). We use the definition of an El Niño (La Niña) event as a period when SST anomalies in the Niño 3 region remain above 0.5 °C (below -0.5 °C) for six consecutive months in a five month smoothed time series (Trenbeth, 1997). The Niño 3 indices for all our time slice simulations are shown in Fig. 5.5. The time series clearly show stronger events

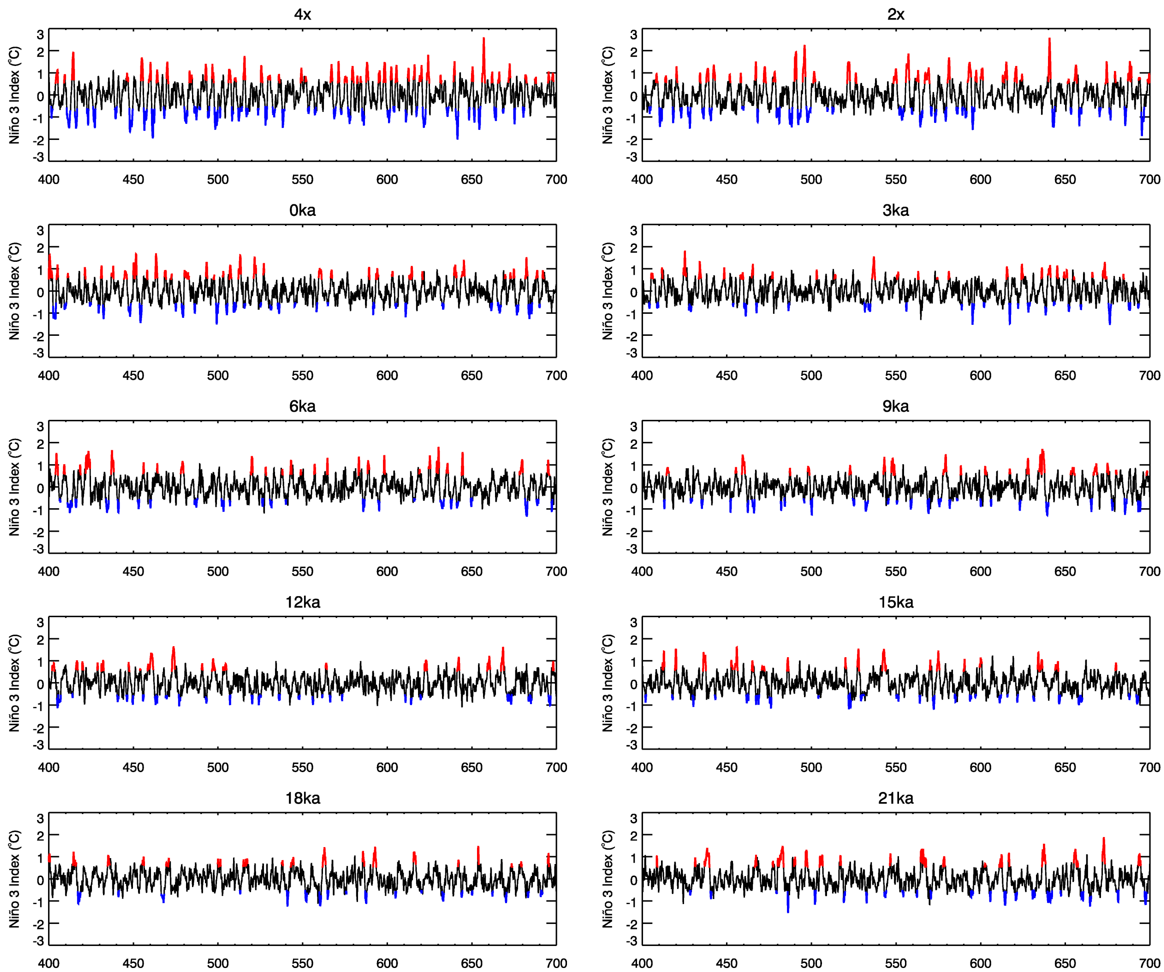

Figure 5.5 Sea surface temperature anomalies in the Niño 3 region for all time slice simulations using a 5-month smooth. El Niño events are highlighted in red and La Niña events in blue.

under 2x and 4x atmospheric CO_2 levels. The amplitude of events prior to 0ka are generally weaker, specifically at 18ka and 12ka. The standard deviation of the Niño 3 index bandpassed with a 3 – 8 year filter clearly illustrates the strength of ENSO was reduced in the past, whereas the 2x and 4x simulations have a stronger than present ENSO (Fig. 5.6a), as expected from our analysis of Bjerknes feedback components. All of the paleo time slices display less variability than 0ka, in accordance with the proxy records. With the exception of the 6ka simulation, our mid-Holocene simulations display a ~20% reduction in the variability of ENSO. At 6ka, ENSO is reduced to a lesser degree (10%), but is still in agreement with the proxy records (Moy et al., 2002). The 21ka – 15ka simulations exhibit less ENSO variability with a reduction between 20 – 25%. Our LGM ENSO, which is weaker than that of 0ka, contrasts with other modeling studies that found ENSO was enhanced at the LGM due to favorable background conditions and a shoaling of the thermocline (An et al., 2004). However, a weaker ENSO at 21ka is consistent with some of the PMIP2 models (Zheng et al., 2008).

To compare changes in the strength of ENSO to proxies that record discrete, large events (Rodbell et al., 1999; Moy et al., 2002), we analyze changes in the number of El Niño events that occur in our simulations, so that our measure of ENSO strength is applicable to these proxies. The time series of El Niño counts (Fig. 5.6b) is similar to the trend seen in the standard deviation of the Niño 3 index, wherein past ENSO is weaker than present and stronger in the 2x and 4x simulations (Fig 5.6a). There are ~8 El Niño events per century in our 6ka simulation, which corresponds well to the 6 - 12 events/century inferred from the Papua New Guinea corals between 7.6 - 5.4ka (McGregor and Gagan, 2004). Our 0ka simulation have ~13 El Niño events/century

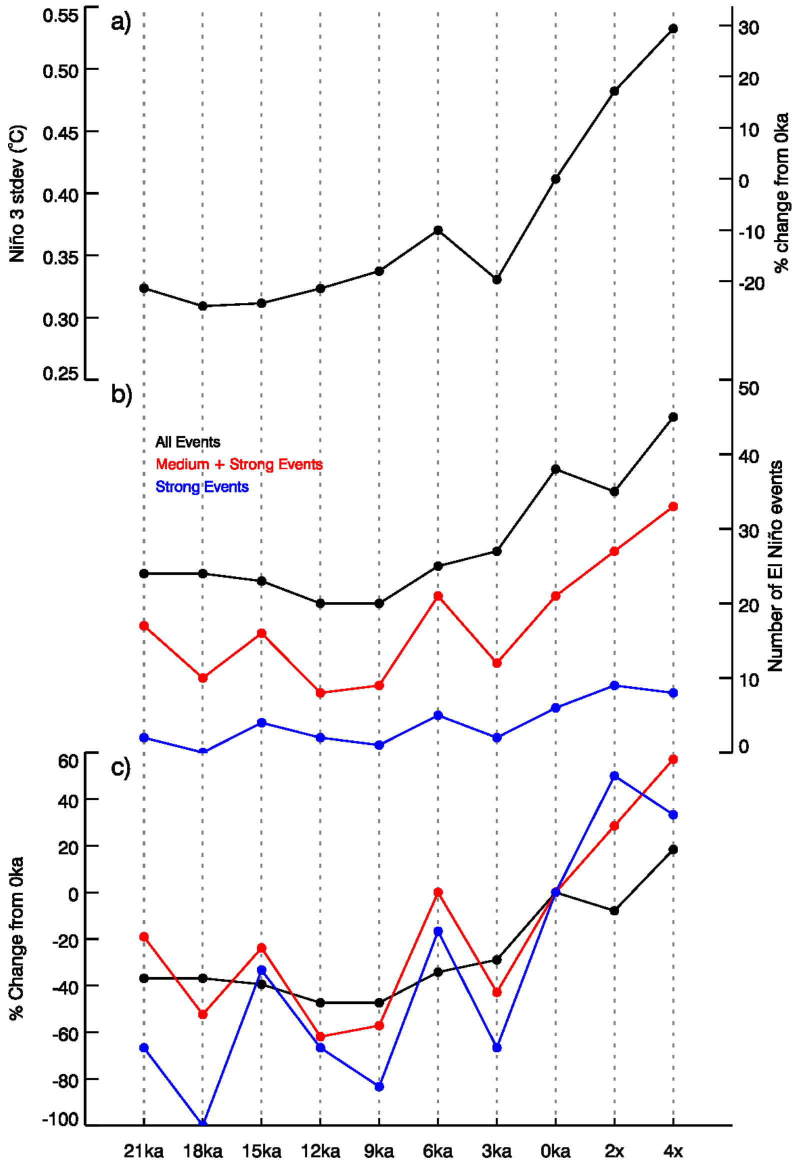

Figure 5.6 Changes in simulated ENSO strength through time. a) standard deviation of the monthly Niño 3 index using a 3 - 8 year bandpass filter, b) count of all El Niño events (black), events with a peak temperature anomaly >= 1.0 ºC (red), and events with a peak >= 1.5 ºC (blue), c) number of El Niño events (same coloring as b.) shown as percent change from the 0ka simulation.

which is somewhat lower than the 19 events/century McGregor and Gagan (2004) found between 1950-1997, confirming the finding of Alder et al. (*in prep*) that GENMOM simulates lower-than-observed ENSO frequency. Based on the number of El Niño counts (Fig. 5.6c), rather than changes in standard deviation, our paleo simulations have 25 – 50% fewer El Niño events, in better agreement with the proxies than the simulated change in variability. By limiting our analysis to medium and strong events (defined as peak SST anomalies >= 1.0 ºC), the 12ka, 9ka and 3ka simulations indicate an even greater 40 – 60% reduction (6ka remains anomalously strong). In the Niño 3 region, the 2x and 4x simulations have a 17% and 30% increase in variability and a 29% and 57% increase in the number of medium to strong El Niño events.

Analyzing changes in the number of events may be useful for comparison to certain types of proxies, however changes in the Niño 3 index standard deviation is more common in model-to-model comparisons. The paleo time slice simulations generally have the same east-west trend as the 0ka simulation, where the highest variability is simulated in the Niño 4 region and the lowest in Niño 3 (Fig. 5.7). The 2x and 4x simulations show a dramatic reduction in Niño 4 variability associated with the eastward shift and the Walker Circulation (Alder et al., *in prep*). The 21ka simulation also has reduced Niño 4 variability, but does not appear to be associated with changes in the Walker Circulation (Fig. 5.4).

Proxy records have difficulty detecting changes in ENSO frequency because many of the interpretations rely on thresholds to define ENSO events. In the case of the laminate lake records from Ecuador, fewer El Niño event counts do not necessarily imply reduced frequency, but rather that the events are weaker and no longer induce a

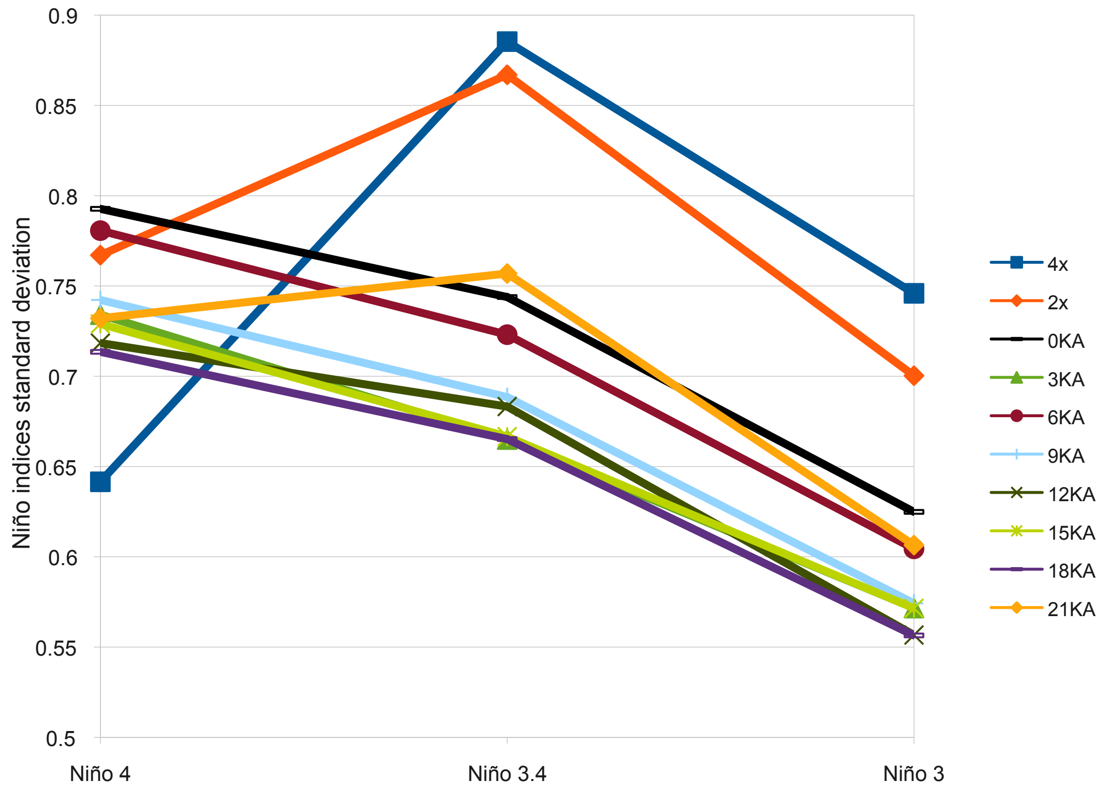

Figure 5.7 Past and future changes in the standard deviation of the Niño indices.

geomorphological response. In the case of climate models, changes in ENSO frequency can be evaluated by performing wavelet analysis on the Niño 3 SSTs (Fig. 5.8). As noted by Alder et al. (*in prep*), the 4x simulation has a decreased period of 4.6 years compared with the present value of 5.6 years. The paleo time slice simulations generally have less spectral power (associated with weakened ENSO) and longer periods, with the exception of 6ka and 3ka, which have slightly more frequent events. The wavelet spectra also reveal a trend of strong semi-annual power (6-month peak) and weak annual power in the 4x simulation to the opposite at 21ka (weak semi-annual, strong annual). It is unclear how the GENMOM simulated semi-annual cycle in the eastern tropical Pacific impacts the model's ability to simulate ENSO. Some authors note a strong annual cycle results in reduced ENSO strength (Timmermann et al., 2007), which generally agrees with our results, with the exception of the 12ka simulation that has both weak ENSO and weak annual cycle.

5.4.2 Bjerknes feedbacks and ENSO strength

The Pacific mean climate is generally in a quasi-stable balance between Walker Circulation strength (convection, surface easterly winds, and subsidence), the east-west temperature gradient, and eastern upwelling, where ENSO events are a disruption of this balance. In our ten simulations we find the strength of ENSO is directly related to changes in these Bjerknes feedbacks (Fig. 5.9). Western windstress and the east-west SST gradient share a near linear relationship (Fig. 5.9a) where stronger easterly winds setup a stronger temperature gradient, and the stronger gradient enhances winds in a circular, positive feedback. If we view our ten simulations as a sensitivity test of Bjerknes – ENSO strength feedbacks (different boundary conditions notwithstanding) it

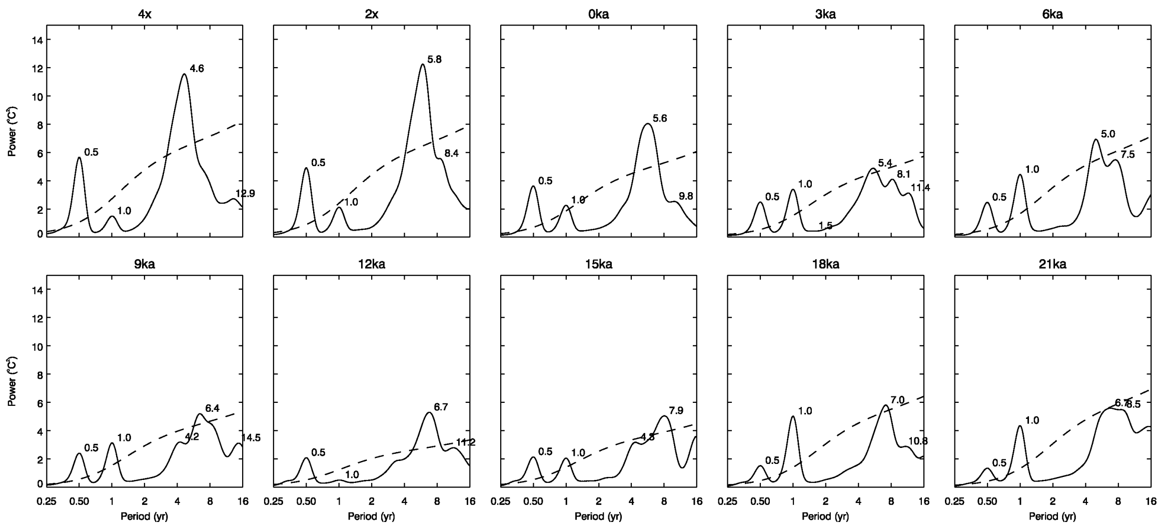

Figure 5.8 Spectra of Niño 3 SSTs as calculated by wavelet analysis.

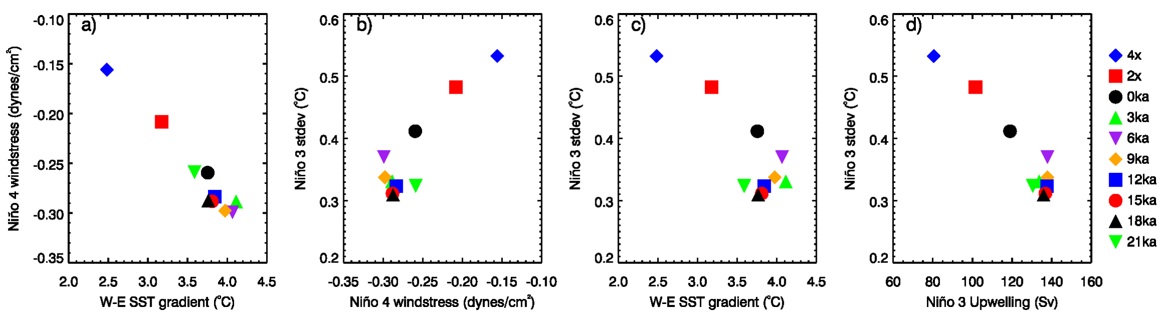

Figure 5.9 Scatter plots linking the strength of ENSO to various Bjerknes feedbacks. The standard deviation of the Niño 3 index uses a 3 – 8 year bandpass filter.

becomes clear that changes in the mean state govern ENSO strength in our simulations. While it is not surprising that the strength of Bjerknes feedbacks are directly related to ENSO strength, it is perhaps surprising how linear the relationship between windstress and ENSO strength and between upwelling and ENSO are in GENMOM considering the complexity of the dynamic interactions that make up ENSO (Fedorov and Philander, 2001). The relationship between the east-west Pacific temperature gradient and ENSO strength is less clear, but does indicate a weaker gradient corresponds to stronger ENSO. We also note Bjerknes feedbacks, and hence ENSO strength, in the 2x and 4x simulations are well outside of the 0ka – 21ka simulation range, indicating the tropical Pacific under global warming may be operating in a new regime with greatly strengthened ENSO, the likes of which have not been seen in the past 21,000 years.

The poor match between the simulated past AMOC and the proxies is of some concern regarding ENSO. Using five AOGCMs Timmermann et al. (2007) found weakening the AMOC tends to weaken the annual cycle of SSTs in the Pacific, which in turn strengthens ENSO. Our simulations do show weakening AMOC is associated with strengthening of ENSO; however, our paleo time slice simulations have a rapidly changing AMOC between 6ka and 12ka (Part I Fig. 4.17), which does not correspond to changes in ENSO strength (Fig. 5.6a), indicating the AMOC maybe a minor influence on ENSO strength in GENMOM.

5.4.3 Interaction with the Indian monsoon

Many modeling studies have found mid-Holocene simulations have a strengthened Indian summer monsoon, due to increased northern hemisphere seasonality driven by precession (e.g., Kutzbach and Otto-Bleisner, 1982, Braconnot et al., 2007),

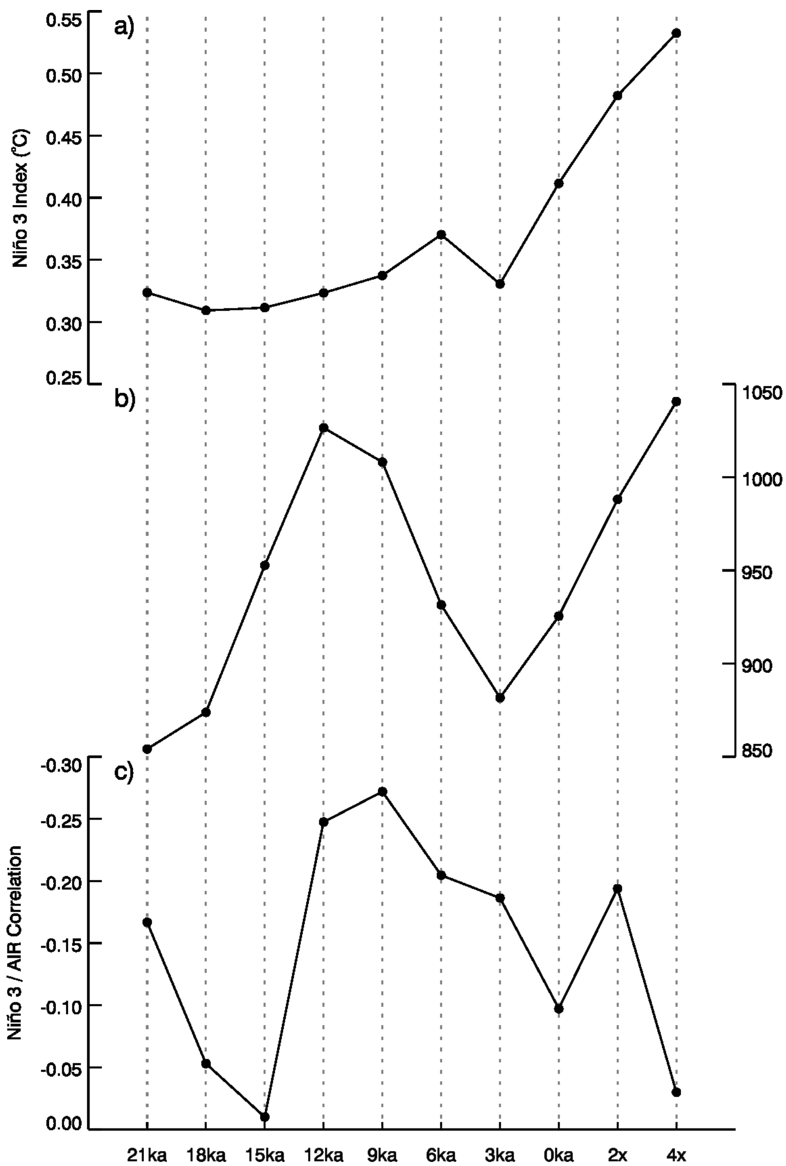

Figure 5.10 The strength of the Indian summer monsoon and its correlation to ENSO. a) standard deviation of the monthly Niño 3 index using a 3 - 8 year bandpass filter, b) the All India Rainfall (AIR) index defined as the sum of all June – September (JJAS) rainfall over all land grid cells between 5 ºN – 30 ºN and 60 ºE – 100 º, c) the correlation between the Niño 3 index standard deviation (JJAS only) and the AIR index.

and that a strengthened monsoon suppresses ENSO by enhancing western Pacific windstress (Liu et al., 2000; Brown et al., 2008). Our simulations also exhibit a strengthened Indian summer monsoon between 15ka and 6ka (Part I Fig. 4.11) that corresponds to the time of increased summer (JJA) insolation (Part I Fig. 4.2). To quantify the change in the Indian monsoon, we use the All India Rainfall index (AIR, Sontakke et al., 1993) which is defined here as the sum of June – September (JJAS) rainfall between 5 ºN – 30 ºN and 60 ºE – 100 ºE over land grid cells only (Fig. 5.10b).

Between 15ka and 9ka, and also in the 2x and 4x simulations, the simulated Indian monsoon is distinctly stronger than that of the 0ka simulation. Precipitation anomalies for 6ka indicate increased summer (JJA) rainfall (Part I Fig. 4.11), but the AIR index is similar to 0ka. As previously discussed, GENMOM does simulate strengthened JJAS windstress in the mid-Holocene simulations, which weaken ENSO via Bjerknes feedbacks. The correlation between the seasonal AIR index (seasonal anomalies) and Niño 3 index illustrates that monsoon strength is negatively correlated to ENSO strength, with a stronger-than-0ka correlation from 12ka – 3ka (Fig. 5.10c). The 0ka correlation value of ~-0.1 is lower than the values found by Liu et al. (2000) and Brown et al. (2008) which are -0.28 and -0.38 respectively, but the mid-Holocene increase in correlation matches their results, indicating the strength of the monsoon influences ENSO strength.

5.4.4 Seasonal timing / phase locking

Observations indicate that El Niño events typically develop during summer (JJA), peak in winter (DJF), and decay sometime during the following spring (MAM), requiring interactions between the seasonal cycle of SSTs and winds. This seasonal interaction, known as phase locking, can be seen in the historical average of El Niño seasonal timing

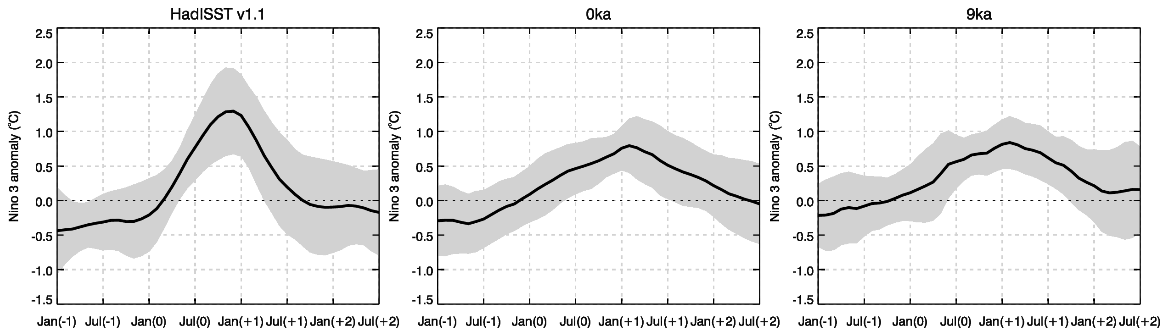

Figure 5.11 Seasonal phase locking of El Niño events for observations (left), 0ka (middle), and 9ka (right). Observations are from the HadISST v1.1 dataset from 1880-2007 (UK Meteorological Office, 2006).

(Fig. 5.11). Like many non-flux correct AOGCMs (AchutaRao and Sperber, 2006; Guilyardi, 2006), GENMOM does not exhibit the characteristic summer initiation and winter peak, but rather the model develops ENSO events in any season. This is likely caused by GENMOM incorrectly simulating the Pacific SST seasonal cycle by including an anomalous semi-annual cycle that is not seen in observations.

The mechanism put forward by Clement et al. (1999) to explain an insolation driven mid-Holocene weakening of El Niño events calls for a late summer strengthening of equatorial winds due to strengthening the east-west Pacific temperature gradient. The mechanism requires the east-west gradient to increase during summertime when El Niño events typically develop, thereby inhibiting events from fully developing and prematurely peaking in fall (SON) rather than winter. Since the events do not have enough time to mature, they peak with less strength than in present-day (Clement et al., 2000). We cannot test the mechanism described by Clement et al. (1999) to explain our GENMOM mid-Holocene reduction of ENSO strength for three reasons: (1) GENMOM does not phase lock to the seasonal cycle in the 0ka or 9ka simulations, where the 9ka seasonal timing (or lack thereof) is generally unchanged relative to 0ka (Fig. 5.11). (2) GENMOM produces a mid-Holocene reduction in east Pacific windstress in late summer (September and October, not shown) rather than an enhancement. However, GENMOM does simulate enhanced west Pacific windstress between June through September, which is associated with a strengthening Indian monsoon. (3) The GENMOM mid-Holocene simulations show only a slight increase in the summertime east-west Pacific temperature gradient (Fig. 5.2), which is part of the driving force for ENSO suppression in the Clement et al. (1999) hypothesis.

5.4.5 Teleconnections

Changes in past spatial patterns of temperature and precipitation associated with ENSO events are important to the interpretation of proxies as many proxies rely on $\partial^{18}O$ or similar isotopic ratios that capture both changes in temperature and precipitation. A change in spatial teleconnection could wrongly be interpreted as a change in the strength of ENSO. Analyses of isotopic based proxies often assume the past teleconnection spatial patterns were essentially the same as they are today, unless independent evidence supports a change in moisture or temperature. Our time slice paleo simulations indicate this assumption is generally valid as global teleconnections for both temperature and precipitation are similar in the paleo simulations as they are in the 0ka simulation. The 0ka simulation indicates India has a cool temperature teleconnection during El Niño events; this teleconnection is weakened between 12ka – 3ka and reversed to a warm temperature teleconnection from 21ka to15ka. This reversal is not seen during La Niña events. In the 0ka simulation, North America has a strong warm temperature teleconnection during El Niño events, Alaska a cool temperature teleconnection, and Central America a cool temperature teleconnection. This pattern generally holds through all our paleo simulations, but the Central American cool teleconnection is greatly strengthened between 21ka and 15ka. In the 0ka simulation, the western Pacific Warm Pool and Indian Ocean have a strong increase in precipitation during La Niña events, which is associated with warm SSTs and the zone of convection being forced westward by strengthened winds. This pattern holds in all our paleo simulations, but is noticeably weaker at 21ka and 18ka. While Alder et al. (*in prep*) find a few drastic changes in ENSO teleconnections in the 2x and 4x simulations, our paleo simulations by and large have spatial patterns that are consistent with the 0ka simulation, which adds credibility to the assumption used in proxy analysis that teleconnections in the LGM and late-Holocene were similar to those seen today. Our finding that LGM teleconnection patterns are largely the same as present is in conflict with the work of Otto-Bliesner et al. (2003) who found a weakened precipitation teleconnection to the location of the Papua New Guinea corals, 10% reduced mean precipitation at those sites, and an eastward shift in the Walker Circulation, both of which impact the interpretation of Papua New Guinea corals.

5.5 Discussion and Conclusions

The ability to simulate reasonable changes in past Pacific temperature is key to simulating past ENSO. Using broad area averages, GENMOM simulates an LGM cooling in the eastern and western Pacific in agreement with the MARGO reconstruction, with ~2 °C cooling in both east and west Pacific regions. The GENMOM mid-Holocene simulations indicate a cooling between 1.2 – 1.4 °C, which is a degree colder than SSTs found in the GHOST dataset. Though these bulk area averages are in agreement with the proxy records, smaller more focused regions on the equatorial Pacific (where there are far fewer, if any proxy records) show a 0.3 °C increase in the mid-Holocene east-west temperature gradient, and a 0.7 °C reduction in the LGM temperature gradient. The east-west Pacific surface temperature gradient in the 21ka simulation is slightly weaker than in the 0ka simulation, 18ka – 12ka are similar to 0ka, and 9ka – 3ka simulations are stronger than 0ka. The east-west temperature gradient is sharply reduced in the 2x and 4x simulations where the east Pacific cold tongue warms significantly when forced by increased atmospheric CO_2. The 18ka - 3ka simulations all exhibit enhanced windstress in the Niño 4 region, while the mid-Holocene simulations primarily have stronger winds between June and September (JJAS) that is associated with a strengthened Indian summer monsoon. The Indian summer monsoon is strengthened due to increased northern hemisphere seasonally forced by positive summer (JJA) insolation anomalies because of a precessional shift in the timing of peak insolation (Kutzbach and Otto-Bleisner, 1982, Braconnot et al., 2007). Upwelling in the eastern Pacific is greatly strengthened in our 21ka – 3ka simulations and weakened in the 2x and 4x simulations, each with corresponding changes in the vertical thermocline temperature gradient.

The observed ENSO proxy records indicate a 15 – 60% reduction in mid-Holocene strength, but these proxies fundamentally capture changes in ENSO strength in different ways. To address these differences in types of proxies, we provide an analysis of ENSO strength based on both variability in the ENSO band (3 – 8 years) and the number of El Niño event occurrences. The variability based metric indicates our mid-Holocene simulations have ~20% reduced ENSO strength, which is in good agreement with the proxy records, while our deglacial simulations show a 25% reduction in strength. The 2x and 4x elevation atmospheric CO_2 simulations show a striking 17% and 29% increase in variability. Using the occurrence based metric of strength, our mid-Holocene simulations have 25 – 50% fewer El Niño events, while the deglacial and LGM simulations have 35 – 40% fewer El Niño events. To correspond with the increased variability in the 2x and 4x simulations, these simulations show 29% and 57% more medium and strong El Niño events respectively. Wavelet analysis is used to confirm that ENSO events in our paleo time slices are generally less frequent and less intense, whereas the 2x and 4x simulations are more intense and more frequent.

Our analysis shows a near linear relationship between ENSO strength and west Pacific windstress as well as between ENSO strength and eastern upwelling. The relationship between the east-west Pacific temperature gradient is less clear, where simulations with a gradient between 3.5 – 4.2 °C can have essentially the same ENSO strength. However, the 2x and 4x simulations clarify this by displaying a strongly weakened east-west gradient produces a greatly enhanced ENSO strength. The 2x and 4x simulations indicate that the mean state Bjerknes feedbacks (western windstress, east-west temperature gradient, and eastern upwelling) in those simulations are well outside the range seen in the paleo time slice simulations, contributing to a new regime in the tropical Pacific that has enhanced ENSO strength and frequency.

We propose the following mechanisms are controlling ENSO strength in each of our time periods:

(1) The 2x and 4x simulations have an enhanced ENSO due to strong warming of the cold tongue associated with increased atmospheric CO_2 (Figs. 7 and 8), which greatly reduces the east-west temperature gradient, slackens easterly winds, greatly weakening upwelling, and sharpening the thermocline gradient.

(2) The mid-Holocene simulations have an insolation driven enhanced Indian summer monsoon, which strengthens west Pacific easterly winds, thereby inhibiting ENSO, which is in agreement with other mid-Holocene modeling studies (Liu et al.,2000; Brown et al., 2008; Zheng et al, 2008). The 12ka - 3ka simulations have a stronger than present correlation between the Niño 3 index and the All India Rainfall (AIR) index, even when the 3ka monsoon is weaker than 0ka.

(3) The 21ka – 15ka simulations have ENSOs that are weaker than those of the mid-Holocene, but the cause of this reduction is not well resolved by our analysis. The 21ka and 0ka simulations share similar east-west Pacific temperature gradients and Niño 4 windstress, but despite the similar windstress, the 21ka simulation has much stronger upwelling. Our analysis does not include a non-ENSO source of enhanced upwelling or weaker than present thermocline gradient, but they appear to play a role in suppressing ENSO at the LGM (which could also apply to the Holocene simulations. We prefer the mechanistic explanation of an enhanced Indian summer monsoon).

The significantly reduced ENSO strength in our LGM simulation is in direct conflict with the findings of Otto-Bliesner et al. (2003) and An et al. (2004), who find a stronger LGM ENSO. However, Otto-Bliesner et al. (2003) attributes the stronger LGM ENSO in their simulation to a sharpened thermocline gradient, while An et al. (2004) attribute the strengthening in their simulation to a shoaling of the thermocline. Results from our 2x and 4x simulations indicate a stronger ENSO is associated with a sharper thermocline gradient, as found in Otto-Bliesner et al. (2003). Using models from PMIP2, Zheng et al. (2008) found that three out of four models studied have a reduced LGM ENSO, while one simulated a stronger ENSO at LGM. Changes in LGM ENSO strength are found to be less conclusive than in the mid-Holocene simulations, and are generally more related to mean tropical cooling and a weakening of the tropical thermocline rather than changes in equatorial dynamics (Zheng et al., 2008).

Teleconnections in the paleo time slice simulations are similar to those of the 0ka simulation, which may help validate the assumption of stationary teleconnections used in proxy analysis. The largest exception to stationary teleconnections in our paleo simulations is an Indian temperature anomaly reversal during El Niño events from a cold negative anomaly in 0ka to a warm positive anomaly at 21ka – 15ka. It should be noted though that the sign of the 0ka teleconnection does not match that of observations (Alder et al., *in prep*), so this finding should be interpreted with caution.

Although our simulations show a reduced mid-Holocene ENSO within the range reported by proxy evidence and is in good agreement with other model simulations, our findings are fundamentally bound by the limitations of the model. Like any model, GENMOM does not produce a perfect representation of real world ENSO. The ENSO simulated by GENMOM is demonstrated to be on par with other models (Alder et al., *in prep*), yet the lack of seasonal phase locking and the simulation of an east Pacific temperature semi-annual cycle may be serious limitations to the application of GENMOM to testing ENSO related hypotheses. Such is the case with the Clement et al. (1999) hypothesis on a mid-Holocene insolation driven reduction of ENSO strength. The hypothesis requires an accurate simulation of the Pacific seasonal cycle regarding temperature, seasonal winds, and the location of the ITCZ. GENMOM cannot affirm or refute this hypothesis because the model lacks the required seasonality in the tropical Pacific. Moreover, by keeping vegetation constant our simulations may be underestimating past changes due to the lack of vegetation-climate feedbacks. In addition to benefiting from improved models, more complete proxy reconstructions are needed in order to rigorously validate past climate simulations. Although the MARGO reconstruction has excellent spatial coverage, the GHOST reconstruction has very few points in the Pacific Warm Pool and none in the open ocean, limiting our knowledge of how the east-west temperature gradient changed in the past. There are very few pollen reconstructions in South America, Southeast Asia, and Australia to validate modeled changes in precipitation or teleconnections. Despite these caveats, GENMOM is shown to simulate tropical SST changes in agreement with the best proxies available and simulates reduced ENSO strength within the proxy range of 15 – 60%, despite both limitations of the model and the reconstruction data.

5.6 References

AchutaRao, K. and Sperber, K. R.: ENSO simulation in coupled ocean-atmosphere models: Are the current models better? Climate Dynamics, 10.1007/s00382-006-0119-7, 2006.

Alder, J. R., Hostetler, S. W., Pollard, D., and Schmittner, A.: Evaluation of a present-day climate simulation with a new coupled atmosphere-ocean model GENMOM, Geosci. Model Dev., 4, 69-83, doi:10.5194/gmd-4-69-2011, 2011.

Alder, J. R., Hostetler, S. W. and Pollard, D.: The sensitivity of ENSO to increased atmospheric CO2 as simulated by the atmosphere-ocean model GENMOM, *in prep*.

An, S.-I., Timmermann, A., Bejarano, L., Jin, F.-F., Justino, F., Liu, Z., and Tudhope, A. W.: Modeling evidence for enhanced El Nino–Southern Oscillation amplitude during the Last Glacial Maximum, Paleoceanography, 19, PA4009, doi:10.1029/2004PA001020, 2004.

Battisti, D. S., and Hirst, A.C.: Interannual variability in the tropical atmosphere/ocean system: Influence of the basic state, ocean geometry and nonlinearity, J. Atmos.Sci., 46, 1687-1712, 1989.

Bjerknes, J.: Atmospheric teleconnections from the equatorial Pacific. Monthly Weather Review, 96, 163-172, 1969.

Braconnot, P., Otto-Bliesner, B., Harrison, S., Joussaume, S., Peterchmitt, J.-Y., Abe-Ouchi, A., Crucifix, M., Driesschaert, E., Fichefet, Th., Hewitt, C. D., Kageyama1, M., Kitoh, A., Loutre, M.-F., Marti, O., Merkel, U., Ramstein, G., Valdes, P., Weber, L., Yu, Y., and Zhao, Y.: Results of PMIP2 coupled simulations of the Mid-Holocene and Last Glacial Maximum – Part 2: feedbacks with emphasis on the location of the ITCZ and mid- and high latitudes heat budget. Clim. Past, 3, 279–296, 2007.

Brown J, Collins, M., Tudhope, A.: Coupled model simulations of mid-Holocene ENSO and comparisons with coral proxy records. Adv Geosci 6:29–33, 2006.

Brown, J., Collins, M., Tudhope, A. W., and Toniazzo, T.: Modelling mid-Holocene tropical climate and ENSO variability: Towards constraining predictions of future change with palaeo-data, Clim. Dyn., 30, 19 – 36, 2008.

Chiang, J.C.H., Fang, Y., Chang, P.: Pacific Climate Change and ENSO Activity in the Mid-Holocene. Journal of Climate, 22, 923-939, doi: 10.1175/2008JCLI2644.1, 2009.

Clement, A.C., Seager, R., Cane, M.A.: Orbital controls on the El Nino/Southern Oscillation and the tropical climate. Paleoceanography, 14, 441-456, 1999.

Clement, A.C., Seager, R., Cane, M.A.: Suppression of El Nino during the mid-Holocene by changes in the earth's orbit. Paleoceanography ,15, 731– 737, 2000.

CLIMAP Project Members: Seasonal reconstructions of the earth's surface at the Last Glacial Maximum, pp. 18, Geol. Soc. Am. Map and Chart Series, MC-36, 1981.

Cole, J.: A Slow Dance for El Niño. Sciencexpress, pg 1, doi:10.1126/science.1059111, 2001.

Collins, M.: Uncertainties in the response of ENSO to Greenhouse Warming, Geophys. Res. Lett., 27, 3509–3513, 2000a.

Collins, M.: The El-Niño Southern Oscillation in the second Hadley Centre coupled model and its response to greenhouse warming. J. Climate, 13, 1299–1312, 2000b.

Donders, T. H., Wagner-Cremera, F., and Vissche, H.: Integration of proxy data and model scenarios for the mid-Holocene onset of modern ENSO variability. Quaternary Science Reviews, Volume 27, Issues 5-6, pg 571-579, doi:10.1016/j.quascirev.2007.11.010, 2008.

Fedorov, A. V., and Philander, S. G.: Is El Niño Changing? Science, 288, pg 1997-2002, doi: 10.1126/science.288.5473.1997, 2000.

Fedorov, A. V., and Philander, S. G.: A stability analysis of tropical oceanatmosphere interactions: Bridging measurements and theory for El Nino, J. Climate, 14, 3086–3101, 2001.

Feldberg, M. J. and Mix, A. C.: Planktonic foraminifera, sea surface temperatures, and mechanisms of oceanic change in the Peru and south equatorial currents, 0–150 ka BP. Paleoceanography, vol. 18, no. 1, 1016, doi:10.1029/2001PA000740, 2003.

Guilyardi, E.: El Niño–mean state–seasonal cycle interactions in a multi-model ensemble. Climate Dynamics, 26, 329–348, 2006.

Jin, F.-F.: An Equatorial Ocean Recharge Paradigm for ENSO. Part I: Conceptual Model. The Journal of Atmospheric Sciences, 54, 811-829, 1997.

Koutavas, J., Lynch-Stieglitz, T. M., Marchitto, J. P. Jr., and Sachs, J. P.: El Nino-like pattern in Ice Age tropical Pacific sea surface temperature, Science, 297, 226–230, 2002.

Kutzbach, J.E. and Otto-Bleisner, B. L.: The sensitivity of the African-Asian monsoonal climate to orbital parameter changes for 9000 years in a low resolution general circulation model. J.Atmos.Sci., 39, 1177-1188, 1982.

Lea, DW, Pak, D.K., Spero, H.J.: Climate impact of Late Quaternary equatorial Pacific sea surface temperature variations. Science 289:1719–1724, 2000.

Leduc, G., Schneider, R., Kim, J.-H., Lohmann, G.: Holocene and Eemian sea surface temperature trends as revealed by alkenone and Mg/Ca paleothermometry. Quaternary Science Reviews, vol 29, pg. 989–1004, doi:10.1016/j.quascirev.2010.01.004, 2010.

Liu Z, Kutzbach, J., Wu, L.: Modeling climate shift of El Nino variability in the Holocene. Geophys Res Lett 27:2265–2268, 2000.

Liu Z, Otto-Bliesner B, Kutzbach, J., Li, L., Shields, C.: Coupled model simulation of the evolution of global monsoons in the Holocene. J Clim 16:2472–2490, 2003.

Liu, Z., Brady, E. C., and Lynch-Stieglitz, J.: Global ocean response to orbital forcing, Paleoceanography, 18, doi:10.1029/2002PA000819, 2003.

MARGO Project Members: Constraints on the magnitude and patterns of ocean cooling at the Last Glacial Maximum. Nature Geoscience, vol 2, pp 127- 132, doi: 10.1038/NGEO411, 2009.

McGregor, H.V. and Gagan, M.K.: Western Pacific coral δ18O records of anomalous Holocene variability in the El Nino-Southern Oscillation. Geophysical Research Letters, 31, doi:10.1029/2004GL019972, 2004.

Meehl, G.A., Gent, P.R., Arblaster, J.M., Otto-Bliesner, B.L., Brady, E.C., Craig, A.: Factors that affect the amplitude of El Nino in global coupled climate models. Clim Dyn 17:515–526, 2001.

Merryfield, W. J.: Changes to ENSO under CO2 doubling in a multimodel ensemble. J. Climate, 19, 4009–4027, 2006.

Moy, C.M., Seltzer, G.O., Rodbell, D.T., Anderson, D.M.: Variability of El Nino/ Southern Oscillation activity at millennial timescales during the Holocene epoch. Nature, 420, 162– 165, 2002.

Neelin, J. D., Battisti, D. S., Hirst, A. C., Jin, F.-F., Wakata, Y., Yamagata, T., and Zebiak, S. E.: ENSO theory, J. Geophys.Res., 103, 14,261–14,290, 1998.

Otto-Bliesner, B, Brady, E., Shin, S., Liu, Z., Shields, C.: Modeling El Nino and its tropical teleconnections during the last glacial-interglacial cycle. Geophys Res Lett 30 DOI 10.1029/2003GL018553, 2003.

Quinn, W. H., Zopf, D.O., Short, K. S. and Yang Kuo, R.T.W.: Historical trends and statistics of the Southern Oscillation, El Niño, and Indonesian droughts. Fish. Bull., 76,663–678, 1978.

Rodbell, D. T., Seltzer, G.O., Anderson, D.M., Abbott, M.B., Enfield, D.B., and Newman, J.H.: An ~15,000-year record of El Nino-driven alluviation in southwestern Ecuador. Science 283, 516–520, 1999.

Rodo, X. and Rodriguez-Arias, M-A.: El Niño–Southern Oscillation: Absent in the early Holocene? Journal of Climate, 17, 423–426, 2004.

Schopf, P.S., and Suarez, M. J.: Vacillations in a coupled ocean-atmosphere model, J. Atmos. Sci., 45, 549-566, 1988.

SCOR: Prediction of El Niño. Proc. No. 19, Paris, France, Scientific Committee for Ocean Research Working Group 55, 47–51, 1983.

Shin, S. I., Liu, Z., Otto-Bliesner, B. L., Brady, E. C., Kutzbach, J. E., and Harrison, S. P.: A simulation of the Last Glacial Maximum Climate using the NCAR CSM, Clim. Dyn., 20, 127– 151, 2003.

Sontakke, N. A., Plant, G. B., and Singh, N.: Construction of all-India summer monsoon rainfall series for the period 1844–1991, J. Clim., 6,1807–1811, 1993.

Suarez, M. J., and Schopf, P.S.: A delayed action oscillator for ENSO, J. Atmos. Sci., J5, 3283-3287, 1988.

Taylor, K.E., Stouffer, R.J., and Meehl, G.A.: A Summary of the CMIP5 Experiment Design. http://cmip-pcmdi.llnl.gov/cmip5/docs/Taylor_CMIP5_design.pdf, 2011.

Timmermann A., Okumura, Y., An, S.-I., Clement, A., Dong, B., Guilyardi, E., Hu, A., Jungclaus, J., Krebs, U., Renold, M., Stocker, T.F., Stouffer, R.J., Sutton, R., Xie, S.-P., Yin, J.: The influence of a weakening of the Atlantic meridional overturning circulation on ENSO. Journal of Climate, 20, 4899- 4919, 2007.

Trenberth, K.E.: The definition of El Niño. Bulletin of the American Meteorological Society 78, 2771–2777, 1997.

Trend-Staid, M., and Prell, W. L.: Sea surface temperature at the Last Glacial Maximum: A reconstruction using the modern analog technique, Paleoceanography, 17, doi:10.1029/2000PA000506, 2002.

Tudhope, A.W., Cilcott, C.P., McCulloch, M.T., Cook, E.R., Chappell, J., Ellam, R.M., Lea, D.W., Lough, J.M., Shimmield, G.B.:Variability in the El Nino–Southern Oscillation through a glacial–interglacial cycle. Science, 291, 1511– 1517, 2001.

UK Meteorological Office, Hadley Centre: HadISST 1.1 - Global sea-Ice coverage and SST (1870-Present), [Internet]. British Atmospheric Data Centre, Downloaded 2/8/2010. Available from http://badc.nerc.ac.uk/data/hadisst/, 2006.

Webster P., and Yang, S.: Monsoon and ENSO: selectively interacting systems. Quart J R Meterol Soc 118:877–926, 1992.

Wolter, K., and Timlin, M.S.: Monitoring ENSO in COADS with a seasonally adjusted principal component index. Proc. of the 17th Climate Diagnostics Workshop, Norman, OK, NOAA/NMC/CAC, NSSL, Oklahoma Clim. Survey, CIMMS and the School of Meteor., Univ. of Oklahoma, 52-57, 1993.

Zheng, W., Braconnot. P., Guilyardi, E., Merkel, U., Yu, Y.: ENSO at 6ka and 21ka from ocean–atmosphere coupled model simulations. Clim Dyn (2008) 30:745–762, DOI 10.1007/s00382-007-0320-3, 2008.

Chapter 6: Conclusions

Chapter 2 concludes that GENMOM produces a global climatology and atmospheric circulation that compare well to three AOGCMs and observations. The simulated global 2 m air temperature is 0.6 °C warmer over oceans and 1.3 °C colder over land. Cold SST anomalies in the Norwegian Sea are explained by excessive sea-ice in both winter and summer, which is in turn caused by weak Atlantic Ocean overturning. A warm bias in the Southern Ocean is attributed to a weak ocean overturning resulting in a poor simulation of the Deacon Cell, which suppresses associated cold water upwelling in the Southern Ocean. GENMOM simulates a double ITCZ when coupled with the OGCM, which is not present when GENESIS is coupled to a slab ocean.

The global ocean temperature is well simulated, with the exception of a warm bias between 200 – 1000 m in the tropics and mid-latitudes. Salinity is well simulated, but with a fresh bias in the North Atlantic caused by underrepresentation of narrow channels (i.e., the Norwegian Sea) at T31 model resolution and a 1+ PSS salinity bias in the northern mid latitudes originating in the Gulf of Mexico. Ocean overturning is simulated with the correct spatial pattern, but is generally weaker-than-observed. Weak meridional ocean overturning is attributed to (i) weak and northwardly displaced westerly winds in the Southern Hemisphere due to coarse topography and (ii) a narrow and shallow Drake Passage also due to coarse orography. Most ocean surface currents are well simulated by GENMOM, with the exception of narrow currents such as the Gulf Stream and the Kuroshio Current that are weaker-than-observed again due to the coarse T31 resolution. Northern Hemisphere Sea-ice is well simulated with the exception of excess sea-ice in the Norwegian Sea. However, the Southern Hemisphere sea-ice extent is too small compared to observations.

Chapter 3 analyzes the fidelity of ENSO produced by GENMOM, finding that it is on par with eight IPCC AR4 models. The Niño 3 - 4 indices have a standard deviation within 0.3 °C of the observations, indicating GENMOM is producing variability in the tropical Pacifc that is comparable to observations. However, the model simulates western Pacific SSTs that are too cool and eastern Pacific SSTs that are too warm and too zonal, resulting in a weaker-than-observed east-west Pacific surface temperature gradient. GENMOM produces a semi-annual temperature seasonal cycle that is not seen in the observations but is not uncommon in AOGCMs. The model simulates ENSO events with a realistic frequency (5.6-year period) and generally correct global spatial patterns of temperature and precipitation teleconnections

Using 300-year CO_2 sensitivity experiments, GENMOM simulates more frequent and higher amplitude ENSO events with CO_2-driven global warming, specifically at 4x atmospheric CO_2 levels. ENSO events are more intense due to disproportionate heating of the eastern Pacific than the western Pacific, such that the east-west temperature gradient is reduced by ~34% in the 4x simulation. The weakened east-west temperature gradient slackens west Pacific windstress by 38% and thereby weakening east Pacific upwelling by ~32% in the 4x simulation. EOF analysis of the 4x simulation reveals the ENSO region of action is constrained by 15-20° on its western boundary, resulting in a westward shift in the Walker Circulation.

Chapter 4 applies GENMOM to simulate past climates for the LGM, deglacial, and Holocene and compares model output to the best available proxy reconstructions for the LGM and mid-Holocene. GENMOM captures the glacial-interglacial changes in polar temperature but does not simulate a 6ka 'climatic optimum'; instead the model continues to warm progressively to present. Reconstructed SSTs from the MARGO project are used to validate the 21ka simulation, finding the model is in good agreement over broad spatial scales, with regional discrepancies between the model and proxy data. The simulated LGM is globally ~6.8 °C cooler than present due to an increase in northern hemispheric albedo from continental ice sheets and greatly reduced greenhouse gases. The GHOST reconstruction dataset is used to validate mid-Holocene SSTs, finding GENMOM is cooler than the data indicate due to a lack of a 'climatic optimum'.

Fossilized pollen reconstructions from the mid-Holocene indicate the western United States was wetter-than-present, while the east was predominantly drier. Much of Africa, Europe and Asia were considerably wetter-than-present. The GENMOM 6ka simulation agrees well with pollen records from Africa and the eastern United States, but does not agree with pollen proxies from the western United States, Europe and Asia. The model captures the observed mid-Holocene increased moisture in northern Africa, though the increased moisture does not extend to the northern most limit of the continent. The mid-Holocene simulations have a strengthened Indian summer monsoon, which is in agreement with previous modeling and proxy studies.

LGM pollen reconstructions exhibit widespread drying over Europe and Asia, while indicating increased precipitation in the southwest United States and drying in the east. Although the pollen data are sparse, the GENMOM 21ka simulation agrees very well with these patterns. Though LGM lake level reconstructions are sparse, the model agrees well with an LGM increase in P-E in the western United States.

Chapter 5 leverages the seven paleo simulations performed and evaluated in Chapter 4 as well as the 2x and 4x simulations performed in Chapter 3. ENSO events in the mid-Holocene simulations are weakened by 20%, in good agreement with the 15 – 60% reduction as indicated in coral and lake sediment proxy records. The reduction is associated with an enhancement of Bjerknes feedbacks that drive stronger winds, enhanced east Pacific upwelling, and increased east-west Pacific surface temperature gradient. This mid-Holocene weakening of ENSO is caused by a precessionally-driven enhancement of the Indian summer monsoon that enhances west Pacific trade winds during summer, thereby weakening ENSO strength, which is supported by previous modeling studies. The 21ka – 15ka simulations have a 25% reduction in ENSO strength, which is not explained by changes in equatorial dynamics but rather mean tropical cooling and a weakening of the tropical thermocline. As in Chapter 3, the 2x and 4x simulations have an enhanced ENSO due to strong warming of the cold tongue associated with increased atmospheric CO_2, which greatly reduces the east-west temperature gradient, slackens easterly winds, greatly weakening upwelling, and sharpening the thermocline gradient.

The ten simulations produced by this thesis provide exciting opportunities for future work regarding high-resolution regional downscaling for North America. The LGM simulation provides an opportunity to study the influence the Laurentide Ice Sheet had on regional climate, including altered patterns of plant distributions. The combination of the simulations produced by this thesis and regional modeling allow for detailed studies of how ENSO teleconnections are downscaled and how they impact North America. Chapter 3 notes a temperature sign reversal for the teleconnection to the western United States under both El Niño and La Niña events. The impacts of this sign reversal are best studied by applying regional modeling for the western United States. Outside of regional downscaling, Chapter 5 concludes the cause of 2x and 4x enhanced ENSO strength is caused by an asymmetric warming of the eastern Pacific, which greatly reduces the east-west temperature gradient. This thesis does not explore the source of the asymmetric warming, which should be done in future work in order to have a stronger mechanistic explanation for strengthened ENSO events under global warming.